University of South-Eastern Norway
Faculty of Technology, Natural Sciences and Maritime Studies
—
Doctoral dissertation no. 61
2020

Christian Berg

Modeling for Automatic Control and Estimation of Influx and Loss During Drilling Operations

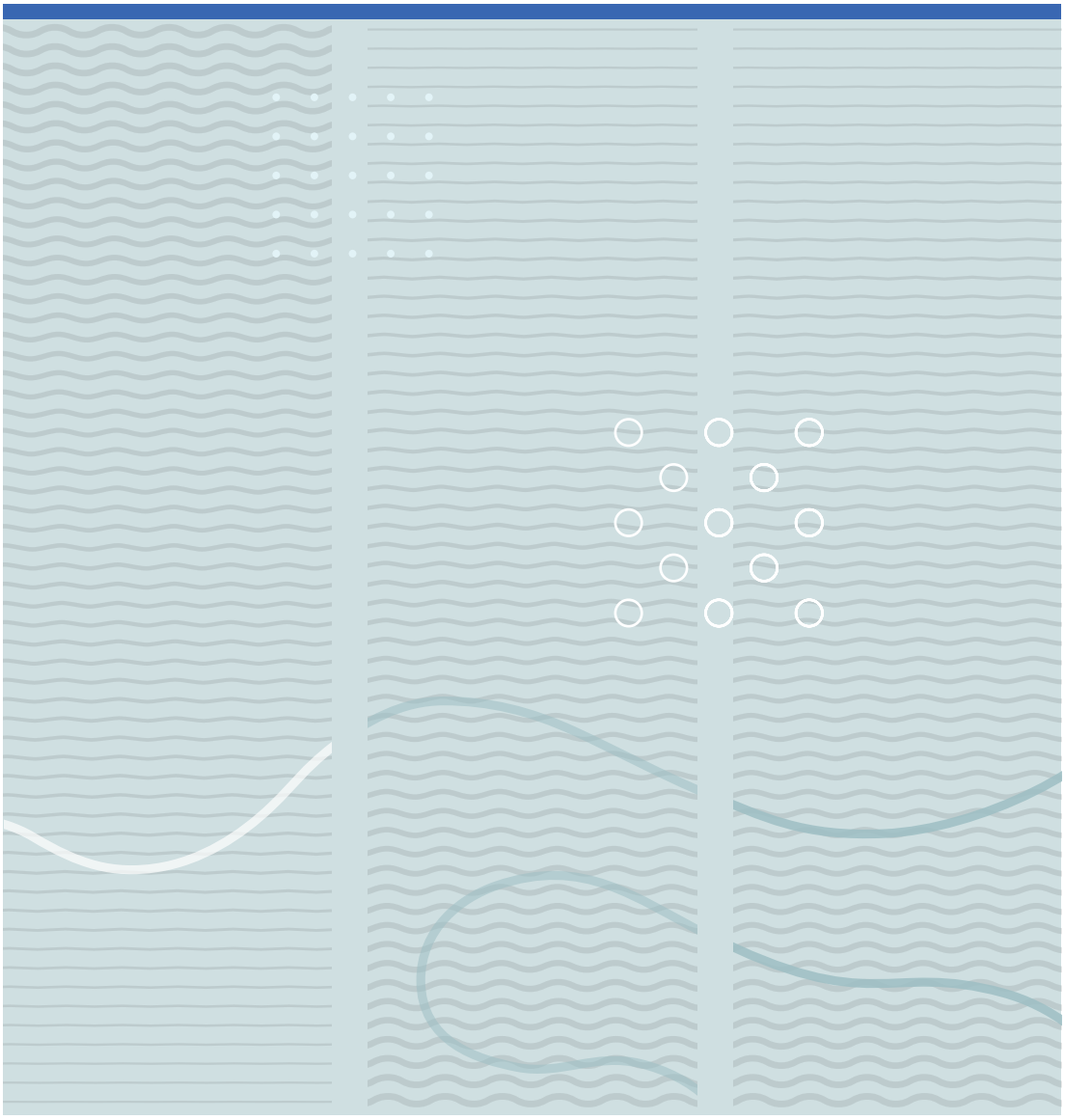

Christian Berg

Modeling for Automatic Control and Estimation of Influx and Loss During Drilling Operations

A PhD dissertation in
Process, Energy and Automation Engineering

Faculty of Technology, Natural Sciences and Maritime Studies
University of South-Eastern Norway
Porsgrunn, 2020

Doctoral dissertations at the University of South-Eastern Norway no. 61

ISSN: 2535-5244 (print)
ISSN: 2535-5252 (online)

ISBN: 978-82-7206-544-6 (print)
ISBN: 978-82-7206-545-3 (online)

Print: University of South-Eastern Norway

In loving memory of my grandfather Kjell O. Berg (9.1.1936-29.12.2018) and grandmother Ingeborg M. Berg (5.3.1939-30.6.2019)

Preface

This thesis is submitted to the University of South-Eastern Norway (USN) in partial fulfilment of the requirements of the degree of Philosophiae Doctor (PhD) in the Process, Energy and Automation Engineering program. The work has been funded as an Industrial PhD project by the Norwegian Research Council. The PhD project has taken place in the Telemark Modelling and Control Center (TMCC) research group at USN, as well as at Kelda Drilling Controls.

The project has been under the supervision of Professor Bernt Lie, and with co-supervision by Adjunct Associate Professor Glenn-Ole Kaasa. The work has been carried out at Kelda Drilling Controls, University of South-Eastern Norway, as well as on-site in the United Arab Emirates and Russia.

The thesis is article based, consisting of a collection of scientific papers and contain two main parts. The first section provides an introduction to the drilling process, commonly used hydraulic models in this context, and a very brief summary of the main results in the articles. Part two consist of 7 research articles that found the basis of the thesis.

The work has been mainly related modelling the dynamics of the drilling process for both single and multi phase flows, performed in parallel with controller development by the team at Kelda Drilling Controls.

Porsgrunn, 11th February 2020

Christian Berg

Acknowledgements

First of all, I would like to express my thanks to my main supervisor, Bernt Lie, for guidance and support through the years. I would also like to thank my co-supervisor, Glenn-Ole Kaasa, for constructive advice and numerous rewarding discussions. Thank you for challenging me and making me better. A special thanks to Knut Vaagsaether for providing advice and rewarding discussions.

I would like to thank all my colleagues at Kelda Drilling Controls for sharing their knowledge, for numerous valuable discussions, for all the fun we have had together, and for making a great place to work.

I would also extend thanks to the MPD crews at Air Drilling Associates for making a green PhD student feel included and telling me about the vee-door key before anyone sent me to get it.

A special thanks to all the PhD students in the HYDRA Project, Naveen Velmurugan, Mohammad Abbasi and Sajad Naderi Lordejani. Working with you has been great, and through your stays here in Porsgrunn, motivation for finalizing this work was born. Thanks to the PhD students in the SEMI-KID project and everyone at the Telemark Modeling and Control Center (TMCC) research group for interesting presentations and discussions.

I am grateful to my family for supporting me through the years. A very special thanks to my wife Thea for your support, love and never ending patience. Finally, thanks to my two sons Eirik and Sondre.

Summary

In the modern energy driven world, oil and gas will be important resources, at least in the foreseeable future. Wells with challenging pressure windows are more commonly drilled, and in recent years the drop in oil prices has lead to an industry focus on reduction of non productive time. Managed Pressure Drilling, considered an unconventional drilling method, tackles a lot of current industry challenges. With managed pressure drilling one has more control over the bottom hole pressure. This lead to the possibility of drilling what would be considered conventionally un-drillable wells, an increase in safety and reduced non productive time.

Managed pressure drilling has been forecasted to grow in the next years, fuelled by an increase in the level of automation. Drilling for oil and gas is a complex process, involving pumping of fluid through kilometres of fluid conduit, leading to wave propagation phenomena that becomes apparent at timescales relevant for automatic control. There has been a significant research effort in academia for both modelling, control design and observer designs in recent years. A lot of the work done in academia has not taken the step from university and out into the field.

Gas influx, and the detection of this has had a surge in research after the Macondo Disaster. The design of kick detection and well control strategies require mathematical models of the same dynamics as control design for managed pressure drilling. It can be said that in terms of kick detection, especially for conventional drilling, it is not the algorithms on how this can be done that is missing, but the sensors required for them. Through the work on this thesis, a possible alternative measurement principle has been studied, using a subcritical venturi flume.

Through the work of this PhD, the topic of modelling, at different detail levels has been studied. This has been performed in parallel with the development of a full MPD control system at Kelda Drilling Controls. This system is now in operation, and has numerous successful wells drilled. For design and upgrades of this control system, extensive testing is performed on a high fidelity PDE model capturing the dynamics of the drilling process. Development of the models and their accuracy is covered in three of the attached papers. For control design, simpler models are usually required. There has been numerous control and estimator designs based on simpler models in literature, but there has been limited publications on real life use of these designs.

The control system developed by Kelda Drilling Controls through the last 5 years is based on the most commonly used simplified model, and has been found have good performance in real drilling operations for both single phase and multiphase cases. Perhaps one of the main success criteria in this has been the extensive testing of different solutions on the high fidelity models coming from this work.

Managed pressure drilling opens up a lot of possibilities when it comes to both detection of unwanted reservoir influx, and circulating the influx out. MPD systems have less regulatory requirements and lower pressure rating than conventional well control equipment. Due to this, performing what would normally be considered a well control operation using MPD equipment should be done with care. The Influx Management Envelope (IME) helps to deal with this. Although wanted by industry, and very likely introduced as a planning tool in the official guidelines by the International Association of Drilling Contractors (IACD) for MPD operations world wide, no systematic description of the IME has existed in peer-reviewed journals. This is covered in the included paper on the IME.

List of Publications

Articles: Published and accepted

1. Berg, Christian, Anjana Malagalage, Cornelius E. Agu, Glenn-Ole Kaasa, Knut Vaagsaether, and Bernt Lie. "Model-Based Drilling Fluid Flow Rate Estimation Using Venturi Flume." IFAC-PapersOnLine 48, no. 6 (2015): 171–76. https://doi.org/10.1016/j.ifacol.2015.08.027.

2. Abbasi, Mohammad H., Sajad Naderi Lordejani, Naveen Velmurugan, Christian Berg, Laura Iapichino, Will H.A. Schilders, and Nathan van de Wouw. "A Godunov-Type Scheme for the Drift Flux Model with Variable Cross Section." Journal of Petroleum Science and Engineering 179 (August 1, 2019): 796–813. https://doi.org/10.1016/j.petrol.2019.04.089.

3. Berg, Christian, Jon Åge Stakvik, Bernt Lie, Knut Vaagsaether, and Glenn-Ole Kaasa. "Pressure Wave Propagation in Managed Pressure Drilling- Model Comparison with Real Life Data." In Proceedings of the 60th Conference on Simulation and Modelling (SIMS 59), 8. Linköping Electronic Conference Proceedings No. University of Västerås, Västerås, Sweden: Linköping University Electronic Press, August 13th–15th. https://doi.org/ecp2017091.

4. Berg, Christian, Geir Arne Evjen, Naveen Velmurugan, and Martin Culen. "The Influx-Management Envelope Considering Real-Fluid Behavior." SPE Drilling & Completion, Society of Petroleum Engineers, December 1, 2019. https://doi.org/10.2118/198916-PA.

5. Stakvik, Jon Age, Christian Berg, Glenn-Ole Kaasa, and Ole Morten Aamo. "Cascaded Bottom Hole Pressure Control in Managed Pressure Drilling." In 2017 IEEE Conference on Control Technology and Applications (CCTA), 2001–7. Mauna Lani Resort, HI, USA: IEEE, 2017. https://doi.org/10.1109/CCTA.2017.8062748.

6. Berg, Christian, Jon Åge Stakvik, Stanislav Kulikov, Maytham Badrawi, Glenn-Ole Kaasa, Aleksandr Dubovtsev, Sergey Korolev, and Gurban Veliyev. "Automated Pressure Control for UBD Operations: Case Study and Field Validation." SPE Drilling & Completion, Society of Petroleum Engineers, October 1, 2019. https://doi.org/10.2118/194555-PA.

Articles: Submitted for review

1. Abbasi, Mohammad H., Sajad Naderi Lordejani, Christian Berg, Laura Iapichino and Nathan van de Wouw. "A Well-Balanced Godunov-Type Scheme for the Euler Equations and the Drift Flux Model with Laminar Friction and Gravitation," Submitted to Journal of Computational Physics

Other contributions

1. Stakvik, Jon Åge, Christian Berg, Glenn-Ole Kaasa, Ole Morten Aamo, and Urs Lehner. "Adaptive Model Based Choke Control System for MPD Operations." In SPE-179714-MS, 11. SPE: Society of Petroleum Engineers, 2016. https://doi.org/10.2118/179714-MS.
2. Stakvik, Jon Åge, Christian Berg, Glenn-Ole Kaasa, Robert Graham, and Antonio Torrealba. "Model-Based Control in Managed Pressure Drilling." In SPE-184649-MS, 15. SPE: Society of Petroleum Engineers, 2017. https://doi.org/10.2118/184649-MS.
3. Welahettige, Prasanna, Christian Berg, Joachim Lundberg, Bernt Lie, and Knut Vaagsaether. "Computational Fluid Dynamics Study of the Effects of Drill Cuttings on the Open Channel Flow." International Journal of Chemical Engineering 2019 (August 22, 2019): 1–9. https://doi.org/10.1155/2019/6309261.
4. Naderi Lordejani, Sajad, Mohammad Abbasi, Naveen Velmurugan, Christian Berg, Jon Åge Stakvik, Bart Besselink, Laura Iapichino, Florent Di Meglio, Wil H. A. Schilders and Nathan van de Wouw. "Modelling and numerical implementation of managed pressure drilling systems for the assessment of pressure control systems" SPE Drilling & Completion, Society of Petroleum Engineers, 2019.

Contents

List of Figures

Nomenclature

β	Fluid bulk modulus
ρ	Density
c	Speed of sound
F	Friction source term
$F(U)$	PDE flux vector
G	Gravity source term
p	Pressure
q	Flow rate
$S(U)$	PDE source vector
U	PDE state vector
u	Velocity
V	Volume
BOP	Blow Out Preventer
BSEE	Bureau of Safety and Environmental Enforcement
CFD	Computational Fluid Dynamics
DFM	Drift Flux Model
EOS	Equation of state
FLIC	Flux Limiter Centered
FSI	Fluid Structure Interactions
IADC	International Association of Drilling Contractors
IME	Influx Management Envelope
LCM	Lost Circulation Material
LxF	Lax Friedrichs
NPT	Non-Productive Time
ODE	Ordinary Differential Equation
PDE	Partial Differential Equation
RCD	Rotating Control Device
SBP-MPD	Surface Backpressure Managed Pressure Drilling
UBD	Under-balanced Drilling
VOF	Volume of Fluid

WCM Well Control Matrix

Part I

Overview

1 Introduction

Part 1, overview is structured into two main chapters. Chapter 1 aims to provide background for the research, introducing drilling, Managed Pressure Drilling (MPD) and well control such that the included articles can more easily be put into context. After that, the chapter introduces dynamic modeling of drilling hydraulics, with common models reviewed. A very brief introduction into solution and analysis of systems of Partial Differential Equations (PDEs) is then given.

Chapter 2 summarize the main contributions of the included papers, and review more recent work where applicable. All included papers have their own literature review, and can be read as stand alone works.

1.1 Drilling

The first step before production of oil and gas is drilling the well. Drilling is the process of excavating a borehole into the ground by the use of specialized equipment and is performed by a drilling rig. When drilling, a long steel pipe (drillstring) made up of smaller pipe sections is used. This drillstring has a drillbit attached to the end. Rotation at the drillbit can be achieved by both rotation of the drillstring, a downhole motor or a combination of these.

Drilling fluid, often called "mud" is circulated by high pressure pumps into the drill string, and out through nozzles in the drillbit. Then the drilling fluid gets transported up the annulus, the gap between the drill string and wellbore, carrying drilled cuttings to the surface. When reaching the surface the drilling fluid is separated from the cuttings and recirculated to be pumped back down the drillstring. An overview of this flow path can be seen in figure Fig. 1.1.

The drilling fluid can be seen as having two main purposes. The drilling fluid drives the downhole motor if one is installed, cools the drillbit and transports rock cuttings to the surface. The second important task the drilling fluid achieves is that of pressure control: When drilling, a pressure in the annulus, ideally equal to the pressure in the drilled formation should be present to maintain wellbore stability and prevent flow of fluids from the formation into the wellbore or flow of fluids from the wellbore into the formation. The pressure in the wellbore is achieved through

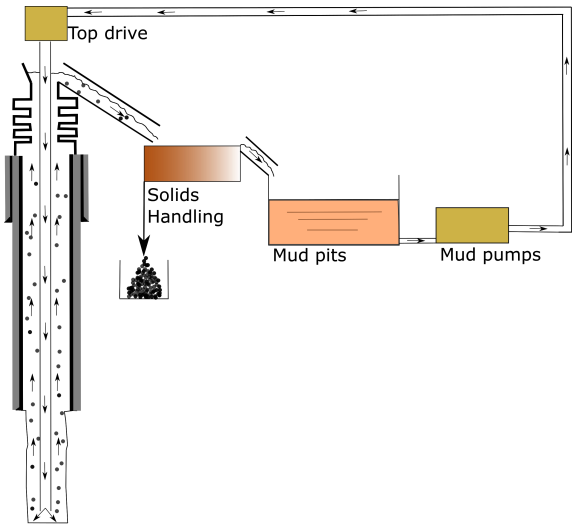

Figure 1.1: Drilling fluid flow path.

hydrostatic pressure from the density of the drilling fluid, and is primarily controlled by addition of high density solids.

In general, situations arise that for a given drilling fluid density, it is impossible to maintain the appropriate pressure everywhere in the wellbore from the surface to the planned well depth. Due to this, wells are drilled in multiple sections, where the previous section is cased off by steel pipes cemented in place, and the following section drilled with a smaller diameter. Through the use of casing, a balance between the formation and wellbore pressure has to be achieved only in the currently drilling section that is in contact with the formation, commonly called the open hole section. Figure 1.2 shows a wellbore schematic with collapse- annulus- and fracture- pressure versus depth, and casing that isolate sections above the current open hole section.

If the pressure in the open hole section becomes too low with respect to formation pressure, and the formation contains fluids and is permeable, fluid will flow from the formation. This flow is known as an influx. The downhole pressure where this happens is commonly denoted pore pressure. Another potential outcome if pressure becomes too low is that the structural integrity of the wellbore cannot be maintained, and the wellbore might collapse around the drillstring. The pressure where this happens is commonly known as collapse pressure.

If the pressure in the open hole becomes higher than the pore pressure, some of the drilling fluid will be lost to the formation. Drilling fluids contain additives that will plug the local formation (reduce local permeability when fluid flows into the formation from the wellbore) such that drilling with pressure above that of the pore pressure is possible without very high fluid losses. If downhole pressure becomes too high, fractures will be formed in the formation and drilling fluids will be lost into the formation. The pressure where the formation fractures is known as the

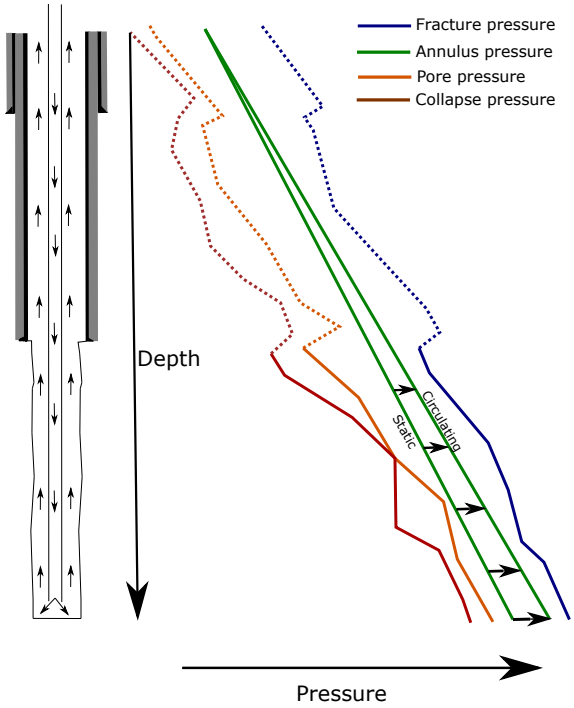

Figure 1.2: Collapse-, pore-, annulus- and fracture-pressure. The annulus pressure profile changes when circulating due to friction (exaggerated).

fracture pressure. The location in the open hole where fracture pressure is exceeded first when pressure is increased (the point in Fig. 1.2 where fracture pressure has the minimum distance to the annulus pressure) is known as the formation weak point.

If transient effects are not considered, the pressure in any part of the wellbore can be described by Eq. (1.1) where $p_{\text{Hydrostatic}}$ is the hydrostatic pressure at location z, and p_{Friction} is the frictional pressure loss from location z to the surface.

$$p(z) = p_{\text{Hydrostatic}} + p_{\text{Friction}} \tag{1.1}$$

In Eq. (1.1), the term p_{Friction} can not be actively controlled to stay within the pressure limits imposed by the formation. The reason for this is that the drilling fluid also has to be able to carry cuttings to the surface, thus, a minimum flow velocity and fluid properties are imposed from considerations with respect to cuttings transport.

Approximately every 30m (100ft) drilled, a connection has to be performed to extend the length of the drillstring. When performing a connection mud pumps are stopped to attach another stand of drillstring and p_{Friction} will be reduced to zero, changing the pressure along the annulus. The difference in downhole pressure when pumps are on and pumps are off is illustrated in Fig. 1.2. $p_{\text{Hydrostatic}}$ can be actively controlled by changing the drilling fluid density. This requires that a drilling fluid of different

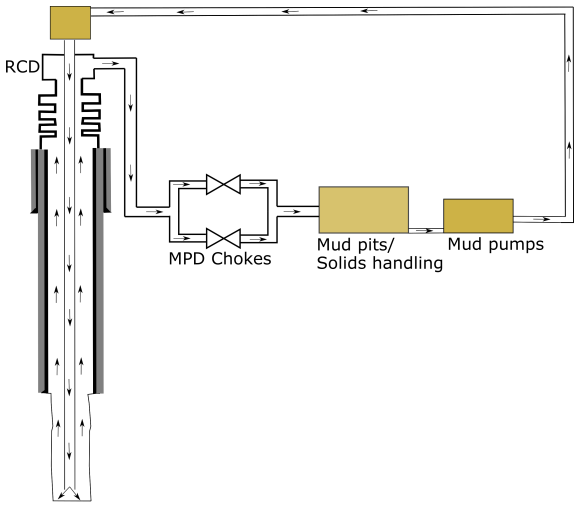

Figure 1.3: Managed pressure drilling. Drilling fluid is circulated from the rig mud pumps and down the drill string. At the bottom of the wellbore, the drilling fluid flows out through the drill bit via nozzles, and is then circulated up to the surface in the annular space between the drill string and annulus.

density is displaced through the system, a process that usually takes hours (being a function of well fluid volume and pump rate).

During conventional drilling, the Blow Out Preventer (BOP) can be closed to apply pressure from the surface, something that can be used to rapidly raise downhole pressure if required. Examples of this would be well control situations where the downhole pressure is not adequate to prevent flow from the formation, termed an influx or kick.

1.2 Managed Pressure Drilling

Surface Backpressure Managed Pressure drilling (SBP-MPD), is a variant of Managed Pressure Drilling (MPD) where pressure is applied to the well from the surface during drilling. For SBP-MPD, the annulus is sealed at the surface by a Rotating Control Device (RCD) and the drilling fluid is routed through control chokes. A schematic showing the equipment setup while using SBP-MPD is seen in Fig. 1.3. If transient effects are not considered, the downhole pressure with SBP-MPD can be described by Eq. (1.2) where p_{Surface} is the pressure at the MPD chokes.

$$p(z) = p_{\text{Surface}} + p_{\text{Hydrostatic}} + p_{\text{Friction}} \tag{1.2}$$

As for conventional drilling, p_{Friction} cannot be actively controlled directly as it is given through considerations such as cuttings transport. $p_{\text{Hydrostatic}}$ can be changed

by changing the mud density, but as for conventional drilling this is a slow process taking hours. p_{Surface} can be changed rapidly, giving almost direct control over downhole pressure. In cases where the flow rate, and thus p_{Friction} change, p_{Surface} can be used to compensate for the changes in friction at a given point. This makes MPD able to keep the pressure constant at one specific point in the well (commonly referred to as the anchor point), irrespective of flow rate. Due to the increased control of downhole pressure when using MPD, this unconventional drilling method has gained traction in recent years, both for drilling challenging wells, and as a way to reduce non-productive time (NPT) . Figure 1.4 shows the same case as Fig. 1.2, in the case of MPD. Note the fact that the pressure at the anchor point is the same in the circulation and static case. The possibilities presented by modern automation technology, with automatic control of surface-, anchor point-, or standpipe (pump)-pressure presents a substantial increase of control over the annulus pressure compared to conventional drilling.

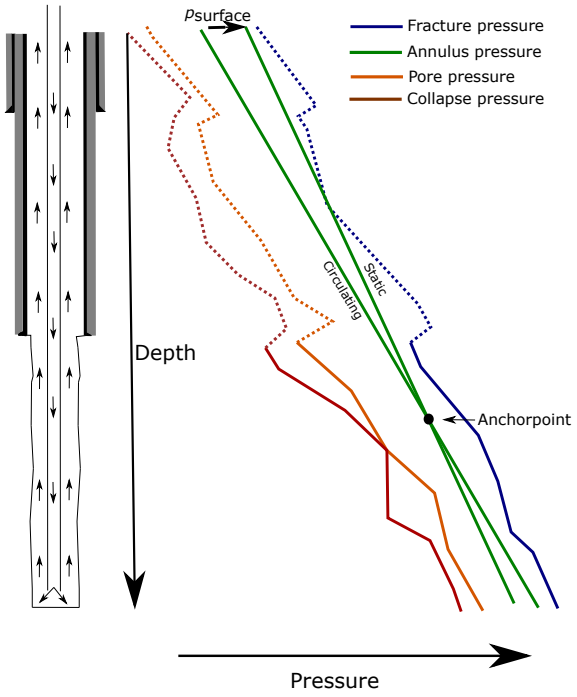

Figure 1.4: Collapse-, pore-, annulus- and fracture-pressure using MPD techniques. Annulus pressure profile change when circulating due to friction and applied surface pressure (exaggerated).

For design of control and estimation algorithms, dynamic models are required which are able to predict not only the flow and pressure during steady conditions, but also when moving from one operating point to another. There is a range of possible modeling approaches from the relatively simple model by Kaasa, Stamnes *et al.* [1] to more elaborate Partial Differential Equation (PDE) models capturing the travel of pressure waves in the system. There has been an extensive research effort on

controller and estimator design for MPD in recent years, both based on the model in [1], such as by [2]–[6] as well as for PDE models in [7]–[13]. Much of this work has been in academia only, and actual applications have not been published. Successful use of the model in [1] for MPD control design in the context of heave compensation and surge swab mitigation can be found in [6].

1.3 Well pressure control

If for some reason the downhole pressure in operation ends up below the pore pressure or above the fracture pressure, fluid influx or fluid losses will occur. *Well control*, typically a very specific definition with dedicated equipment, fixed procedures and regulatory requirements is here treated somewhat pragmatically. Regulations and guidelines on whether an influx should be considered a *well control* event is not covered here. This is treated in Section 1.5 as well as paper E in the case where MPD equipment can be used for dealing with minor influxes.

There are numerous possible operational reasons for ending up in a situation where downhole pressure is outside of the window specified by pore/collapse pressure and fracture pressure. In many cases, especially exploration drilling, the exact pore and fracture pressure is unknown, and well planning is based on best estimates. Fractures in the reservoir can also lead to local pore pressure (pressure in the fracture) being significantly lower or higher than expected for that formation zone. There could be operational reasons for exiting the pressure window, such as unintentional raising or lowering of mud density, drillstring movement (known as surge/swab), or for MPD operations, too high or low surface pressure applied to the well. In any case, exiting the pressure window will lead to loss of drilling fluid to the formation, or influx of formation fluids into the annulus. A too low annulus pressure can also lead to a formation collapse and thus the drillstring becoming stuck, even without any significant influx of formation fluid preceding it. The procedures for dealing with loss and influx are often very different, with minor losses often viewed as a necessary evil, especially for conventional drilling. Influx will in many cases be with formation fluids that are gaseous, flammable and in some cases extremely toxic. This leads to influxes being associated with very different considerations than losses in a health and safety perspective. Gas influxes will expand when being brought to the surface, and if not controlled, will lower downhole pressure further due to a lowering of hydrostatic pressure. This will lead to even more influx in a positive feedback mechanism. In the uncontrolled case this is what would be considered a blow out.

Both loss and influx is detected by the in and out flow of the well not being balanced. If an out flow measurement is available, an out flow from the well higher than the pump rate will indicate an influx. A lower out flow than pump flow would indicate

a loss. As the out flow is recirculated and pumped back through the mud pits, an increase or decrease in mud pit level will indicate the same. There are numerous other indicators of a possible influx and loss, such as changes in torque on the drillstring top drive and change of Rate Of Penetration (ROP). These indicators are mainly linked to mechanical feedback in the drilling system that the reservoir has changed. Thus they are not directly indicating an influx or loss but that the factors that could be associated with it is present.

1.3.1 Losses

If losses are encountered in operation, usually detected by a dropping mud level in the mud pit or a drop in return flow, multiple possible approaches to deal with the situation exist. One can lower downhole pressure by reducing drilling fluid density in the conventional drilling case, or reduce surface pressure in the MPD case (if already holding surface pressure). An important point to note is that lowering pressure to reduce losses runs the risk of having a lower pressure than pore pressure somewhere else in the annulus and thus taking an influx. Another option is trying to cure the losses by circulating Lost Circulation Material (LCM), a mud additive designed to reduce formation permeability, effectively plugging up the formation so losses are reduced/eliminated. In cases where LCM is unable to cure the losses and downhole pressure cannot be reduced further, two more possible options exist. One of the options is to keep drilling with losses, depending on cost and availability of drilling fluid and possible damage it can cause to the formation. If drilling with continued losses is not an option the second option is to set a contingent casing. This is an unplanned casing that seals off the problematic zone, but will lead to a lower diameter than planned at the end of the well (and thus lower well production). In the MPD case, walking the line with challenging pressure windows are usually possible for longer than the conventional case due to the smaller variations in downhole pressure between static and circulating.

A special case of losses that should be treated separately is the case where the losses are higher than the pump flow rate, commonly referred to as total losses. This case is significantly more challenging than the case where losses are not total, and total losses can quickly spiral into more serious well control situations. If total losses are encountered in MPD operations, this can lead to the inability to apply pressure at the surface due to lack of return flow. Depending on the initial surface pressure this can lead to a too low downhole pressure, and taking an influx somewhere else in the annulus. In both the MPD and conventional drilling case, if losses are substantial enough, the mud column and thus hydrostatic pressure can drop in the annulus, leading to possible influx. In the case where total losses do not lead to an influx, drilling with total losses is usually not an option when considering conventional drilling or using SBP-MPD. This is due to the fact that the lack of flow in the

annulus makes it impossible to transport drilled cutting to the surface, eventually leading to the possibility of getting a stuck drillstring. In practice, a contingent casing is often the only option if a sudden total loss is encountered that cannot be cured using LCM.

1.3.2 Influx

If downhole pressure is below the pore pressure, an unwanted flow of formation fluid into the annulus occurs, known as an influx or kick. An influx can consist of oil, water and/or gas, and is noticed from an increased out flow and rising mud pit levels. If an influx is encountered and detected, the pumps will typically be stopped first and then the BOP closed, known as a hard shut-in. The total influx volume will be calculated, and shut in standpipe and surface pressures will be recorded for the preparation of a kill sheet and attempted identification of the type of influx fluid. After the BOP is shut the downhole pressure will increase to the pore pressure, caused by to the pressure added from the BOP at the surface. This pressure added from the BOP stops the influx, and well control procedures are performed to re-establish control of the well. Typically the gas will be circulated through the closed BOP and well control chokes, adding surface pressure while keeping the pump pressure constant and the gas expands. When the gas is circulated out of the annulus, drilling fluid density is increased, and the surface pressure decreased. When the full procedure is finished, the downhole pressure has been increased by increasing $p_{\text{Hydrostatic}}$ and drilling can continue. The procedure where the gas is circulated out first, then the mud density is increased, is commonly referred to as Driller's method. For a thorough introduction to the actual step by step procedure of both the Driller's Method, as well as alternative well control procedures, see Schubert [14].

In MPD operations, the surface equipment available is similar to that of a conventional well doing well-control procedures with a closed BOP. This make MPD able to handle minor influxes without resorting to conventional well control procedures. For an influx during MPD, the surface pressure can be raised immediately to increase downhole pressure and suppress the influx. The influx can then be circulated to the surface while keeping the pump pressure constant, and drilling can continue without increasing the fluid density. The influx can typically also be circulated to the surface at a higher pump rate using MPD equipment than for conventional well control chokes.

1.4 Influx loss detection

For detecting influx and loss, numerous approaches exist. In general a fluid loss or influx will be detected through a mismatch in the inflow versus outflow in the

well, either indirectly through changes in mud pit level V_{mudpit}, directly through a measured change in outflow q_{return} for a constant inflow q_{pump}, or as a combination of this as well as other indicators of changing downhole conditions (Change of torque, hookload and pump pressure). Figure 1.5 shows an overview of the flow path while drilling, and the measured variables commonly involved in kick/loss detection where $q_{\text{influx/loss}}$ is the influx/loss flow rate, ideally zero in normal operation.

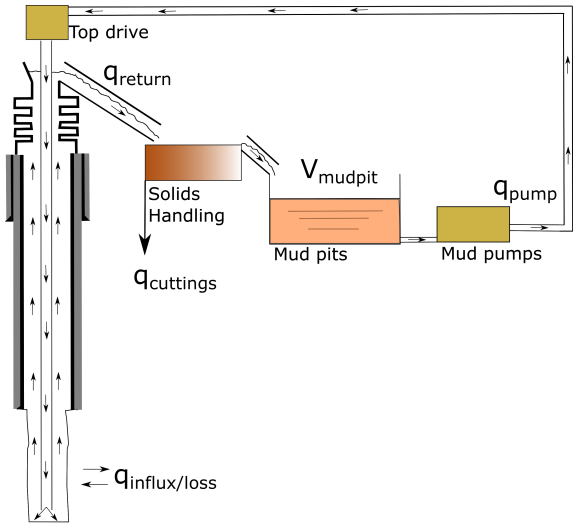

Figure 1.5: Circulation path while drilling, key measurements for influx loss detection.

Numerous detection and estimation strategies exist, usually based on the mud pit level V_{mudpit} or the volumetric flow in and out q_{pump} and q_{return}. The different methods have strengths and weaknesses with respect to detection time and influx/loss size required for detection [15], making the approach of combining multiple sensors appealing. Based on the method used, challenges with respect to sensor accuracy and reliability exists, especially for the measurement of return flow. This topic is covered independently in subsection 1.4.4.

In practice, influx and losses might come in the middle of changes in operating conditions, for instance a change in pump rate affecting the downhole pressure. Due to this, detection and estimation strategies that also work in transients would be the ideal approach, although this might be difficult in practice. If detection and estimation of influx is to be performed in transients, a dynamic model describing the dynamic behaviour of q_{return} vs q_{pump} and $q_{\text{influx/loss}}$ will be required.

1.4.1 Surface volume based methods

Kick detection from surface fluid volumes is the oldest and still most commonly used method for kick detection today [16]. Modern rig control systems have Pit-

Volume-Totalizers, using change in surface mud volume for kick/loss detection, with configurable alarm limits.

Challenges with all surface based methods is that they require a minimum influx or loss volume, depending on the resolution of the pit volume sensors. In many cases this required volume might be unacceptably high in the case of influx. Volume based methods also make no distinction with respect to kick severity, such that a large flow influx will still require a given influx volume before it can be detected.

Strengths with volume based approaches is that influx/loss rates below flow measurement detection accuracy will still be detected when the accumulated volume is above a certain threshold.

For dealing with influx during transients, and especially in pump off events, traditionally *fingerprinting* is performed. When fingerprinting, the increase in surface volume, caused by fluid expansion and drain back at the surface, is recorded when stopping the pumps, and then this is compared to the pit level increase at later connections [16].

Automatic algorithms that perform this fingerprinting and compare the pit level in transients to a known well signature has had developments in recent years with successful field use of for instance the Influx Detection at Pumps Stop (IDAPS) software [17]. Algorithms performing this fingerprinting can be based on both historic data and/or an internal model such as the one in [18] and comparison of the model and measurement. Cayeux and Daireaux [16] show the ability of high fidelity simulations to predict this drain back signature.

1.4.2 Flow rate based methods

In the simplest case, flow based kick detection for a steady flow rate can be performed by monitoring for changes in out flow. This is what is used for most simple paddle based kick/loss detection systems. Detection of influx and loss through change in out flow only, when out flow is not accurately measured can only provide a kick indication, not volume nor intensity other than in a qualitative sense.

If reliable and accurate flow rate measurements are available for both pump and return flow, flow-rate based methods can be taken further than just detection of changes.

In the ideal case,

$$\frac{\mathrm{d}V_{\mathrm{mudpit}}}{\mathrm{d}t} = q_{\mathrm{return}} - q_{\mathrm{pump}} - q_{\mathrm{cuttings}}, \tag{1.3}$$

for Fig. 1.5 in the case of no influx or loss. If q_{cuttings} is known then it is possible to detect both influx/loss rate, accumulated influx/loss volume, and have very rapid

detection of influx and loss with no minimum requirement on volume. Flow measurements can also be used together with a dynamic model of the well to perform this, even in the case of system transients such as described by Zhou, Nygaard *et al.* [19] and Hauge, Aamo *et al.* [20]. The limitation of flow rate based methods is that in reality, even for steady conditions, the measurements for q_{pump} and q_{return} are not perfectly aligned, such that a minimum difference, depending on the sensor accuracy, between these flow measurements is required. This leads to a minimum loss and influx rate that is detectable. Flow measurements of the accuracy required for this type of influx loss detection are traditionally only available in MPD operations.

The strength of flow based methods is that although there is a required kick/loss rate for reliable detection, there is no minimum required volume, as opposed to surface-volume based methods. Due to this, high intensity/high flow-rate losses and kicks can be detected almost immediately.

1.4.3 Sensor fusion methods

The strengths and weaknesses of volume based and flow based methods are largely complementary. This makes the prospect of combining these two methods promising. A challenge in the case where high quality q_{return} measurements are available, is that these measurements and the measurement of V_{mudpit} is usually performed by independent service providers on independent systems.

1.4.4 Return flow sensor accuracy and reliability

For measuring return flow in drilling operations, numerous approaches exist, with varying accuracy. An important factor for deciding the type of sensor to use is whether the surface fluid system is closed, as is the case for MPD operations, or open as for most conventional drilling operations. Measurement principles that are based on open channel flows (the case for conventional drilling) will not work for closed circulation systems. In general, measurement of flow rate for closed circulation systems is simpler than for open channel flows. Measurement principles that require the entire flow return line pipe to be filled with liquid can in some cases be used in the open channel conventional drilling case. When this is done, such as the use of a coriolis flow meter in conventional drilling, this requires extensive modifications to the return-flow line.

Coriolis flow meter

The coriolis flow meter is the most accurate (but also most expensive) flow measurement. Coriolis flow meters are sensitive to the presence of air or gas, and can not be

used in a open channel setting. Coriolis flow meters have been used for conventional drilling operations, but this requires extensive modification of the return-flow line. It is common to have coriolis flow meters in MPD operations. They have low sensitivity to changes in fluid composition and rheology, and do not require any external flow reference to be calibrated.

Differential pressure measurements

For closed circulation systems, differential pressure based flow measurements is very common and inexpensive, but has not seen much use in drilling operations. The last few years, these have been installed to be tested as a cheaper alternative to coriolis flow meters for MPD operations in MPD manifolds instrumented by Kelda Drilling Controls. They are found to be reasonably accurate around the operating flow, but as expected are inaccurate at very low flow. Initial designs were prone to plugging of the sensor ports by particles in the drilling fluid. If the option for a low cost MPD operation is no other measurements due to coriolis meter cost and footprint, then this is an inexpensive alternative. Differential pressure based flow estimation need a reference flow rate for calibration, where pump flow rate is used.

Paddle based flow meters

The paddle is the most commonly used flow meter for conventional drilling operations, consisting of a spring mounted paddle in the return line. The paddle gets deflected by the flow, and the deflection is measured. The paddle measurement is inexpensive and robust, but has the lowest accuracy of the alternatives. In practice, correlating the paddle deflection and actual flow rate requires continuous calibration, and even then accuracy is very low (+/- 15 %) [21]. Due to this, paddle measurements are most commonly used with a % deflection output, and this is used qualitatively to monitor the out flow for changes. Used in this way the paddle meter can be used as a qualitative measure for kick/loss detection, but the accuracy is too low to be used for estimating actual influx/loss rate and accumulated volume.

Rotating floating wheel flow meter

Developed at Sandia National laboratories [22] to deal with the challenges of the paddle flow meter for return measurements in drilling, this flow meter shows great potential [21], but has not been adopted by industry in any large volume. The rotating wheel flow meter consist of a rotating wheel that floats on top of the fluid surface, and thus measuring both liquid level and velocity. A schematic view of this flow meter can be seen in Fig. 1.6.

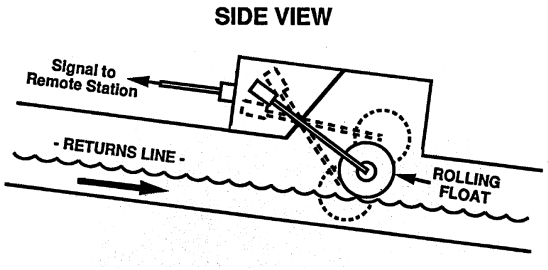

Figure 1.6: Rolling float flow meter, schematic from [22].

Venturi/Flume sub-critical open channel flow measurements

A possible way of measuring flow rates in open channels is by use of flume designs that make it possible to determine flow rate from liquid level. This is a well known and quite accurate approach used extensively in civil engineering. It might be possible to measure open channel flow in conventional drilling operations using this approach. This is covered in paper A and has been an area of significant research effort in recent years through the Sensors and models for improved kick/loss detection in drilling (Semi-Kidd) project at the University of South-Eastern Norway with among others Equinor as an industrial partner [23]–[25].

1.5 Influx management for managed pressure drilling

In some cases while doing managed pressure drilling, closing the BOP and performing traditional well control procedures might not be required as MPD equipment can deal with minor influxes. To determine whether to use MPD equipment or conventional well control has up until the 2000's been rather arbitrary and largely market specific. The Bureau of Safety and Environmental Enforcement (BSEE) suggested the MPD Well Control Matrix to help with this decision making, and although originally intended for the Gulf of Mexico, it is now adopted worldwide in most markets. An example of the WCM can be seen in Fig. 1.7.

The Influx Management Envelope (IME) is an extension of the WCM. The IME is a relatively modern concept, first described by Culen, Brand *et al.* [26] and now in use in the Gulf of Mexico. There has been a large number of conference articles on the subject of the IME, but no in depth articles on how to construct an IME with systematic derivation. This is covered in paper E.

	MPD Operating Matrix		
	Surface Pressure Limitations While Drilling		
	0 - 1250 psi	1250 - 2000 psi	> 2000 psi
No Influx or small Influx (gain less than 5 bb)	Normal operating	Stop drilling, P/U off bottom, Adjust MW to reduce surface pressure while maintaning BHP	Shut in on BOP, Secure Well Hand well control to rig Evaluate next planned action
Influx < 10 bbl	Stop drilling, P/U off bottom, Adjust system to increase BHP	Stop drilling, P/U off bottom, Adjust system to increase BHP and circulate out the influx	Shut in on BOP, Secure Well Hand well control to rig Evaluate next planned action
Influx > 10 bbl	Shut in on BOP, Secure Well Hand well control to rig Evaluate next planned action	Shut in on BOP, Secure Well Hand well control to rig Evaluate next planned action	Shut in on BOP, Secure Well Hand well control to rig Evaluate next planned action

Figure 1.7: Well Control Matrix.

1.6 Hydraulics modelling for drilling

There has been a significant research effort in the last decade on modelling the dynamics of the drilling process, especially in the context of estimation and control, see Stamnes [27], Hauge [28], Aarsnes [29] and Ambrus [30]. In general the system under consideration can be described by hyperbolic partial differential equations (PDEs) and what simplifications can be introduced in the context of modelling for control and estimation depends on the time scale of interest. In the following chapter, common models for the transient hydraulics while drilling will be summarized, separated into the single-phase (liquid only) and multi-phase cases.

1.6.1 Single-phase

The distributed dynamics for the single-phase case can be described by the 1-D isothermal Euler equations given in Eq. (1.4) if the effect of temperature on the system dynamics is neglected [30].

$$\begin{aligned} \frac{\partial \rho}{\partial t} + \frac{\partial \rho u}{\partial x} &= 0 \\ \frac{\partial \rho u}{\partial t} + \frac{\partial (\rho u^2 + p)}{\partial x} &= F + G \end{aligned} \tag{1.4}$$

Here ρ is density, u is velocity, p is pressure and F and G are source terms representing friction and gravity respectively. In drilling, the cross-sectional area of the flow conduit is not constant and a spatially varying cross sectional area should be considered. If varying cross sectional area of the flow path is considered, the isothermal

Euler Eq. (1.4) take the form of Eq. (1.5) where A is cross sectional area.

$$\begin{aligned} \frac{\partial \rho A}{\partial t} + \frac{\partial \rho u A}{\partial x} &= 0 \\ \frac{\partial \rho u A}{\partial t} + \frac{\partial ((\rho u^2 + p)A)}{\partial x} &= -p\frac{\partial A}{\partial x} + F + G \end{aligned} \tag{1.5}$$

Equation (1.4) has 3 unknowns, ρ, u, p but only 2 equations. To be uniquely solved, a closure law is required as given in Eq. (1.6), an equation of state (EOS) describing density as a function of pressure.

$$\rho = \rho(p) \tag{1.6}$$

For single phase systems a common and reasonably accurate choice for this is the linearized liquid EOS given in Eq. (1.7), where c_l is the speed of sound in the fluid and ρ_0 and p_0 the linearisation point density and pressure respectively [29].

$$\rho_l = \rho_0 + \frac{1}{c_l^2}(p - p_0) \tag{1.7}$$

There are numerous ways of solving Eq. (1.4) and Eq. (1.5), as well as simplifying the equations further. Equation (1.4) and Eq. (1.5) are strictly hyperbolic and nonlinear.

For the single phase case, the flow velocity will be low compared to the speed of sound. Assuming $u << c_l$, Eq. (1.4) can be made pseudo linear (in the case that F is still a nonlinear function of ρ and/or u). Inserting $\frac{\partial \rho}{\partial p} = \frac{1}{c_l^2}$, assuming near-incompressible and setting the ρu^2 term to zero, yields the water-hammer equations given in Eq. (1.8).

$$\begin{aligned} \frac{\partial p}{\partial t} + \rho c_l^2 \frac{\partial q}{\partial x} &= 0 \\ \frac{\partial q}{\partial t} + \frac{1}{\rho}\frac{\partial p}{\partial x} &= F + G \end{aligned} \tag{1.8}$$

A commonly used simplified model in the context of estimation and control is the one described by Kaasa, Stamnes *et al.* [1], and used extensively for both estimation and control design by Zhou [2] [19] [3], Stamnes [31] [32] [33], Stakvik, Berg *et al.* [4], [5] and Pavlov, Kaasa *et al.* [6].

The simplified model by Kaasa, Stamnes *et al.* [1] can be viewed as a water hammer model as given by Eq. (1.8), solved over two control volumes with one representing the drillstring and one representing the annulus using a staggered grid discretization in space. This yields two states for pressure, one in each control volume and one

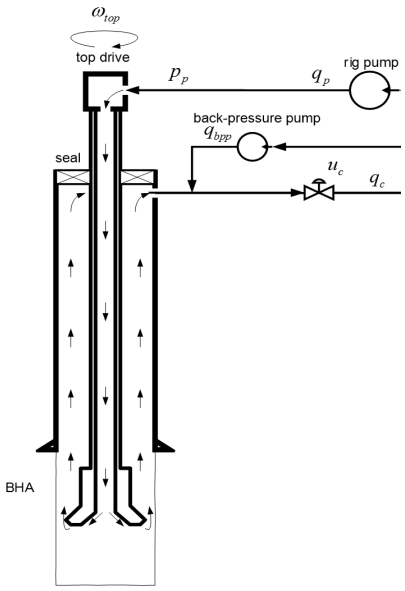

Figure 1.8: Simplified model schematic overview.

state for flow, at the interface between the control volumes. The model in [1] is given in Eqs. (1.9) to (1.13). As the model is primarily made for MPD applications, the outflow boundary condition is specified through a choke equation, Eq. (1.13). Figure 1.8 shows a schematic overview of the process.

$$\frac{V_d}{\beta_d}\frac{\mathrm{d}p_p}{\mathrm{d}t} = q_p - q_{bit} \tag{1.9}$$

$$\frac{V_a}{\beta_a}\frac{\mathrm{d}p_c}{\mathrm{d}t} = q_{bit} + q_{bpp} - q_c \tag{1.10}$$

$$M\frac{\mathrm{d}q_{bit}}{\mathrm{d}t} = p_p - p_c - F_d q_{bit}^2 - F_a q_{bit} \tag{1.11}$$

$$M = \int_0^{L_d} \frac{\rho_d}{A_d(x)}\mathrm{dx} + \int_{L_a}^{0} \frac{\rho_a}{A_a(x)}\mathrm{dx} \tag{1.12}$$

$$q_c = g_c(z_c)K_c\sqrt{\frac{2}{\rho}(p_c - p_{co})} \tag{1.13}$$

In Eqs. (1.9) to (1.13), V is volume, ρ is density, β is fluid bulk modulus $\beta = \frac{1}{\rho}\frac{\mathrm{d}\rho}{\mathrm{d}p}$ and A is area. The subscripts d and a represent the drillstring and annulus respectively. q is flow, with subscripts p and c representing pump and choke respectively. q_{bit} is a state representing flow from the drill string to the annulus, F_d and F_a are friction factors for the drill string and annulus, g_c is choke area as a function of choke position z_c.

1.6.2 Multi-phase

The Drift Flux Model has been extensively used to describe multi phase flows for drilling systems, due to its balance between predictive capabilities and simplicity. The drift flux model consist of two transport equations, and one mixture momentum equation, given in Eqs. (1.14) to (1.16) [29], [34]–[36].

$$\frac{\partial \rho_g \alpha_g}{\partial t} + \frac{\partial \rho_g \alpha_g v_g}{\partial x} = 0 \tag{1.14}$$

$$\frac{\partial \rho_l \alpha_l}{\partial t} + \frac{\partial \rho_l \alpha_l v_l}{\partial x} = 0 \tag{1.15}$$

$$\frac{\partial (\rho_l \alpha_l v_l + \rho_g \alpha_g v_g)}{\partial t} + \frac{\partial ((\rho_l \alpha_l v_l^2 + \rho_g \alpha_g v_g^2) + p)}{\partial x} = F + G \tag{1.16}$$

Equations (1.14) to (1.16) have 7 unknowns, and thus require 4 closure laws given in Eqs. (1.17) to (1.20) for the system to be uniquely solvable. How to calculate pressure, and thus the other primitive variables from the closure laws and conservative variables will be covered here in detail.

As the sum of liquid and gas volume fraction must be one, Eq. (1.17) must be satisfied. Treating both the liquid and the gas as compressible yields Eqs. (1.18) and (1.19). Gas velocity is found through the common K, S_∞ drift flux formulation by Zuber and Findlay [37] Eq. (1.20) with $K > 1, S_\infty > 0$.

$$\alpha_l + \alpha_g = 1 \tag{1.17}$$

$$\rho_l = \rho_l(p) \tag{1.18}$$

$$\rho_g = \rho_g(p) \tag{1.19}$$

$$v_g = K v_m^{sup} + S_\infty \tag{1.20}$$

Mixture superficial velocity is defined as Eqs. (1.21) to (1.23).

$$v_m^{sup} = v_l^{sup} + v_g^{sup} \tag{1.21}$$

$$v_g^{sup} = \alpha_g v_g \tag{1.22}$$

$$v_l^{sup} = \alpha_l v_l \tag{1.23}$$

Using Eqs. (1.17) to (1.19) and denoting $\rho_l \alpha_l$ as m_l and $\rho_g \alpha_g$ as m_g as these are known from Eqs. (1.14) and (1.15) yield:

$$m_l = \rho_l(p)(1 - \alpha_g) = \rho_l(p)(1 - \frac{m_g}{\rho_g(p)}) \tag{1.24}$$

$$m_l \rho_g(p) = \rho_l(p)(\rho_g(p) - m_g) \tag{1.25}$$

Combining these yield Eq. (1.26), an expression from which pressure can be found

$$\rho_l(p)\rho_g(p) - \rho_l(p)m_g - \rho_g(p)m_l = 0 \tag{1.26}$$

Commonly used with the following equations of state [29]

$$\begin{aligned} \rho_l &= \rho_0 + \frac{1}{c_l^2}(p - p_0) \\ \rho_g &= \frac{1}{c_g^2} p \end{aligned} \tag{1.27}$$

The DFM in Eqs. (1.14) to (1.16) with equations of state as given in Eq. (1.27) is nonlinear and strictly hyperbolic. There has been significant research work in recent years on explicit numerical solutions of the drift flux model, see [38]–[44].

The model introduced in Ambrus [30] and Ambrus, Aarsnes *et al.* [45] is in practice a two phase equivalent of the simplified model in Eqs. (1.10) and (1.13). It is derived by reduction of the DFM, yielding one PDE transport equation representing the transport of gas, with one ODE equation representing the conservation of mass in the annulus. For an in-depth derivation, the reader is referred to the appendix of [45]. For the Red-DFM model, the transport of gas in the annulus is described by a single PDE, given in Eq. (1.28).

$$\frac{\partial \alpha_g}{\partial t} + v_g \frac{\partial \alpha_g}{\partial x} = \frac{\alpha_g(\alpha_g - \alpha_l^*)}{(1-\alpha_l^*)\gamma p}\left(v_g \alpha_l \rho_l \left(g\cos(\theta) + \frac{2f(q_g+q_l)^2}{A^2 D}\right) - \frac{\partial p}{\partial t}\right) \tag{1.28}$$

where v_g is calculated by a slip law as given in Eq. (1.29).

$$v_g = \frac{v_m}{1-\alpha_l^*} + v_\infty \tag{1.29}$$

Here, α_l^* is a constant related to the gas concentration and velocity profile ($0 \leq \alpha_l^* < 1$) and v_∞ is the slip velocity. With the simplification $\dfrac{\partial p}{\partial t} \approx \dfrac{\mathrm{d}p_c}{\mathrm{d}t}$, the pressure at the choke is given by Eq. (1.30).

$$\frac{\mathrm{d}p_c}{\mathrm{d}t} = \frac{\bar{\beta}_a}{V_a}(q_l + q_g + T_{E_g} - q_c) \tag{1.30}$$

where effective bulk modulus of the system $\bar{\beta}_a$ is calculated as a function of the gas distribution as given in Eq. (1.31). T_{E_g} represents the additional liquid flow caused by the expansion of gas being transported up the annulus, calculated as Eq. (1.32).

$$\bar{\beta}_a = \frac{\beta_l}{1 + \frac{\beta_l}{V}\displaystyle\int_0^L \frac{A\alpha_g(\alpha_l - \alpha_l^*)}{(1-\alpha_l^*)\gamma p}\mathrm{d}x} \tag{1.31}$$

$$T_{E_g} = \int_0^L A\rho_l v_g \frac{\alpha_g \alpha_l (\alpha_l - \alpha_l^*)}{(1-\alpha_l^*)\gamma p} \left(g\cos(\theta) + \frac{2f(q_g+q_l)^2}{A^2 D} \right) \mathrm{d}x \tag{1.32}$$

The choke flow as a function of choke pressure is calculated as Eq. (1.33)

$$q_c = C_v z \sqrt{\frac{p_c - p_{co}}{\rho_l}} + \left(1 - \sqrt{\frac{\rho_g}{\rho_l}} \frac{1}{Y}\right) (A v_g(x) \alpha_g(x))|_{x=L} \tag{1.33}$$

1.7 Numerical solution of hyperbolic partial differential equations

The PDE models for single phase and the drift flux model are nonlinear hyperbolic PDEs. In general, numerical solution of such systems are not straight-forward[46]. There are numerous well known methods for solving PDEs of this type, all with advantages and disadvantages. If the timescale of interest is at the timescale of wave propagation for the fastest waves, explicit schemes are the most effective with respect to computing cost [47].

1.7.1 PDE analysis

PDEs such as Eq. (1.4), Eq. (1.8) and Eqs. (1.14) to (1.16) can be put in vector form as in Eq. (1.34) where U is the state vector, $F(U)$ is the flux function and $S(U)$ is the source vector.

$$\frac{\partial \mathrm{U}}{\partial t} + \frac{\partial}{\partial x}(F(\mathrm{U})) = S(\mathrm{U}) \tag{1.34}$$

Equation (1.34) can then be cast in quasi-linear form as in Eq. (1.35),

$$\frac{\partial \mathrm{U}}{\partial t} + A(\mathrm{U}) \frac{\partial \mathrm{U}}{\partial x} = S(\mathrm{U}) \tag{1.35}$$

where $A(U)$ is the Jacobian of $F(U)$, Eq. (1.36)

$$A(\mathrm{U}) = \frac{\partial F(\mathrm{U})}{\partial \mathrm{U}} \tag{1.36}$$

The eigenvalues of the Jacobian $A(U)$, λ is used to classify the PDE.

If all eigenvalues $\lambda_1, \lambda_2, ...\lambda_n$ are real, the system is hyperbolic, if all are real and distinct, the PDE is strictly-hyperbolic. Both the isothermal Euler equations and the drift flux model can be shown to be strictly hyperbolic.

For the isothermal Euler equations, introducing temporary parameter u_1 and u_2

$$\mathrm{U} = \begin{bmatrix} \rho \\ \rho u \end{bmatrix} = \begin{bmatrix} u_1 \\ u_2 \end{bmatrix} \tag{1.37}$$

$$A(\mathrm{U}) = \frac{\partial F(\mathrm{U})}{\partial \mathrm{U}} = \begin{bmatrix} 0 & 1 \\ -\frac{u_2^2}{u_1^2} + \frac{\partial p}{\partial \rho} & 2\frac{u_2}{u_1} \end{bmatrix} \tag{1.38}$$

It can be found that the eigenvalues of $A(U)$ are $\lambda_{1,2} = u \pm \sqrt{\frac{\partial p}{\partial \rho}}$ where u is velocity and $\sqrt{\frac{\partial p}{\partial \rho}}$ is the speed of sound in the fluid.

For the DFM, a full analysis is not performed here. For a thorough analysis the reader is referred to Evje and Flåtten [43], as well as papers B and C.

The drift flux model can be shown to have $\lambda_1 = u_g$, $\lambda_{2,3} = u_l \pm c_m$.

For numerical solutions of PDEs, how big variations is encountered in the mixture sound velocity should be considered. Some schemes are very sensitive to the time step size versus local propagation velocity with respect to numerical diffusion. The drift flux model has a mixture sound velocity that is a highly nonlinear function of gas volume fraction α_g as see in Fig. 1.9, making this especially relevant.

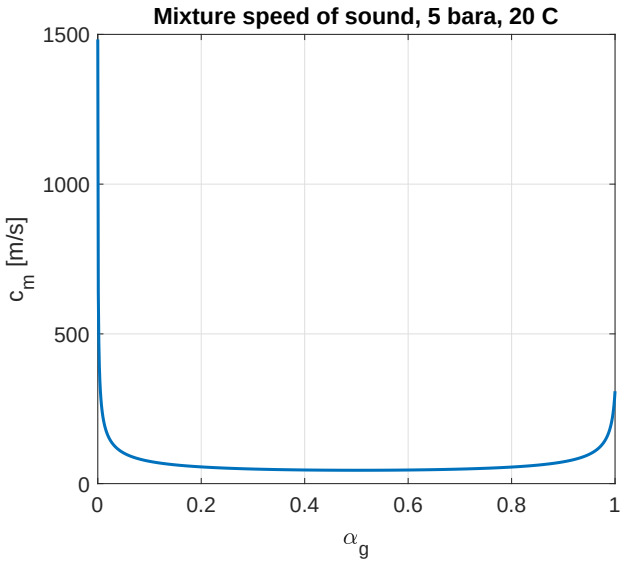

Figure 1.9: Mixture sound velocity, Drift flux model

1.7.2 Numerical solution

Hyperbolic PDEs of the form:

$$\frac{\partial \mathrm{U}}{\partial t} + \frac{\partial}{\partial x}(F(\mathrm{U})) = 0 \tag{1.39}$$

are typically solved explicitly through conservative schemes of the form in Eq. (1.40) [46].

$$\mathrm{U}_i^{n+1} = \mathrm{U}_i^n - \frac{\Delta t}{\Delta x}(\mathscr{F}(\mathrm{U}_{L,i+1/2}^n, \mathrm{U}_{R,i+1/2}^n) - \mathscr{F}(\mathrm{U}_{L,i-1/2}^n, \mathrm{U}_{R,i-1/2}^n)) \tag{1.40}$$

where n represent discrete time steps, i discrete points in space, the subscripts L, R the left- and right- hand side of the interface respectively and $\mathscr{F}(U_L, U_R)$ is found from a scheme specific numerical flux, or exact or approximate Riemann solver. A schematic representation of the spatial distribution of states can be seen in Fig. 1.10.

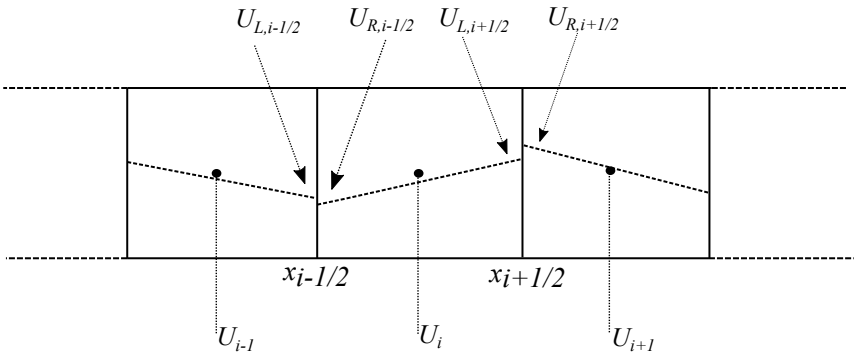

Figure 1.10: Scheme Schematic.

For a first order scheme, the states at the interfaces are approximated as

$$\begin{aligned} U_{L,i+1/2}^n &= U_i^n \\ U_{R,i+1/2}^n &= U_{i+1}^n \\ U_{L,i-1/2}^n &= U_{i-1}^n \\ &\text{and} \\ U_{R,i-1/2}^n &= U_i^n \end{aligned} \tag{1.41}$$

yielding Eq. (1.42) when inserted in Eq. (1.40).

$$\mathrm{U}_i^{n+1} = \mathrm{U}_i^n - \frac{\Delta t}{\Delta x}(\mathscr{F}(\mathrm{U}_i^n, \mathrm{U}_{i+1}^n) - \mathscr{F}(\mathrm{U}_{i-1}^n, \mathrm{U}_i^n)) \tag{1.42}$$

One very typical first order scheme, used extensively in introductory material to hyperbolic PDEs is the Lax Friederichs scheme (LxF)[46], given in the conservative form in Eq. (1.43).

$$\mathscr{F}(\mathrm{U}_L, \mathrm{U}_R) = \frac{f(\mathrm{U}_R) + f(\mathrm{U}_L)}{2} - \frac{\Delta x}{2\Delta t}(\mathrm{U}_R - \mathrm{U}_L) \tag{1.43}$$

The LxF scheme, although good for illustrating basic numerical techniques is very diffusive. A drastically improved version of the LxF scheme is the local Lax Friedrichs

or Rusanov Scheme, given in Eq. (1.44) [46].

$$\mathscr{F}(\mathrm{U}_L, \mathrm{U}_R) = \frac{f(\mathrm{U}_R) + f(\mathrm{U}_L)}{2} - \frac{\lambda}{2}(\mathrm{U}_R - \mathrm{U}_L) \tag{1.44}$$

Where $\lambda = \rho(A(\mathrm{U})) = \max(|\,\lambda_i\,|\,...\,|\,\lambda_n\,|\,|$ is the spectral radius of $A(\mathrm{U})$, the Jacobian of $F(\mathrm{U})$

First order centred schemes as in Eq. (1.43) and Eq. (1.44) usually perform poorly at capturing sharp interfaces when compared to first order exact or approximate Riemann solvers. Although diffusive, these relatively simple centred schemes form a fundamental building block in many modern high-resolution schemes that have more than first order spatial accuracy.

It seems tempting to use higher order approximations than those given in Eq. (1.41). Sadly, it is not that simple, and doing higher than first order approximations in Eq. (1.41) results in a numerical phenomena called "Spurious Oscillations" in high gradient regions of the solution. Godunovs Theorem states [46]:

"Linear numerical schemes for solving partial differential equations (PDEs), having the property of not generating new extrema (monotone scheme), can be at most first-order accurate"

There are two approaches to gain higher than first order resolution without spurious oscillations, namely:

- Van Leer's MUSCL (Monotonic Upwind Scheme for Conservation Laws) [48]
- WENO/ENO schemes (Weighted Essentially non-Oscillatory) [49]

Van Leer's MUSCL (Monotonic Upwind Scheme for Conservation Laws) achieves this through adapting the derivatives used to reconstruct the solution or fluxes at the interface through a nonlinear limiting function termed flux- or slope- limiter for the case of limiting fluxes or states respectively. [48]:

For a second order MUSCL slope limiter scheme the solution on the interfaces $\mathrm{U}^n_{R,i-1/2}, \mathrm{U}^n_{L,i-1/2}$ is approximated by Eq. (1.45).

$$\begin{aligned} \mathrm{U}^n_{R,i-1/2} &= \mathrm{U}^n_i - \frac{\Delta x}{2}\mathrm{U}^{\mathrm{n}}{}_x \\ \mathrm{U}^n_{L,i-1/2} &= \mathrm{U}^n_{i-1} + \frac{\Delta x}{2}\mathrm{U}^{\mathrm{n}}{}_x \end{aligned} \tag{1.45}$$

Here, U^n_x is a flux limited spatial derivative of the solution U^n.

Defining the slopes a, b as

$$a = \frac{\mathrm{U}_i - \mathrm{U}_{i-1}}{\Delta x} \tag{1.46}$$

$$b = \frac{\mathrm{U}_{i+1} - \mathrm{U}_i}{\Delta x} \tag{1.47}$$

U_x can be found as

$$\mathrm{U}_x = \phi(a,b) * a \tag{1.48}$$

Where $\phi(a,b)$ is a slope limiter satisfying Eq. (1.49) [50]

$$\begin{aligned} \frac{a}{b} \leq \phi(a,b) \leq 2\frac{a}{b} \qquad & (0 \leq \frac{a}{b} \leq 1) \\ 1 \leq \phi(a,b) \leq \frac{a}{b} \qquad & (1 \leq \frac{a}{b} \leq 2) \\ 1 \leq \phi(a,b) \leq 2 \qquad & (\frac{a}{b} > 2) \end{aligned} \tag{1.49}$$

such as the minmod slope limiter

$$\phi(a,b) = \max(0, \min(1, \frac{a}{b})) \tag{1.50}$$

Applying this to the Lax Friedrich's, Eq. (1.43), Rusanov, Eq. (1.44) and and a two wave-speed improved Rusanov like scheme yields the schemes derived in detail by Nessyahu and Tadmor [51], Kurganov and Tadmor [52] and Kurganov, Noelle *et al.* [53], respectively.

Semi discrete schemes

For model order reduction, schemes that can be put in semi-discrete form (where only space is discretized) are advantageous (and in some cases required). Taking the limit of $\Delta t \to 0$ in Eq. (1.39) yields the semi discrete form:

$$\frac{\partial \mathrm{U}}{\partial t} = -\frac{1}{\Delta x}(\mathscr{F}(\mathrm{U}^n_{L,i+1/2}, \mathrm{U}^n_{R,i+1/2}) - \mathscr{F}(\mathrm{U}^n_{L,i-1/2}, \mathrm{U}^n_{R,i-1/2})) \tag{1.51}$$

For numerical schemes where Δt is part of the numerical flux function $\mathscr{F}(U_L, U_R)$, the semi-discrete form of Eq. (1.39), Eq. (1.51) might not be possible, such as for the Lax-Friedrichs scheme in Eq. (1.43) where $\lim_{\Delta t \to 0} \mathscr{F}(U_L, U_R) = \pm\infty$.

The schemes derived in Kurganov and Tadmor [52] and Kurganov, Noelle *et al.* [53] admit a semi-discrete form.

Well balanced schemes

Most numerical schemes for strictly hyperbolic nonlinear PDEs do not consider source terms that appear if one considers friction, gravity and varying flow path area. Usually, the drift flux model considers the flow cross sectional area to be constant along the flow path, something that is not true in most drilling operations. Adding source terms to the PDE and using a scheme not designed for source terms does not necessarily work well. A commonly used approach to dealing with source terms is to perform Godunov splitting in time [46]. Although this works well for transient stability, it does introduce spurious non-physical phenomena in the steady state solution. A numerical scheme that if initialized on the steady state solution with source terms, and the numerical solution stays on the steady state solution without changing, is termed well balanced.

Work on a explicit numerical scheme for the DFM that can handle changes in cross sectional area is performed in paper B as well as gravity and friction in paper C.

2 Main contributions

This chapter summarize the main results of the included papers, and put them in context. Where more recent work has been performed after the publication of the papers, this work is also summarized. The chapter is split into four subchapters, where each subchapter deal with a specific topic.

- Subchapter 2.1 presents the work in Paper A, a feasibility study for the use of a novel return-flow measurement principle for conventional drilling.
- Subchapter 2.2 presents the work in Papers D and F. Here the accuracy for the distributed and simplified models for the drilling hydraulics is compared with field data for fast and slow transients. Further, the feasibility of using the simplified model for MPD controller design, and the feasibility of using a cascade control structure is shown on a real drilling operation.
- In subchapter 2.3 the results of Papers B, C and G is summarized. Papers B and C deal with the design of a well balanced semi-discrete schemes for DFM. Recent approaches to creating well-balanced schemes for other PDE systems, notably the Euler equations for gas dynamics is applied to the DFM. Then the feasibility of using a control structure based on the simplified model is shown to work in multiphase case. Paper G shows performance of the controller during multiphase conditions on a real well, but extensive testing was performed on models similar to those described in Papers B and C prior to operation.
- Subchapter 2.4 presents the work in Paper E. The Influx Management Envelope (IME) is a relatively new concept for well control in MPD operations. The paper systematically derive the IME from first principles, and show that it can be calculated with real-gas Equations of State (EOS's) if numerical solution is used. To the authors knowledge Paper E is the first peer-reviewed journal-length article that systematically deals with the IME.

2.1 Return flow measurement

Using open channel geometries that force sub-critical flow conditions and using this for estimating flow-rate is something that has been used for more than a century. To

the best of my knowledge, this approach has never been attempted for flow measurements of the return flow while drilling. Open channel flumes are especially interesting for conventional drilling operations, as the measurement principle is based on open channel flow; traditionally one of the challenges with flow measurement for conventional drilling.

The main limiting factor for good kick loss detection in conventional drilling operations is the quality of the return flow measurement, and improving the accuracy of this sensor would be of great importance to more advanced kick/loss detection [15]. Installing coriolis flow meters in conventional drilling is possible, but requires so extensive modifications to the return flowline that this is rarely done. It might be possible to install a flume design with acceptable footprint and modification on the rig.

In paper A, the possibility of using a flume design for flow rate estimation is discussed. Multiphase Volume of Fluid (VOF) Computational Fluid Dynamics (CFD) simulations of different flow rates of both water and non-Newtonian mud was performed for a commercially available ISO 4359 venturi flume. It was found that CFD simulations fit well with the manufacturer specifications of flow-rate versus fluid level.

There has been a significant amount of work on the possibility of using a venturi flume for flow rate estimation for drilling in recent years through the "Sensors and models for improved kick/loss detection" (SEMI-KIDD) project at the University of South-Eastern Norway (USN). A full scale experimental rig has been built and multiple PhD theses have been defended on this in particular.

Welahettige [24] has performed CFD simulations, with validation against experimental data for both Newtonian and non-Newtonian fluids continuing the work from paper A in [54], [55]. He has also performed multiphase simulations with both solid (cuttings), liquid, and gas phases to study potential cuttings settling problems in [56]. Work on the simplified 1-D shallow water equations, similar to the isothermal Euler equations has also been done using a second order Flux Limiter Centered (FLIC) numerical scheme in [57] and found to fit reasonably well with both CFD simulations and experimental data.

Agu has done work on the simplified 1-D shallow water equations, showing good agreement with experimental data in [58]. He has also designed a flow estimation algorithm based on this model in [59], showing promising estimation accuracy when used with experimental data.

Chhantyal [25] has looked at possible flow rate estimation techniques, for a venturi Flume, using sensor fusion and artificial neural networks (ANN's) with multiple venturi level measurements, showing good agreement between estimated and measured flow rate for the experimental venturi flume.

Jinasena [23] has performed 1-D simulations of the flume using the second order scheme described by Kurganov and Petrova [60], model order reduction of this model in [61] as well as studied different approaches for flow rate estimation. She has developed model based real-time estimators with real time estimation of friction factors in the venturi flume showing good agreement between estimated flow in the venturi flume compared to measurements in the experimental rig.

The study done in paper A as well as subsequent work, still show the feasibility of using flume designs in the return line for flow rate estimation in conventional drilling operations. Results from the experimental rig show that good accuracy can likely be achieved, and significantly more accurate than using a paddle. A drastic change in the quality of the return flow measurement opens up a new world of possibilities for robust kick/loss detection in conventional drilling operations.

Flume designs have still not been tested in practice in real operations, but design and simulations for a venturi flume is ongoing, with field trials by Kelda Drilling Controls likely within a year.

The main challenges with respect to flume design for rig installation, is that the length available for having a horizontal flume is limited, leading to less inlet section than what is typically recommended. It is believed that systematic and iterative design coupled with CFD simulations can largely overcome this problems.

2.2 Hydraulics modelling and pressure control, single phase

Although there are a number of publications in recent years on control and estimator designs on the model in Eqs. (1.9) to (1.13) there is almost no publications on real operational use of these. For the controller Kelda Drilling Controls use, the design was based on the model in Eqs. (1.9) to (1.13). During controller development, extensive testing was also performed on a simulated well, based on the isothermal Euler equations PDE model in Eq. (1.5).

As the entire control system was developed and tested against the simulator only up until the first field operation, significant trust is put in the simulation model to represent real life. This is the topic of paper D.

For the isothermal Euler equations as well as multiphase models, an equation of state for the liquid is required, typically a function of fluid bulk modulus β or the liquid speed of sound c_l. Drilling muds are composite fluids consisting of both solids, water and/or oil. A mixture equivalent bulk modulus or speed of sound can be calculated for this system if component volume fractions are known. An example from paper D of comparison between the simplified model, a PDE model, and recorded data for fast transients where wave propagation delays are apparent can be seen in Fig. 2.1.

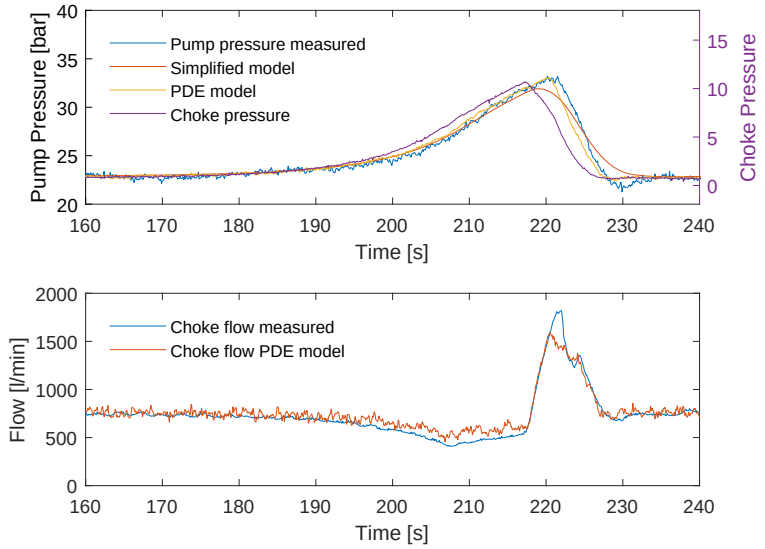

Figure 2.1: Simplified model versus PDE and reality, fast transients.

In paper D, the mixture bulk modulus β_m is used in comparing the PDE model in Eq. (1.5) as well as the simplified model of Eqs. (1.9) to (1.13) to data from commissioning an MPD control system offshore. It is found that the mixture bulk modulus does not fit well with the recorded data. Fluid structure interactions (FSI) are then considered, yielding a new equivalent bulk modulus β_e that improves the accuracy of the PDE model. An example of the effect of considering simple FSI in the PDE model can be seen in Fig. 2.2. It is still found that pressure wave propagation time from choke to pumps differ in the PDE model from the recorded data. Treating β as a unknown parameter can make the wave propagation time, or the dynamic flow response of the system fit, but not both, indicative that something fundamental might be missing in the PDE model.

For MPD control systems, having control of downhole and pump pressure directly would be beneficial. In paper F a simple cascade control structure is suggested, where the inner controller controlling choke pressure is based on the model in Eqs. (1.9) to (1.13) and downhole pressure is controlled using a cascaded PI controller, providing the set-point for p_c. The controller implementation and design is described in more detail in [4], [5]. This was tested extensively on a model similar to that described in paper D and performance was found to be acceptable.

The controller was then deployed in a commercial MPD package, and the author was part of system setup and testing during the first operation of the controller outside Dubai in the United Arab Emirates. The PDE model was also extensively used during training on the control system, and employed as a digital twin during initial system setup.

In paper F it is shown that the model in Eqs. (1.9) to (1.13) is adequate for controller

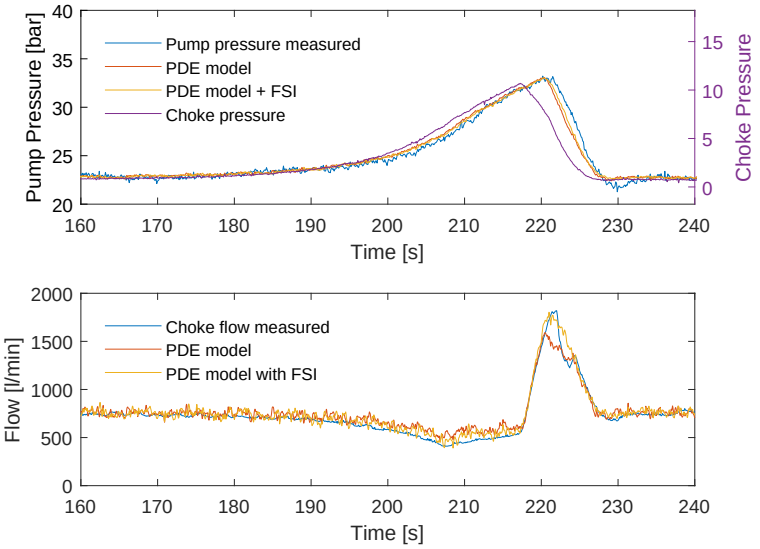

Figure 2.2: Fluid mixture bulk modulus and simple FSI equivalent bulk modulus in PDE model versus recorded data.

design for single phase MPD systems, re-affirming the findings by Pavlov, Kaasa *et al.* [6] and Godhavn, Pavlov *et al.* [62]. An example of reference tracking performance of the controller based on the simplified model can be seen in Fig. 2.3.

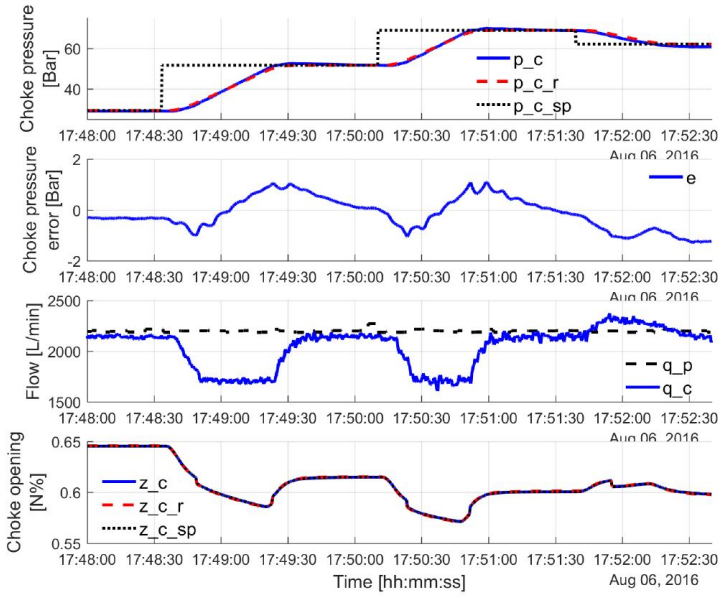

Figure 2.3: Choke pressure set point steps, controller based on simplified model.

One has to be careful of judging controller performance of model-based controllers with simulation on the design model. At best it shows that the implementation is

as intended, and does not prove real life performance. Especially in the case where Eqs. (1.9) to (1.13) is used for design, the fact that this model neglects pressure wave propagation and reflection should be respected. Through the design process and first operation covered by paper F it is shown that employing a model of the fidelity of the PDE model in paper D as a test environment for control design is close enough to real system response.

Paper D shows that bulk modulus as a tuning parameter is not able to accurately capture both wave propagation time and flow response at the same time. This might be important in the context of controller and estimator designs on the PDE itself, something that has had a significant focus in recent years. Although the PDE model is accurate enough for testing purposes on designs based on simpler models, it is uncertain whether the deviation from reality observed might affect PDE based designs.

Paper D does model comparison with data from a small time period on one well, but the finding of the inability of β as the only free parameter to accurately capture wave propagation time and flow dynamics has been observed on multiple wells. A more systematic comparison of the PDE model against field data for cases where transients are fast enough to excite wave dynamics should be performed. It is shown that considering FSI can remove some of the guesswork in the β parameter, but possible modifications to the PDE model to accurately describe both wave propagation time and flow response should be performed. One possible approach here could be comparison of compressible liquid CFD simulations in symmetric 2D geometries to the 1D model to confirm or disprove the importance of 2D effects on the wave propagation velocity.

2.3 Hydraulics modelling and pressure control, two phase

Modelling of multiphase flows can be challenging, and there is multiple possible 1-D models, ranging from the complex model of Baer and Nunziato, through the two fluid, drift flux (DFM) and reduced drift flux model [63]. In general, the drift flux model has been shown to have a reasonable balance between complexity and prediction accuracy [34], [36], [63], [64]. Through cooperation with the EU project Hydralics Modeling for Drilling Automation (HYDRA), work was done on numerical solution of the DFM, aimed a finding a reasonably accurate, simple to implement scheme admitting a semi discrete form. Numerous approaches to deal with non-conservative source term were studied. I contributed with literature review, design of schemes, implementation as well as design of test cases, interpretation of results and critical review in papers B and C.

The DFM traditionally assumes a constant cross sectional area along the flow path. In drilling operations this is not the case, and the presence of sharp changes in

cross sectional area affect both the transport velocity and lead to partial reflection of pressure waves. When the drift flux model is put in the form admitting changes in cross sectional area, as given in Eq. (2.1) the source term $-p\frac{\partial A}{\partial x}$ appears in the mixture momentum equation. Note that friction and gravity, the F and G terms in Eq. (1.16) are not considered here.

$$\begin{aligned}
\frac{\partial \rho_l \alpha_l A}{\partial t} + \frac{\partial \rho_l \alpha_l v_l A}{\partial x} &= 0 \\
\frac{\partial \rho_g \alpha_g A}{\partial t} + \frac{\partial \rho_g \alpha_g v_g A}{\partial x} &= 0 \\
\frac{\partial((\rho_l \alpha_l v_l + \rho_g \alpha_g v_g)A)}{\partial t} + \frac{\partial(((\rho_l \alpha_l v_l^2 + \rho_g \alpha_g v_g^2) + p)A)}{\partial x} &= -p\frac{\partial A}{\partial x}
\end{aligned} \tag{2.1}$$

The addition of this source term, although seemingly trivial, complicates matters when it comes to numerical solution. Conservative schemes in the form of Eq. (1.40) often does not handle this well. Stability can often be helped by Godunov splitting, but this still leads to problems in the resulting steady state solution [46]. There has been a significant research effort on tackling a problem very similar to this for the Shallow-water equations, and scheme modifications that is both robust and captures the correct steady state exist for these equations, see for instance Kurganov and Petrova [60]. There has also been fundamental work on scheme modifications for tackling non-constant cross sectional area for the Euler equations, a 3-PDE system very similar to the DFM [65], [66].

In paper B, multiple scheme modifications of the Rusanov scheme are tested on the DFM to handle spatially changing cross sectional area. One of multiple test cases consists of two connected pipes at different diameter, with a constant inflow of liquid and gas, as seen in Fig. 2.4

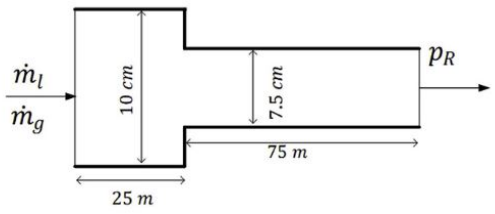

Figure 2.4: Variable geometry test case.

The presence of this discontinuous change in cross sectional area will lead to non-physical numerical artifacts developing at the point where the cross sectional area changes, if not handled in a special manner. The result of the naive approach, with no scheme modifications and solved with the Rusanov scheme can be seen in Fig. 2.5.

The numerical scheme was then modified by the method proposed by Clain and Rochette [65] for the Euler equations, but adapted to the DFM. This approach

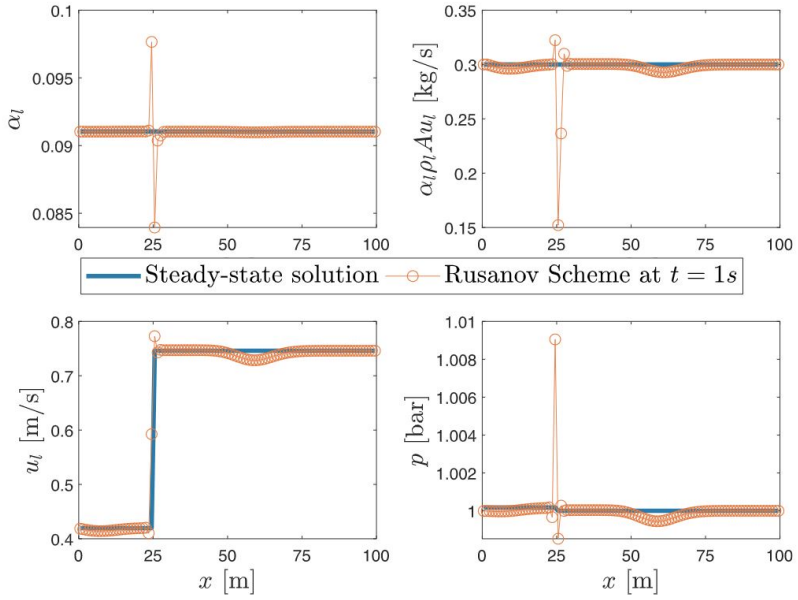

Figure 2.5: Variable geometry test case, naive approach to sources.

was also further extended. Then the approach by Kröner and Thanh [66] was implemented for the DFM. In this approach, the PDE is solved in its normal form, without the area term in the PDE, and then the effect of area variation is captured by an intermediary calculation step. Out of all possible approaches, the one by Kröner and Thanh [66] was the most successful and the result of this for the DFM and the test case in Fig. 2.4 can be seen in Fig. 2.6. Perfect fit with the steady state solution using this approach for the DFM was not achieved even though this was achieved by Kröner and Thanh [66] for the Euler equations. This can be observed in the top right plot of Fig. 2.6. The reasons for this is discussed in paper B, and is linked to the difficulty of solving jump conditions across the interface in the presence of a slip law. The achieved accuracy in capturing the steady state is sufficient for most practical purposes. The approach of Kröner and Thanh [66], but modified to the DFM is also scheme independent, such that the findings and suggested modifications in paper B can be applied to any scheme that can be put in the conservative form of Eq. (1.40).

Discontinuous changes in cross sectional area does not only affect the steady state solution of the system, but also leads to partial reflection of waves, something that changes the transient response. An example of this can be seen in Fig. 2.7. Here the test geometry of Fig. 2.4 (top) is compared to that of a straight pipe, with a step in the inlet boundary conditions, leading to a travelling wave that is partially reflected in the changing geometry case.

When gravity and friction is considered in the DFM, the same problems as for changing cross sectional area appear. Creating well-balanced schemes for the Euler

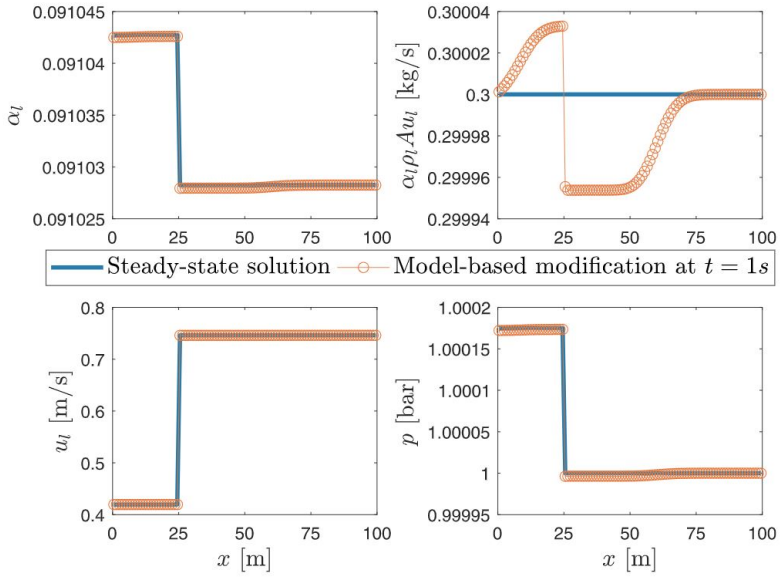

Figure 2.6: Variable geometry test case, proposed scheme.

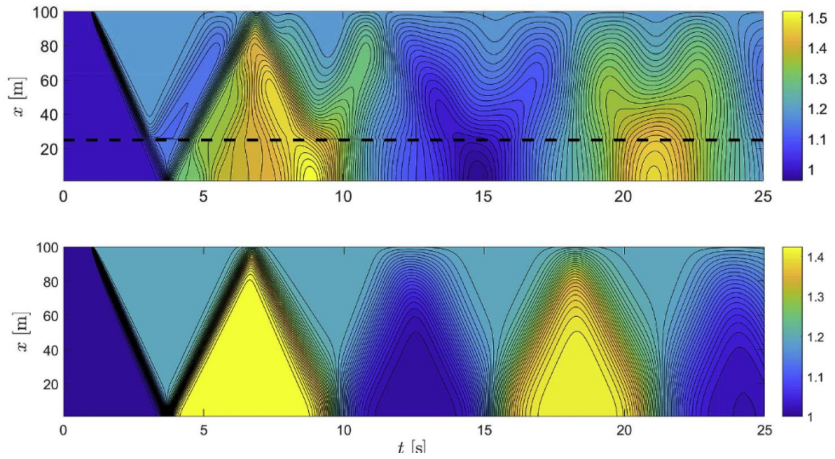

Figure 2.7: Wave reflection in multiphase flow.

equations with gravity has been done by Käppeli and Mishra [67] and Chertock, Cui *et al.* [68]. In paper C, the ideas of Kröner and Thanh [66] is applied to the isothermal Euler equations as well as the DFM for creating a well balanced scheme with friction and gravitation. A test case is defined with flow up a pipe against gravity, as seen in Fig. 2.8. Suggested scheme modifications are tested out with respect to preservation of steady state.

Figure 2.9 shows the test case in Fig. 2.8 for the isothermal Euler equations and zero flow. The result without any special treatment of the source terms show that mass-flow rate increases along the length of the pipe without any inlet flow (and

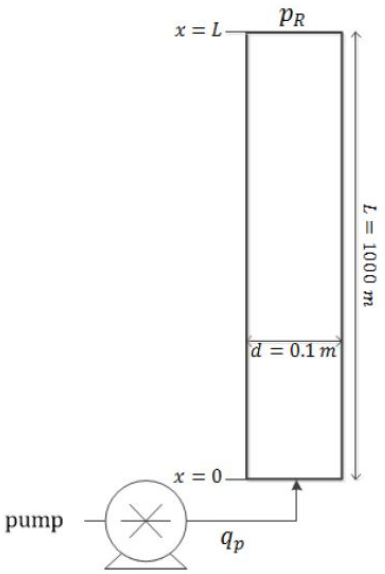

Figure 2.8: Test case, friction and gravity source terms.

thus friction), violating conservation of mass. This is caused by the gravity source term. The proposed well-balanced scheme stays on the steady state, without the unphysical creation of mass in the unmodified scheme.

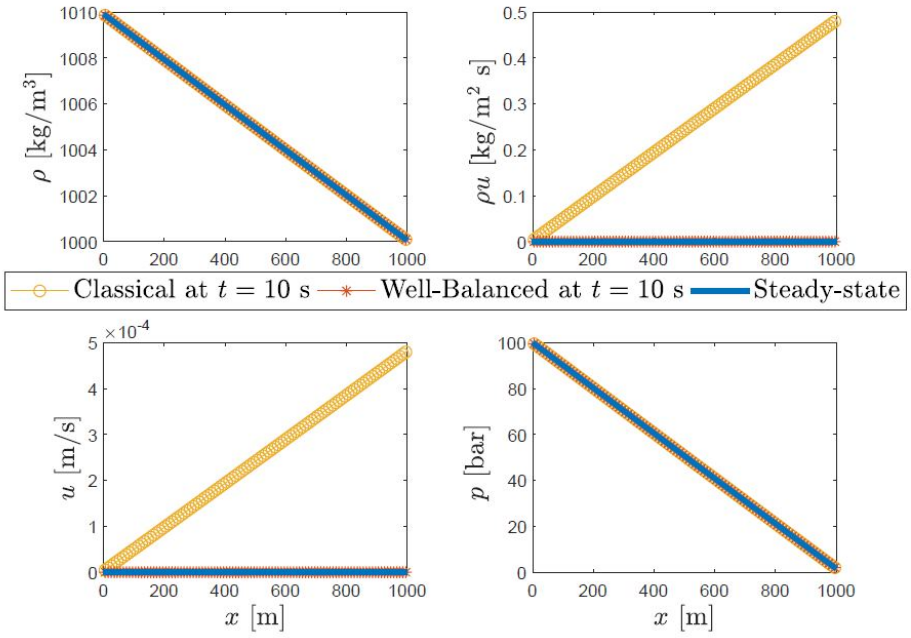

Figure 2.9: Isothermal Euler equations with gravity and friction, zero flow.

Figure 2.10 shows the test case in Fig. 2.8, with flow. The same trend of increasing mass flow along the pipe is observed without any special treatment of the source term.

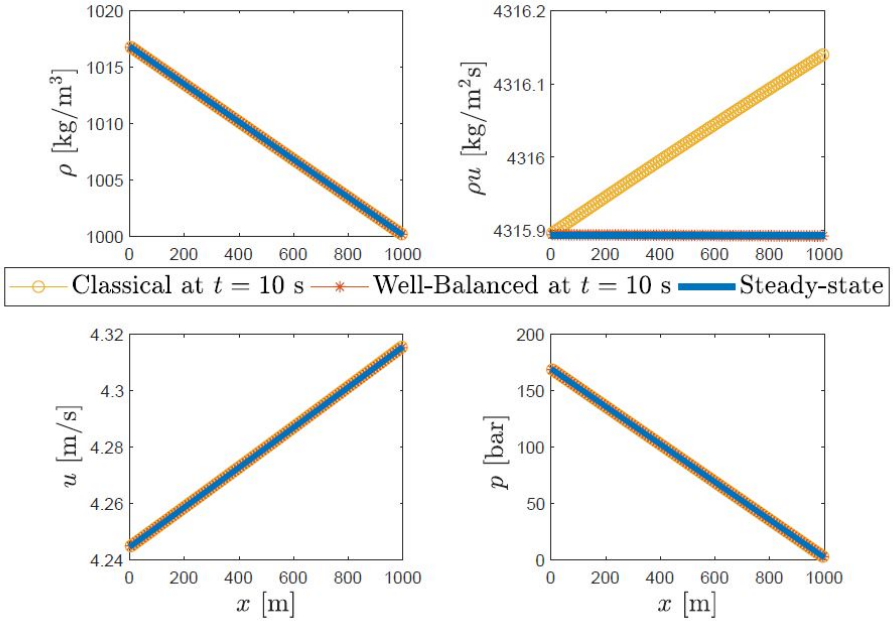

Figure 2.10: Isothermal Euler equations with gravity and friction, flow.

Figure 2.11 shows the test case in Fig. 2.8 with flow for the DFM. Results are similar to those in the isothermal Euler equation test cases. No special treatment of the source terms leads to violating conservation of mass, with a growing mass flow along the length of the pipe.

The proposed scheme in paper C based on the Rusanov scheme makes it possible to include friction and gravity source terms in the DFM, without the non-physical violation of conservation off mass observed if there is no special treatment of sources. The approach is scheme specific, such that the results in paper C cannot be directly used for other schemes than the Rusanov scheme. The derivation in paper C should be possible to follow for other schemes. This makes paper C relevant for other schemes than Rusanov, illustrating a procedure of constructing well balanced schemes for the DFM with friction and gravitation.

The scheme modifications in paper B and paper C can be applied independently, thus giving a Rusanov scheme for the DFM that is able to handle both changing cross sectional flow area, as well as friction and gravitation, without introducing unphysical deviation from the steady state.

For control under multiphase conditions, the largest change to system dynamics in terms of the simplified model in Eqs. (1.9) to (1.13) is the increased compressibility of

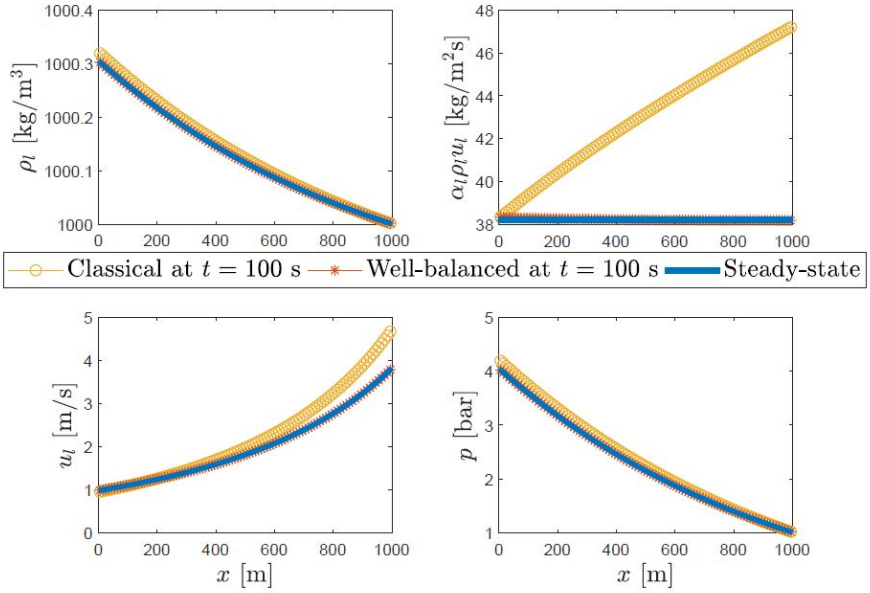

Figure 2.11: DFM equations with gravity and friction, flow.

the system. If comparing the ODE representing the choke pressure in the simplified model of Eq. (1.13), what the controller in paper F is based on and re-stated here for simplicity

$$\frac{\mathrm{d}p_c}{\mathrm{d}t} = \frac{\beta_a}{V_a}(q_{bit} + q_{bpp} - q_c) \tag{2.2}$$

with the choke pressure ODE in the Red-DFM from [45],

$$\frac{\mathrm{d}p_c}{\mathrm{d}t} = \frac{\bar{\beta}_a}{V_a}(q_l + q_g + T_{E_g} - q_c) \tag{2.3}$$

these two models are very similar. In the Red-DFM the effective bulk modulus $\bar{\beta}_a$ is calculated as a function of the gas distribution in the well. q_g represents gas flow over the chokes, found from the gas transport PDE, and T_{E_g} represents additional liquid flow due to gas expansion in the well. The controller in paper F has an integral term accounting for un-modelled flows and errors in the choke equation in Eq. (1.13). The terms q_g and T_{E_g} in the Red-DFM are relatively slowly changing compared to the integral action in the controller.

For a possible control approach, it was tested to see if the controller used in paper F, based on the simplified model in Eqs. (1.9) to (1.13), could work in multiphase conditions. To achieve this, annulus bulk modulus β_a, representing system compressibility, was treated as a changing and unknown parameter with an adaptive law. When testing this approach on a DFM model, controller performance was reasonable and robust, further leading to flow loop tests of the controller with nitro-

gen injection to test controller capabilities under multiphase conditions as described in [4]. Flow loop tests verified the findings from multiphase simulations.

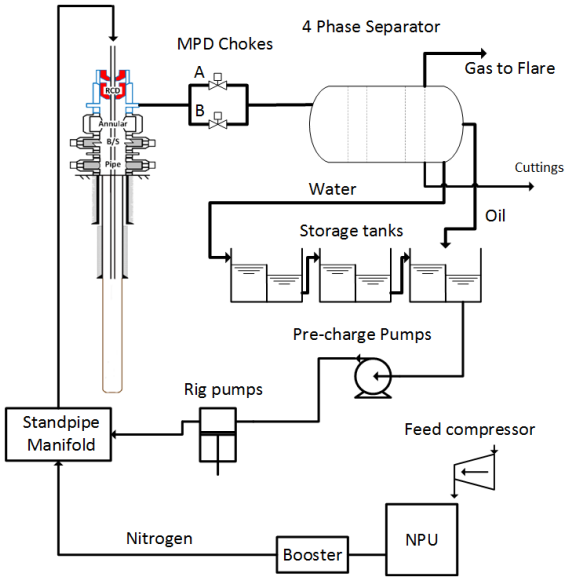

Figure 2.12: Equipment setup UBD with MPD control system.

An under-balanced drilling (UBD) operation in Siberia provided the perfect testing grounds for the multiphase capabilities of the model-based controller. The findings from the operations is described in full in paper G. The equipment setup can be seen in figure Fig. 2.12. Four wells were drilled with a combination of water with N2 injection, crude oil and crude oil with reservoir gas, and all wells transitioning between at-balance MPD and under-balanced drilling. The MPD controller was left largely unmodified, with the exception of an adaptive law on β_a.

The operation showed that the controller with adaptive β_a remained robust and with reasonable performance. This shows that from a controller design view, the simplified model in Eqs. (1.9) to (1.13) is still adequate for design in the multiphase case, as long as the changes in system compressibility is accounted for. To the authors knowledge the operation in paper G is the first ever UBD operation where a MPD system with a high level of automation was used.

Figure 2.13 shows the controller performance for a set point step in back pressure under multiphase conditions. Notice the large time delay from the applied choke pressure, to the change in standpipe pressure (top plot) due to the low speed of sound caused by the gas in the system. Choke pressure changes relatively slowly for even large changes in choke opening compared to single phase operations. This is caused by the drastically increased compressibility of the system, handled in the controller by adapting annulus bulk modulus β_a.

Figure 2.14 shows the use of automatic standpipe control, based on a cascade control

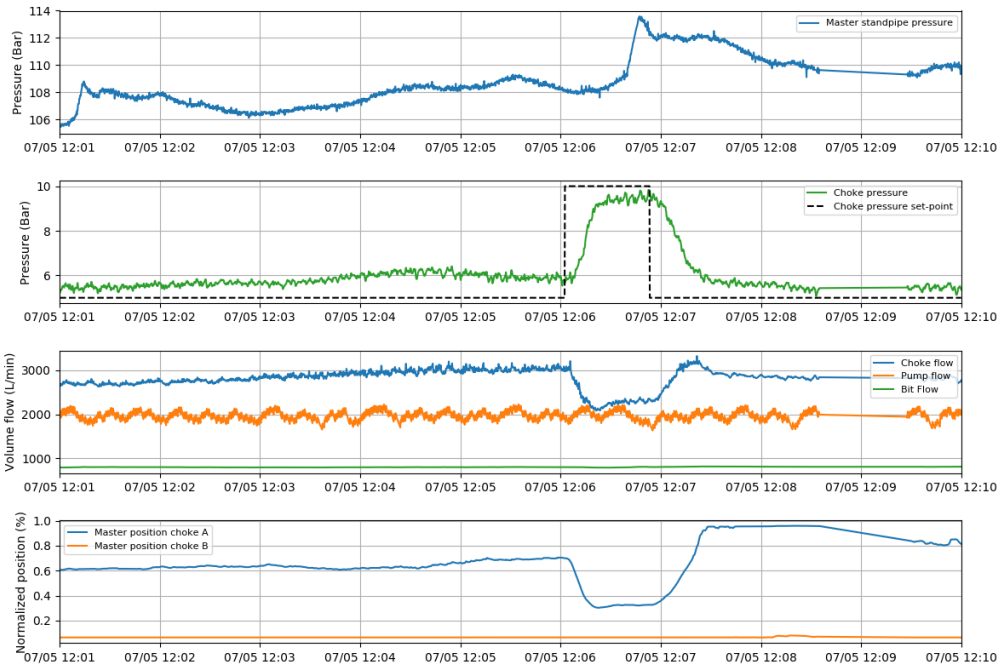

Figure 2.13: Setpoint step, under-balanced multiphase drilling. Controller based on simplified model with adaptive law on compressibility.

structure similar to that described in paper F but with the inner choke pressure loop having an adaptive law on β_a. In Fig. 2.14, a large gas bubble is circulated out over the chokes, with standpipe pressure mode used to maintain downhole pressure constant. The controller was able to keep stand pipe pressure (and thus downhole pressure) within +/− 1.5 bar with large variations in choke pressure. Although the operation in Fig. 2.14 is an under-balanced drilling operation, and not well control, it illustrates some of the possibilities with automatic standpipe pressure control in well control situations.

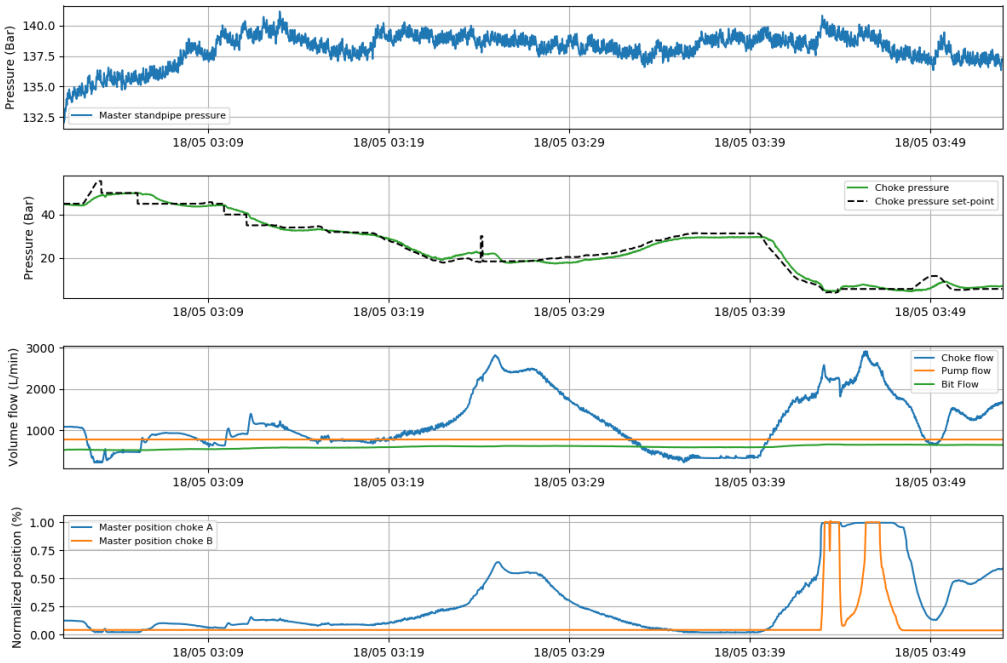

Figure 2.14: Automatic standpipe pressure control, underbalanced multiphase drilling. Controller based on simplified model with adaptive law on compressibility and cascade control of standpipe pressure, similar to the approach described in paper F.

2.4 Well control decision making; the Influx Management Envelope

There are numerous works in recent years on design of controllers for automated well control, such as by Aarsnes, Açıkmeşe *et al.* [69], Zhou, Aamo *et al.* [3], Ambrus, Aarsnes *et al.* [45] and Hauge, Aamo *et al.* [20]. Although relevant in both conventional operations if automatic choke control is available, as well as for MPD, MPD will probably be the first use of such technology. What is usually not covered in these papers, is the fact that one can not traditionally perform what would be considered well control operations using MPD equipment. MPD operations are defined by the International Association of Drilling Contractors (IADC) as: *"an adaptive drilling process used to precisely control the annular pressure profile throughout the wellbore. The objectives are to ascertain the downhole pressure environment limits and to manage the annular hydraulic pressure profile accordingly. It is the intention of MPD to avoid continuous influx of formation fluid to the surface. Any influx incidental to the operation will be safely contained using an appropriate process."*

This definition leaves much room for interpretation of what could be considered "an appropriate process" when dealing with influxes when performing MPD. The Well Control Matrix (WCM), as shown in the introduction in section 1.5 was introduced

by the Bureau of Safety and Environmental Enforcement (BSEE) to help deal with this decision making.

Mir Rajabi, Hannegan *et al.* [70], show that the WCM might not be optimal, and that for a maximum accepted surface pressure, there exists a combination of post influx surface pressures and kick volumes that will reach this limit, describing this as a "Kick envelope". An example of this kick envelope, generated by the use of a high fidelity simulator is shown in Fig. 2.15.

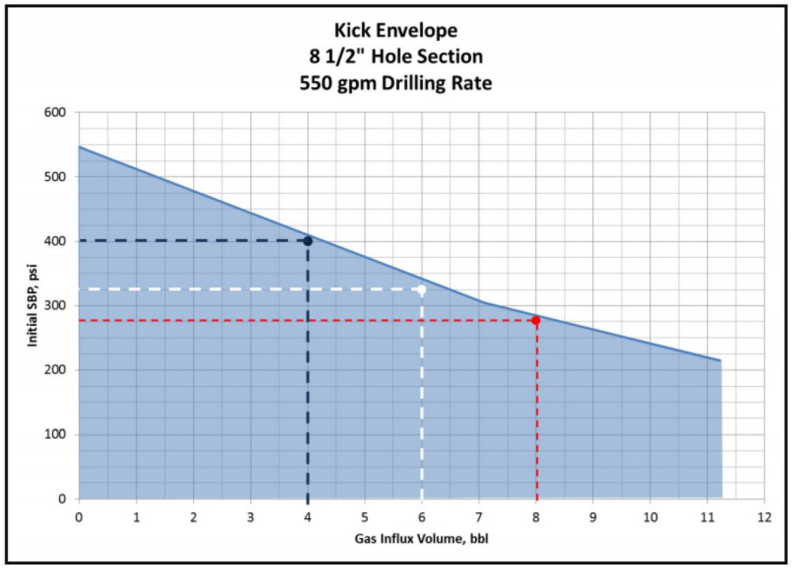

Figure 2.15: Kick Envelope, Mir Rajabi, Hannegan *et al.* [70].

Culen, Brand *et al.* [26] simplified the concept of the Kick Envelope from Mir Rajabi, Hannegan *et al.* [70], using more conventional single bubble kick tolerance calculations and showed that the kick envelope resembles the WCM if the x and y axes are swapped and coining the name "Influx Management Envelope" (IME). An example of the IME as described by Culen, Brand *et al.* [26] can be seen in Fig. 2.16.

In the years since the paper by Culen, Brand *et al.* [26] there has been a large growth in conference papers regarding the IME. Here the development of IMEs using various methods is described, usually through high fidelity simulations treated as a black box. It is found that when generating IMEs using high fidelity simulations, the generated IME tend to favour circulating over MPD (giving more tolerance) than in the equations by Culen. The IME has also been employed successfully for deep-water drilling operations, described by Gabaldon, Brand *et al.* [71]. Although the IME is apparently needed and wanted by industry, there are many misconceptions about what it actually is, and how it should/could be calculated. There has been no peer-reviewed journal papers systematically describing the IME.

Filling this gap between industry needs when it comes to well control decision making

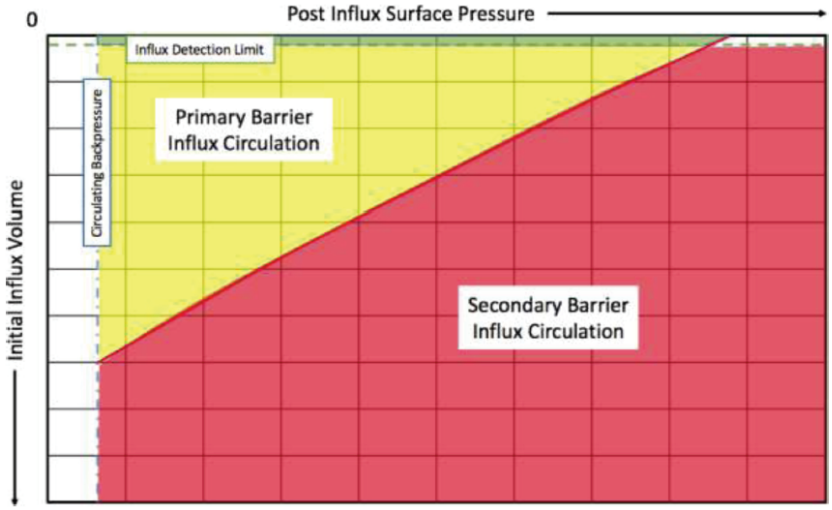

Figure 2.16: Influx Management Envelope (IME), Culen, Brand *et al.* [26].

in MPD operations and litterature is the aim of paper E. The history of well control decision making, from the WCM to the IME, is reviewed. The underlying core assumptions in the IME are detailed and the IME is derived from first principles. It is shown that calculating an IME without making some of the assumptions introduced by Culen, Brand *et al.* [26] can be done using numerical solutions to the equations, and the assumptions by Culen, Brand *et al.* [26] are systematically introduced to re-derive the original equation from the derived IME framework. It is found that if a real gas Equation of State is used, the calculated IME shows that a combination of higher influx volume/ initial surface pressure can be handled by MPD equipment than if the calculations are performed with ideal gas. It is also found that the IME equation presented by Culen, Brand *et al.* [26] might be less conservative than that of ideal gas, as it makes some assumptions on constant gas density with respect to downhole pressure. This is not very clear from [26], but shown in paper E. Examples of the IME calculated as described in paper E, with the presence of a formation weak point, and ideal gas-, Soave-Redlich-Kwong as well as Peng-Robinson EOS for two hypothetical test wells is shown in Figs. 2.17 and 2.18.

Sensitivity to different well parameters such as friction, depth and temperature is studied for the IME equations derived in paper E. It is for instance found that larger kick volumes can typically be tolerated as downhole temperature increases. This can be explained from thermodynamics considerations, but is contrary to the popular belief that "everything gets worse" with HPHT wells. In the IME considerably larger kick volumes can also be handled when drilling from a floating rig, as the riser will typically have a higher diameter then the casing in surface BOP operations.

The IME in paper E is then colour coded along the lines of that originally done by Culen, Brand *et al.* [26], and the different regions are classified by recommended

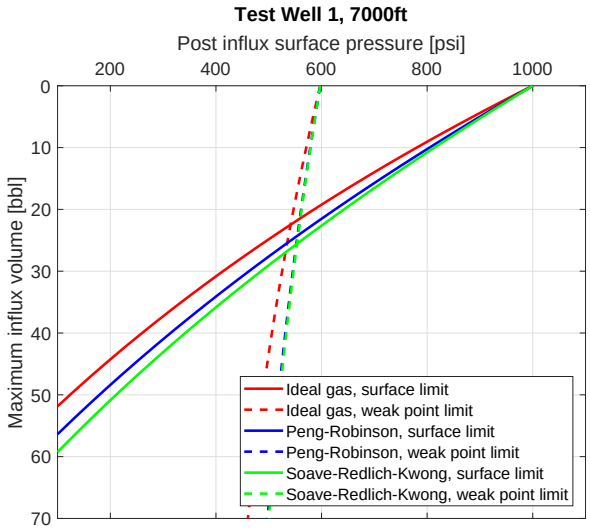

Figure 2.17: Influx management envelope, ideal and non-ideal gas with weak-point, 7000ft, 12.25 in section.

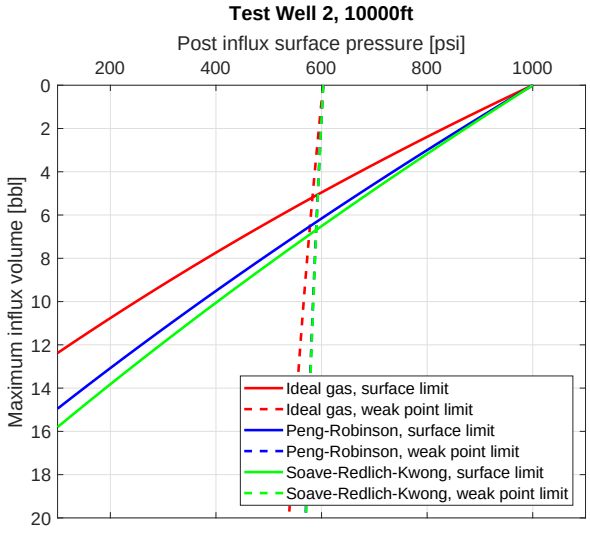

Figure 2.18: Influx management envelope, ideal and non-ideal gas with weak-point, 10000ft, 8.5 in section.

operation to deal with the influx. An example of the colour coded IME with classification of the different regions as described in paper E can be seen in Fig. 2.19.

The different regions in the IME in Fig. 2.19 can be described as follows:

I. Below influx detection limit, no influx is detected and operation continues as normal.

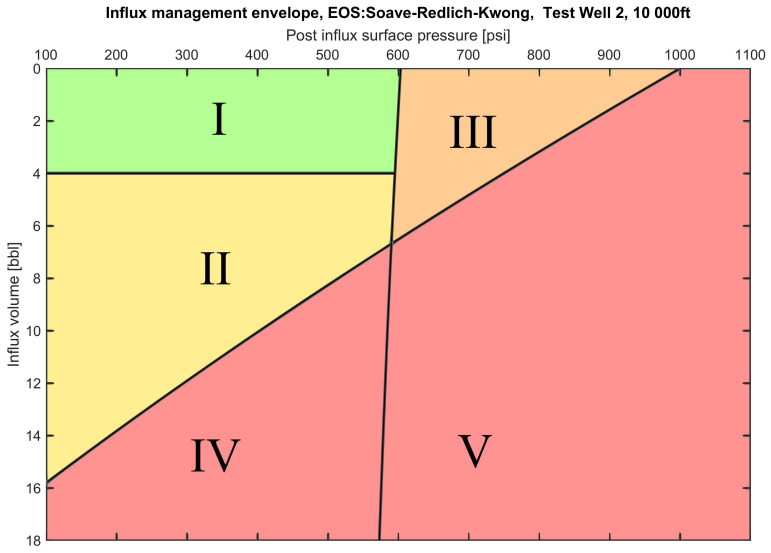

Figure 2.19: Influx management envelope with regions colour coded.

II. Influx detected and suppressed. Combinations of post-influx surface pressure and kick volume in this region will not exceed the specified surface-pressure limit when circulated to the surface and can be circulated out using the MPD equipment. The order of operations would be similar to that in the WCM, pick-up off-bottom (if required), maintain normal pump flow, and circulate out the influx using MPD and the primary MPD flow line. Combinations of post-influx pressure and kick volume that is exactly on the line separating this region and region **IV** will reach a peak surface pressure of 1000 psi (the specified limit) when circulated to the surface.

III. Influx/ post-influx pressure combinations in this region will exceed the specified weak-point pressure when circulated to the surface. The criticality of this depends on how the weak-point limit has been found, and the likelihood of an underground blowout if the limit is exceeded. If the weak-point limit is found from a Formation Integrity Test (FIT) then this limit might be exceeded without severe consequences. If the weak-point limit is from known formation fracture pressure, found from a Leak Off Test (LOT), lost circulation in offset wells, etc., the criticality of being in this region of the IME is higher. If the weak-point pressure limit represents minor losses, then these might also be cured using Lost Circulation Material (LCM). In the case that the weak-point limit represents major losses caused by fracturing and fracture propagation, well control might prove challenging.

IV. Combinations of post-influx pressure and kick volume in this region will exceed the specified maximum surface pressure (1000 psi) when circulated out, but the

kick will not violate the weak-point pressure limit. The kick can be circulated with the MPD equipment initially, but then handed over to conventional well control once the influx has reached a pre-determined depth.

V. Combinations of post-influx pressure and kick volume in this region will exceed both the MPD surface-pressure limit, and violate the weak-point pressure limit. The criticality of exceeding the weak-point limit depends on how the weak-point limit has been found, and the likelihood of an underground blowout if the limit is exceeded. A kick in this region might prove challenging, even when doing conventional well control. If this region is "large", such that even small kicks and low post-influx surface pressures are inside it, this shows a low kick tolerance for the well. In that case the only option might be to set a contingent casing, or finishing the well before planned Total Depth (TD).

3 Conclusion and further work

Reliable sensors for return flow measurement in conventional drilling is still a challenge for automatic kick/loss detection. For a lot of the developments in academia on model-based detection strategies, the accuracy of the return flow measurement has to be improved in the conventional drilling case. Paper A shows that sub-critical flume designs is promising. As subcritical flumes require an open channel flow, these might be a very interesting solution to the problem of return flow measurement in conventional drilling operations. Subsequent research after the publication of paper A confirm these findings and three PhD Theses have been defended on work branching out from the project of paper A. The proposed flow measurement principle has still not been shown in practical operation, but simulation and design is ongoing, with likely field trials by Kelda Drilling Controls within a year.

Through the last 5 years, work on a testing environment based initially on the isothermal Euler equations and later the DFM equations, has been done in parallel with Kelda controller designs based on Eqs. (1.9) to (1.13). The accuracy of the PDE model, especially in the context of wave propagation for single phase flows is studied in paper D. A discrepancy between the wave communication time in the PDE model and measured data is found. Considering fluid structure interactions improve the model fit, but is not sufficient to explain the discrepancy. It is also found that treating the bulk modulus as the only unknown parameter in the system can not make the PDE model fit both with respect to flow response and wave propagation. Further work on comparing the response of the PDE model in fast dynamics with field data should be performed.

The control system developed by Kelda has now been successfully utilized on more than 15 MPD wells. An important success factor in this is that the design used has been extensively tested on an independently developed PDE model for both single phase and multi phase operations. Operations have shown that a design based on the model by Kaasa, Stamnes *et al.* [1] is sufficient for single phase operations, shown in paper F and re-affirming the findings in Pavlov, Kaasa *et al.* [6]. When using the model in Eqs. (1.9) to (1.13), although fit for purpose in the case of controller design, the neglected wave dynamics of the PDE should be respected in terms of controller tuning and stability. This can be achieved through testing of designs based on Eqs. (1.9) to (1.13) with higher fidelity PDE models.

Multiphase modelling is by no means a straight-forward task, and even simplified multiphase models such as the DFM is a nonlinear hyperbolic system of PDEs. The DFM for drilling operations have source terms and in some cases non-negligible flow velocity compared to the speed of sound. Introducing source terms to the equations, although seemingly trivial, introduces challenges with respect to numerical solution of a system that is already challenging. In the context of certain model order reduction methods, semi discrete numerical schemes are beneficiary. Schemes that are relatively robust to largely varying local speed of sound, and well balanced in the presence of source terms have been derived in paper B and C.

For automatic control in multiphase conditions for MPD systems, it is shown that a controller based on the simplified model of Eqs. (1.9) to (1.13) retains reasonable performance, as longs as the system bulk modulus is treated as an unknown parameter. This result is discussed in the context of the recently published Reduced DFM (Red-DFM). In general, if mass transport and downhole pressure is not the main interest, but rather system pressure dynamics, these models are similar in the case where bulk modulus is treated as an unknown parameter. Estimator designs for tracking gas position and volume based on the Red-DFM should be performed in future work.

In paper G it is shown that a MPD system based on Eqs. (1.9) to (1.13) with an adaptive law on bulk modulus, can handle multiphase well conditions with robust automatic control of standpipe pressure. This operation was designed as an under-balanced drilling operation. Transferring this finding to well control in MPD operations is inhibited not only by industry inertia but also regulatory considerations. The Influx Management Envelope, show that the Well Control Matrix might be overly conservative in some cases and overly optimistic in others. Although the IME is gaining industry acceptance, formal definitions, discussions and derivations have been lacking in literature. This was the goal of paper E. Many recent approaches to the IME use commercially available multiphase simulators, and systematic study of the IME calculation described in paper E with the IMEs resulting from these simulators should be performed. Paper E assumes single bubble of gas, and does not have dissolution of gas into the liquid phase. This should be the topic of future work, ideally with comparison to high fidelity multiphase simulations.

Bibliography

[1] G.-O. Kaasa, Ø. N. Stamnes, O. M. Aamo and L. S. Imsland, 'Simplified hydraulics model used for intelligent estimation of downhole pressure for a managed-pressure-drilling control system', *SPE Drilling & Completion*, vol. 27, no. 01, pp. 127–138, 2012, ISSN: 1064-6671. DOI: 10.2118/143097-PA.

[2] J. Zhou, Ø. N. Stamnes, O. M. Aamo and G.-O. Kaasa, 'Observer-based control of a managed pressure drilling system', in *Control and Decision Conference, 2008. CCDC 2008. Chinese*, IEEE, 2008, pp. 3475–3480. [Online]. Available: http://ieeexplore.ieee.org/abstract/document/4597975/ (visited on 14/07/2017).

[3] J. Zhou, O. M. Aamo and G.-O. Kaasa, 'Switched control for pressure regulation and kick attenuation in a managed pressure drilling system', *Control Systems Technology, IEEE Transactions on*, vol. 19, no. 2, pp. 337–350, 2011, ISSN: 1063-6536.

[4] J. Å. Stakvik, C. Berg, G.-O. Kaasa, O. M. Aamo and U. Lehner, 'Adaptive Model Based Choke Control System for MPD Operations', in *SPE-179714-MS*, SPE: Society of Petroleum Engineers, 12th Apr. 2016, ISBN: 978-1-61399-446-7. DOI: 10.2118/179714-MS.

[5] J. Å. Stakvik, C. Berg, G.-O. Kaasa, R. Graham and A. Torrealba, 'Model-Based Control in Managed Pressure Drilling', presented at the SPE/IADC Drilling Conference and Exhibition, Society of Petroleum Engineers, 2017, ISBN: 1-61399-501-6.

[6] A. Pavlov, G.-O. Kaasa and L. Imsland, 'Experimental disturbance rejection on a full-scale drilling rig', *IFAC Proceedings Volumes*, vol. 43, no. 14, pp. 1338–1343, 2010, ISSN: 1474-6670.

[7] H. Holta, H. Anfinsen and O. M. Aamo, 'Improved Kick and Loss Detection and Attenuation in Managed Pressure Drilling by Utilizing Wired Drill Pipe', *IFAC-PapersOnLine*, vol. 51, no. 8, pp. 44–49, 2018, ISSN: 24058963. DOI: 10.1016/j.ifacol.2018.06.353. [Online]. Available: https://linkinghub.elsevier.com/retrieve/pii/S2405896318306839 (visited on 27/08/2019).

[8] H. Holta and O. M. Aamo, 'Boundary Set-Point Regulation of a Linear 2 × 2 Hyperbolic PDE with Uncertain Bilinear Boundary Condition', in *2018 IEEE Conference on Decision and Control (CDC)*, Miami Beach, FL: IEEE, Dec. 2018, pp. 2156–2163, ISBN: 978-1-5386-1395-5. DOI: 10.1109/CDC.2018.8619743. [Online]. Available: https://ieeexplore.ieee.org/document/8619743/ (visited on 27/08/2019).

[9] H. Anfinsen and O. M. Aamo, 'Adaptive Output-Feedback Stabilization of 2 x 2 Linear Hyperbolic PDEs with Actuator and Sensor Delay', in *2018 26th Mediterranean Conference on Control and Automation (MED)*, Zadar: IEEE, Jun. 2018, pp. 1–6, ISBN: 978-1-5386-7890-9. DOI: 10.1109/MED.2018.8442627. [Online]. Available: https://ieeexplore.ieee.org/document/8442627/ (visited on 06/03/2019).

[10] ——, 'Adaptive control of linear 2×2 hyperbolic systems', *Automatica*, vol. 87, pp. 69–82, 1st Jan. 2018, ISSN: 0005-1098. DOI: 10.1016/j.automatica.2017.09.020. [Online]. Available: http://www.sciencedirect.com/science/article/pii/S0005109817304909.

[11] F. Di Meglio, R. Vazquez and M. Krstic, 'Stabilization of a System of n+1 Coupled First-Order Hyperbolic Linear PDEs With a Single Boundary Input', *IEEE Transactions on Automatic Control*, vol. 58, no. 12, pp. 3097–3111, Dec. 2013, ISSN: 0018-9286, 1558-2523. DOI: 10.1109/TAC.2013.2274723. [Online]. Available: http://ieeexplore.ieee.org/document/6573344/ (visited on 27/08/2019).

[12] F. Di Meglio and U. J. F. Aarsnes, 'A distributed parameter systems view of control problems in drilling', *IFAC-PapersOnLine*, vol. 48, no. 6, pp. 272–278, 2015. [Online]. Available: http://www.sciencedirect.com/science/article/pii/S2405896315009106 (visited on 14/07/2017).

[13] J. Auriol and F. Di Meglio, 'Minimum time control of heterodirectional linear coupled hyperbolic PDEs', 15th Oct. 2015. arXiv: 1510.04424 [math]. [Online]. Available: http://arxiv.org/abs/1510.04424 (visited on 27/08/2019).

[14] J. Schubert, *Well Control Procedures for the Proper Identification and Handling of Kicks for the Prevention of Blowouts*. Texas A&M University, 1995.

[15] D. Fraser, R. Lindley, D. D. Moore and M. Vander Staak, 'Early Kick Detection Methods and Technologies', in *SPE Annual Technical Conference and Exhibition*, Amsterdam, The Netherlands: Society of Petroleum Engineers, 2014. DOI: 10.2118/170756-MS. [Online]. Available: http://www.onepetro.org/doi/10.2118/170756-MS (visited on 27/08/2019).

[16] E. Cayeux and B. Daireaux, 'Insights Into the Physical Phenomena That Influence Automatic Gain/Loss Detection During Drilling Operations', *SPE Drilling & Completion*, 2016, ISSN: 1064-6671. DOI: http://dx.doi.org/10.2118/166801-PA.

[17] B. A. Tarr, D. W. Ladendorf, D. Sanchez and G. M. Milner, 'Next-Generation Kick Detection During Connections: Influx Detection at Pumps Stop (IDAPS) Software', *SPE-178821-PA*, vol. 31, no. 04, pp. 250–260, 1st Dec. 2016, ISSN: 1064-6671. DOI: 10.2118/178821-PA. [Online]. Available: https://doi.org/10.2118/178821-PA.

[18] I. Pirir, A. Jinasena and R. Sharma, 'A dynamic model for drain back to active mud pit combined with a well model during drilling', *Journal of Petroleum Science and Engineering*, vol. 167, pp. 803–818, 1st Aug. 2018, ISSN: 0920-4105. DOI: 10.1016/j.petrol.2018.04.057. [Online]. Available: http://www.sciencedirect.com/science/article/pii/S0920410518303632.

[19] J. Zhou, G. Nygaard, J.-M. Godhavn, Ø. Breyholtz and E. H. Vefring, 'Adaptive observer for kick detection and switched control for bottomhole pressure regulation and kick attenuation during managed pressure drilling', presented at the American Control Conference (ACC), 2010, IEEE, 2010, pp. 3765–3770, ISBN: 1-4244-7427-2.

[20] E. Hauge, O. M. Aamo and J.-M. Godhavn, 'Model-based estimation and control of in/out-flux during drilling', presented at the American Control Conference (ACC), 2012, Hauge2012mbe: IEEE, 2012, pp. 4909–4914, ISBN: 1-4577-1095-1.

[21] D. Schafer, G. Loeppke, D. Glowka, D. Scott and E. Wright, 'An Evaluation of Flowmeters for the Detection of Kicks and Lost Circulation During Drilling', in *SPE-23935-MS*, SPE: Society of Petroleum Engineers, 1st Jan. 1992, p. 10, ISBN: 978-1-55563-516-9. DOI: 10.2118/23935-MS. [Online]. Available: https://doi.org/10.2118/23935-MS.

[22] G. Loeppke, D. Schafer, D. Glowka, D. Scott, M. Wernig and E. Wright, 'Development and evaluation of a meter for measuring return line fluid flow rates during drilling', SAND-91-2607, 5036200, 1st Jun. 1992, SAND-91–2607, 5 036 200. DOI: 10.2172/5036200. [Online]. Available: http://www.osti.gov/servlets/purl/5036200-GnFq3F/native/ (visited on 06/08/2019).

[23] A. Jinasena, 'Models and Estimators for Flow of Topside Drilling Fluid', PhD Thesis, University of South-Eastern Norway.

[24] P. Welahettige, 'Transient drilling fluid flow in Venturi channels: Comparing 3D and 1D models to experimental data'.

[25] K. Chhantyal, 'Sensor Data Fusion based Modelling of Drilling Fluid Return Flow through Open Channels', PhD Thesis, University of South-Eastern Norway.

[26] M. S. Culen, P. R. Brand, W. Bacon and O. R. Gabaldon, 'Evolution of the MPD Operations Matrix: The Influx Management Envelope', in *SPE/IADC Managed Pressure Drilling and Underbalanced Operations Conference and Exhibition*, Galveston, Texas, USA: Society of Petroleum Engineers, 2016. DOI: 10.2118/179191-MS. [Online]. Available: http://www.onepetro.org/doi/10.2118/179191-MS (visited on 07/01/2019).

[27] Ø. N. Stamnes, 'Nonlinear Estimation with Applications to Drilling', PhD Thesis, Norwegian University of Science and Technology, 2011.

[28] E. Hauge, 'Automatic Kick Detection and Handling in Managed Pressure Drilling Systems', PhD Thesis, Norwegian University of Science and Technology, Apr. 2013.

[29] U. J. F. Aarsnes, 'Modeling of Two-Phase Flow for Estimation and Control of Drilling Operations', PhD Thesis, Norwegian University of Science and Technology, 4th Jan. 2016.

[30] A. Ambrus, 'Modeling and Control of Managed Pressure Drilling Operations', PhD Thesis, The Univeristy of Texas at Austin, 2017.

[31] Ø. N. Stamnes, J. Zhou, O. M. Aamo and G.-O. Kaasa, 'Adaptive observer design for nonlinear systems with parametric uncertainties in unmeasured state dynamics', presented at the Decision and Control, 2009 Held Jointly with the 2009 28th Chinese Control Conference. CDC/CCC 2009. Proceedings of the 48th IEEE Conference On, IEEE, 2009, pp. 4414–4419, ISBN: 1-4244-3871-3.

[32] Ø. N. Stamnes, O. M. Aamo and G.-O. Kaasa, 'Redesigned Adaptive Observers with Tunable Convergence Rate', *IFAC Proceedings Volumes*, vol. 43, no. 14, pp. 278–283, 2010, ISSN: 1474-6670.

[33] Ø. N. Stamnes, G.-O. Kaasa and O. M. Aamo, 'Adaptive estimation of downhole pressure for managed pressure drilling operations', presented at the 2011 IEEE International Symposium on Intelligent Control, IEEE, 2011, pp. 989–995, ISBN: 1-4577-1104-4.

[34] A. A. Osiptsov, K. F. Sin'kov and P. E. Spesivtsev, 'Justification of the drift-flux model for two-phase flow in a circular pipe', *Fluid Dynamics*, vol. 49, no. 5, pp. 614–626, Sep. 2014, ISSN: 0015-4628, 1573-8507. DOI: 10.1134/S0015462814050081. [Online]. Available: http://link.springer.com/10.1134/S0015462814050081 (visited on 06/09/2017).

[35] H. Shi, J. A. Holmes, L. J. Durlofsky, K. Aziz, L. Diaz, B. Alkaya and G. Oddie, 'Drift-Flux Modeling of Two-Phase Flow in Wellbores', *SPE Journal*, vol. 10, no. 01, pp. 24–33, 1st Mar. 2005, ISSN: 1086-055X. DOI: 10.2118/84228-PA. [Online]. Available: http://www.onepetro.org/doi/10.2118/84228-PA (visited on 10/01/2019).

[36] P. Spesivtsev, K. Sinkov and A. Osiptsov, 'Comparison of drift-flux and multi-fluid approaches to modeling of multiphase flow in oil and gas wells', *WIT Transactions on Engineering Sciences*, vol. 79, pp. 89–99, 2013, ISSN: 1845647343.

[37] N. Zuber and J. A. Findlay, 'Average Volumetric Concentration in Two-Phase Flow Systems', *Journal of Heat Transfer*, vol. 87, no. 4, pp. 453–468, 1st Nov. 1965, ISSN: 0022-1481. DOI: 10.1115/1.3689137. [Online]. Available: https://doi.org/10.1115/1.3689137 (visited on 27/08/2019).

[38] J. E. Udegbunam, K. K. Fjelde, S. Evje and G. Nygaard, 'On the Advection-Upstream-Splitting-Method Hybrid Scheme: A Simple Transient-Flow Model for Managed-Pressure-Drilling and Underbalanced-Drilling Applications', *SPE Drilling & Completion*, vol. 30, no. 02, pp. 98–109, 2015, ISSN: 1064-6671.

[39] R. M. L. Coelho, P. L. C. Lage and A. Silva Telles, 'A comparison of hyperbolic solvers II: Ausm-type and Hybrid Lax-Wendroff-Lax-Friedrichs methods for two-phase flows', *Brazilian Journal of Chemical Engineering*, vol. 27, no. 1, pp. 153–171, 2010. [Online]. Available: http://www.scielo.br/scielo.php?pid=S0104-66322010000100014&script=sci_arttext (visited on 25/09/2017).

[40] S. T. Munkejord, 'Analysis of the two-fluid model and the drift-flux model for numerical calculation of two-phase flow', PhD Thesis, Norwegian University of Science and Technology, 2006.

[41] S. Evje and K. Fjelde, 'Relaxation schemes for the calculation of two-phase flow in pipes', *Mathematical and computer modelling*, vol. 36, no. 4-5, pp. 535–567, 2002, ISSN: 0895-7177.

[42] S. Evje and T. Flåtten, 'Hybrid flux-splitting schemes for a common two-fluid model', *Journal of Computational Physics*, vol. 192, no. 1, pp. 175–210, 2003, ISSN: 0021-9991.

[43] ——, 'On the wave structure of two-phase flow models', *SIAM Journal on Applied Mathematics*, vol. 67, no. 2, pp. 487–511, 2007, ISSN: 0036-1399.

[44] S. T. Munkejord, S. Evje and T. Flåtten, 'A MUSTA scheme for a nonconservative two-fluid model', *SIAM Journal on Scientific Computing*, vol. 31, no. 4, pp. 2587–2622, 2009, ISSN: 1064-8275.

[45] A. Ambrus, U. J. F. Aarsnes, A. K. Vajargah, B. Akbari and E. van Oort, 'A Simplified Transient Multi-Phase Model for Automated Well Control Applications', Ambrus2015: International Petroleum Technology Conference, 6th Dec. 2015. DOI: 10.2523/IPTC-18481-MS. [Online]. Available: https://www.onepetro.org/conference-paper/IPTC-18481-MS.

[46] E. F. Toro, *Riemann Solvers and Numerical Methods for Fluid Dynamics: A Practical Introduction*. Springer Science & Business Media, 2013, ISBN: 3-662-03490-5.

[47] K. H. Bendiksen, D. Maines, R. Moe and S. Nuland, 'The Dynamic Two-Fluid Model OLGA: Theory and Application', *SPE-19451-PA*, vol. 6, no. 02, pp. 171–180, 1st May 1991, ISSN: 0885-9221. DOI: 10.2118/19451-PA. [Online]. Available: https://doi.org/10.2118/19451-PA.

[48] B. Van Leer, 'Towards the ultimate conservative difference scheme. V. A second-order sequel to Godunov's method', *Journal of computational Physics*, vol. 32, no. 1, pp. 101–136, 1979, ISSN: 0021-9991.

[49] X.-D. Liu, S. Osher and T. Chan, 'Weighted Essentially Non-oscillatory Schemes', *Journal of Computational Physics*, vol. 115, no. 1, pp. 200–212, 1st Nov. 1994, ISSN: 0021-9991. DOI: 10.1006/jcph.1994.1187. [Online]. Available: http://www.sciencedirect.com/science/article/pii/S0021999184711879.

[50] P. K. Sweby, 'High Resolution Schemes Using Flux Limiters for Hyperbolic Conservation Laws', *SIAM Journal on Numerical Analysis*, vol. 21, no. 5, pp. 995–1011, Oct. 1984, ISSN: 0036-1429, 1095-7170. DOI: 10.1137/0721062. [Online]. Available: http://epubs.siam.org/doi/10.1137/0721062 (visited on 27/02/2019).

[51] H. Nessyahu and E. Tadmor, 'Non-oscillatory central differencing for hyperbolic conservation laws', *Journal of Computational Physics*, vol. 87, no. 2, pp. 408–463, Apr. 1990, ISSN: 00219991. DOI: 10.1016/0021-9991(90)90260-8. [Online]. Available: https://linkinghub.elsevier.com/retrieve/pii/0021999190902608 (visited on 27/02/2019).

[52] A. Kurganov and E. Tadmor, 'New high-resolution central schemes for nonlinear conservation laws and convection–diffusion equations', *Journal of Computational Physics*, vol. 160, no. 1, pp. 241–282, 2000, ISSN: 0021-9991.

[53] A. Kurganov, S. Noelle and G. Petrova, 'Semidiscrete central-upwind schemes for hyperbolic conservation laws and Hamilton–Jacobi equations', *SIAM Journal on Scientific Computing*, vol. 23, no. 3, pp. 707–740, 2001, ISSN: 1064-8275.

[54] P. Welahettige, B. Lie and K. Vaagsaether, 'Flow regime changes at hydraulic jumps in an open Venturi channel for Newtonian fluid', *The Journal of Computational Multiphase Flows*, vol. 9, no. 4, pp. 169–179, Dec. 2017, ISSN: 1757-482X, 1757-4838. DOI: 10.1177/1757482X17722890. [Online]. Available: http://journals.sagepub.com/doi/10.1177/1757482X17722890 (visited on 27/08/2019).

[55] ——, 'Computational fluid dynamics study of flow depth in an open Venturi channel for Newtonian fluid', presented at the The 58th Conference on Simulation and Modelling (SIMS 58) Reykjavik, Iceland, September 25th – 27th, 2017, 27th Sep. 2017, pp. 29–34. DOI: 10.3384/ecp1713829. [Online]. Available: http://www.ep.liu.se/ecp/article.asp?issue=138%26article=3 (visited on 28/08/2019).

[56] P. Welahettige, C. Berg, J. Lundberg, B. Lie and K. Vaagsaether, 'Computational Fluid Dynamics Study of the Effects of Drill Cuttings on the Open Channel Flow', *International Journal of Chemical Engineering*, vol. 2019, pp. 1–9, 22nd Aug. 2019, ISSN: 1687-806X, 1687-8078. DOI: 10.1155/2019/6309261. [Online]. Available: https://www.hindawi.com/journals/ijce/2019/6309261/ (visited on 26/08/2019).

[57] P. Welahettige, K. Vaagsaether and B. Lie, 'A solution method for one-dimensional shallow water equations using flux limiter centered scheme for open Venturi channels', *The Journal of Computational Multiphase Flows*, vol. 10, no. 4, pp. 228–238, Dec. 2018, ISSN: 1757-482X, 1757-4838. DOI: 10.1177/1757482X18791895. [Online]. Available: http://journals.sagepub.com/doi/10.1177/1757482X18791895 (visited on 28/08/2019).

[58] C. Agu, B. Lie and G. Elseth, 'Simulation of Transcritical Flow in Hydraulic Structures', presented at the The 56th Conference on Simulation and Modelling (SIMS 56), October, 7-9, 2015, Linköping University, Sweden, 25th Nov. 2015, pp. 369–375. DOI: 10.3384/ecp15119369. [Online]. Available: http://www.ep.liu.se/ecp/article.asp?issue=119%26article=37 (visited on 31/10/2019).

[59] C. E. Agu, Å. Hjulstad, G. Elseth and B. Lie, 'Algorithm with improved accuracy for real-time measurement of flow rate in open channel systems', *Flow Measurement and Instrumentation*, vol. 57, pp. 20–27, Oct. 2017, ISSN: 09555986. DOI: 10.1016/j.flowmeasinst.2017.08.008. [Online]. Available: https://linkinghub.elsevier.com/retrieve/pii/S0955598617301826 (visited on 31/10/2019).

[60] A. Kurganov and G. Petrova, 'A second-order well-balanced positivity preserving central-upwind scheme for the Saint-Venant system', *Communications in Mathematical Sciences*, vol. 5, no. 1, pp. 133–160, 2007, ISSN: 1539-6746.

[61] A. Jinasena, G.-O. Kaasa and R. Sharma, 'Use of Orthogonal Collocation Method for a Dynamic Model of the Flow in a Prismatic Open Channel: For Estimation Purposes', presented at the The 58th Conference on Simulation and Modelling (SIMS 58) Reykjavik, Iceland, September 25th – 27th, 2017, 27th Sep. 2017, pp. 90–96. DOI: 10.3384/ecp1713890. [Online]. Available: http://www.ep.liu.se/ecp/article.asp?issue=138%26article=12 (visited on 28/08/2019).

[62] J.-M. Godhavn, A. Pavlov and G.-O. Kaasa, 'New automatic control solutions for the drilling industry', *Transaction on Control and Dynamical Systems*, vol. 2, no. 2, pp. 61–69, 2013.

[63] U. J. F. Aarsnes, T. Flåtten and O. M. Aamo, 'Review of two-phase flow models for control and estimation', *Annual Reviews in Control*, 2016, ISSN: 1367-5788.

[64] U. J. F. Aarsnes, F. Di Meglio, S. Evje and O. M. Aamo, 'Control-oriented drift-flux modeling of single and two-phase flow for drilling', presented at the Proceedings of the ASME 2014 Dynamic Systems and Control Conference, San Antonio, USA, 2014.

[65] S. Clain and D. Rochette, 'First-and second-order finite volume methods for the one-dimensional nonconservative Euler system', *Journal of computational Physics*, vol. 228, no. 22, pp. 8214–8248, 2009, ISSN: 0021-9991.

[66] D. Kröner and M. D. Thanh, 'Numerical solutions to compressible flows in a nozzle with variable cross-section', *SIAM journal on numerical analysis*, vol. 43, no. 2, pp. 796–824, 2005, ISSN: 0036-1429.

[67] R. Käppeli and S. Mishra, 'Well-balanced schemes for the Euler equations with gravitation', *Journal of Computational Physics*, vol. 259, pp. 199–219, Feb. 2014, ISSN: 00219991. DOI: 10.1016/j.jcp.2013.11.028. [Online]. Available: http://linkinghub.elsevier.com/retrieve/pii/S0021999113007900 (visited on 07/09/2017).

[68] A. Chertock, S. Cui, A. Kurganov, S. NurOzcan and E. Tadmor, 'Well-balanced central-upwind schemes for the Euler equations with gravitation', *SIAM J. Sci. Comput*, 2016. [Online]. Available: http://www2.cscamm.umd.edu/publications/CCKOT%20well%20balanced%20gravitional%20Euler_CS-15-00.pdf (visited on 28/08/2017).

[69] U. J. F. Aarsnes, B. Açıkmeşe, A. Ambrus and O. M. Aamo, 'Robust controller design for automated kick handling in managed pressure drilling', *Journal of Process Control*, vol. 47, pp. 46–57, Nov. 2016, ISSN: 09591524. DOI: 10.1016/j.jprocont.2016.09.001. [Online]. Available: https://linkinghub.elsevier.com/retrieve/pii/S0959152416301159 (visited on 08/01/2019).

[70] M. Mir Rajabi, D. M. Hannegan and D. D. Moore, 'The MPD Well Control Matrix; What is Actually Happening', in *SPE Annual Technical Conference and Exhibition*, Amsterdam, The Netherlands: Society of Petroleum Engineers, 2014. DOI: 10.2118/170684-MS. [Online]. Available: http://www.onepetro.org/doi/10.2118/170684-MS (visited on 08/01/2019).

[71] O. R. Gabaldon, P. R. Brand, M. S. Culen, I. U. Haq, R. A. Gonzalez-Luis, T. P. D. Silva, G. Puerto and W. Bacon, 'Case Study: First Experience of Developing an Influx Management Envelope IME for a Deepwater MPD Operation', in *IADC/SPE Managed Pressure Drilling & Underbalanced Operations Conference & Exhibition*, Rio de Janeiro, Brazil: Society of Petroleum Engineers, 2017. DOI: 10.2118/185289-MS. [Online]. Available: http://www.onepetro.org/doi/10.2118/185289-MS (visited on 07/01/2019).

Part II

Scientific Publications

Paper A

Model-based drilling fluid flow rate estimation using Venturi flume

Berg, Christian, Anjana Malagalage, Cornelius E. Agu, Glenn-Ole Kaasa, Knut Vaagsaether, and Bernt Lie. "Model-Based Drilling Fluid Flow Rate Estimation Using Venturi Flume." IFAC-PapersOnLine 48, no. 6 (2015): 171–76. https://doi.org/10.1016/j.ifacol.2015.08.027.

Authors' role in the article: Ideas, modeling and writing.

Available online at www.sciencedirect.com

ScienceDirect

IFAC Papers Online
CONFERENCE PAPER ARCHIVE

IFAC-PapersOnLine 48-6 (2015) 171–176

Model-based drilling fluid flow rate estimation using Venturi flume

C. Berg * **A. Malagalage** ** **C. E. Agu** *** **G.-O. Kaasa** *
K. Vaagsaether *** **B. Lie** ***

* *Kelda Drilling Controls AS, Porsgrunn, Norway*
** *Tel-Tek, Porsgrunn, Norway*
*** *Telemark University College, Porsgrunn, Norway, (e-mail: Bernt.Lie@hit.no)*

Abstract: Monitoring the flow rate out of the well is critical for good control of the downhole pressure in drilling operations. In this feasibility study, we explore the possibility of using a Venturi flume to provide a cost-effective measurement of the flow rate, with improved accuracy compared to conventional methods. A Venturi flume has been simulated both using CFD and a simplified 1D model. By proper design of the Venturi flume, a jump in the fluid level in the throat section of the flume can be injected. Four methods of using this jump information are discussed, each with their own advantages and disadvantages, such as dependence on fluid properties, length of the flume, computation time, etc. Further work is necessary to improve sensor set-up and numeric methods, as well as testing out the concepts on a Venturi rig.

Keywords: Flow measurement, Models, Partial differential equations, Model approximation, Estimators

1. INTRODUCTION

1.1 Background

Control of the downhole pressure is critical in drilling operations. If the downhole pressure exceeds the strength of the formation, the wellbore might be fractured, causing a loss of drilling fluid to the formation and possibly damaging the reservoir. In the worst case, such a damage may cause an uncontrolled reduction in the downhole pressure. If, on the other hand, the downhole pressure reduces below the formation pore pressure, this may cause an unwanted influx of formation fluid into the wellbore and up the annulus, referred to as a kick, which in the worst case could escalate to a blow-out of hydrocarbons on the rig, e.g. the Deepwater Horizon incident, Hauge and Øien (2012). For safe operation, the downhole pressure should thus be kept within a window defined by the formation fracture pressure and the formation pore pressure.

Early detection of loss of drilling fluid to the formation or of a kick is the most effective measure that can be taken to eliminate or limit the consequences of such incidents. A prerequisite for detecting loss to the formation or kick during drilling operations is monitoring of the mass balance of the well, i.e. the flow of drilling fluid out of the well compared to that pumped into the well.

In conventional drilling, the flow rate out of the well is typically measured by a paddle in the open channel running to the mud pits on the rig. This is an inaccurate measurement that limits the resolution of kick/loss detection. A possible alternative is to use a Venturi flume: an open flume with a constriction, and designed to give a jump in the fluid level which holds information about the flow rate. Venturi flumes are typically used to measure large flows of water, and are rarely used in oil drilling. For drilling fluid flow, particle settling is not desired; Venturi flumes have no dead zone, and are thus suitable.

An important concept in fluid flow is that of critical flow. Consider throwing a pebble in a running fluid flow, with resulting ripples spreading in all directions at the wave velocity of the fluid. If the fluid velocity equals the wave velocity, the ripples spreading in the direction opposite to the flow are stagnant wrt. to a frame fixed to the ground; the flow is critical. If the fluid flow is larger than the wave velocity, the flow is supercritical, while if the fluid flow is smaller than the wave velocity, the flow is subcritical.

1.2 Previous work

The Venturi measurement principle is described in introductory books on fluid mechanics. The use of Venturi flume for measurement in hydrology is described e.g. in Gupta (2008). For use in oil rigs, it is necessary to consider variations in viscosity, the presence of rock chips, etc. Thus a more detailed study is called for.

A flume used for the transport and flow measurement should be designed for so-called supercritical flow conditions, Wilson (1991), Smith et al. (1981). A current flume design based on ISO 4359 standard is applied to so-called subcritical upstream conditions, ISO (2013). There has been some research on the requirements for supercritical flume design. A procedure for designing and using a supercritical flume where it is assumed that so-called critical flow conditions occur at the entrance of the channel throat is outlined in Smith et al. (1981). Little information is

10.1016/j.ifacol.2015.08.027

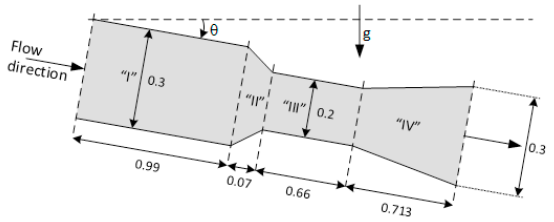

Fig. 1. Geometry of Venturi flume as seen from above: all measures are in [m]. Note that the section lengths are not to scale. Sections "I" and "III" have constant width. g is gravity and θ is the slope angle.

available on flow with non-Newtonian fluids such as used in drilling.

1.3 Structure of paper

In this work, we explore the possibility of using a Venturi flume to provide a cost-effective measurement of the flow rate out of the well, with improved accuracy compared to the flow paddle. In order to compare simulation results with those published in the literature, the experimental set-up of Smith et al. (1981) is used.

In Section 2, the experimental set-up is discussed. In Section 3, models for detailed 3D CFD analysis is discussed, as well as for a simplified 1D approximation. In Section 4, simulation results are presented, and the results are discussed. Some conclusions are drawn in Section 5.

The contributions of the paper are in comparing Venturi flume models using Computational Fluid Dynamics (CFD) for Newtonian fluids to published experimental results, then use CFD for non-Newtonian fluids, comparing CFD models with simplified 1D dynamic models and steady state models. The question is thus: can a Venturi flume be used to estimate relevant information for use in the drilling operation, and how complex a model is needed?

2. EXPERIMENTAL SET-UP

Consider a Venturi flume as seen from above in Fig. 1, with 5 sections numbered "I" through "V".

The slope angle θ of the flume bed can be changed.

With slope angle $\theta = 0$, this Venturi flume appears in the literature [1] as a test case for CFD solvers, using water as fluid and allowing a volumetric flow rate of $[2, 250]$ [m3/h]. In this paper, this nominal flume is used for comparing 3D simulation of water with the results from the literature, as well as with results from a simplified 1D simulation. Furthermore, we use the flume with slope angle $\theta = 4°$ and drilling fluid to study the flow with approximate 1D simulations, and discuss modifications of the flume to make it more suitable for flow measurements of drilling fluid.

3. MODELS OF VENTURI FLUME

3.1 CFD model

Navier Stokes equations For 3D simulations, CFD [2] relies on solving the Navier Stokes equations. These can be stated as (1) for conservation of mass and (2) for conservation of momentum for a Newtonian fluid, Versteeg and Malalasekera (2007)

$$\frac{\partial \rho}{\partial t} + \nabla \cdot (\rho v) = 0 \tag{1}$$

$$\frac{\partial}{\partial t}(\rho v_\varsigma) + \nabla \cdot (\rho v_\varsigma v) = -\frac{\partial p}{\partial \varsigma} + \nabla \cdot (\mu \nabla (v_\varsigma)) + s_\varsigma \tag{2}$$

In (2), ρ is density and $v \in \mathbb{R}^3$ is the velocity vector with components v_ς where $\varsigma \in \{x, y, z\}$. p is pressure and $s \in \mathbb{R}^3$ with components s_ς is additional momentum source terms such as gravity. Modelling non-Newtonian fluids require a different closure to the shear stresses. For incompressible flows (1) reduces to $\nabla \cdot (v) = 0$.

Shear stress For Newtonian fluids, stress τ is proportional to strain rate $\gamma_{\vartheta\varsigma} = \frac{\partial v_\vartheta}{\partial \varsigma}$, and the stress tensor is $\tau = \mu\gamma$ where viscosity μ is very sensitive to temperature. For the Newtonian base case simulations, the fluid is defined as water at 20° [C]. For the non-Newtonian simulations, the *Herschel-Bulkley* model is used, ANSYS-Inc (2011)

$$\tau = \tau_0 + K\gamma^{\frac{1}{\epsilon}} \tag{3}$$

where τ_0 is the excess shear stress, K is the flow behavior index, and $\frac{1}{\epsilon}$ is the fluid consistency index. Here τ_0, K and ϵ are rheological fitting parameters that can be determined by experiments.

Open channel description To track the interface in an open channel problem, the volume of fluid method (VOF) is commonly used, Hirt and Nichols (1981). In VOF an additional variable χ is introduced to represent the volume fraction of a phase in the discretized cell; $\chi = 1$ implies a cell completely filled with the fluid, $\chi = 0$ implies a cell void of the fluid, while $\chi \in (0, 1)$ implies that the cell contains the fluid surface. χ is given by (4),

$$\frac{\partial \chi}{\partial t} + v \cdot \nabla (\chi) = 0 \tag{4}$$

There are different ways to solve this equation; the normal finite volume schemes do not capture the discontinuous nature of χ at the interface. The High Resolution Interface Capture (HRIC) scheme, ANSYS-Inc (2011), is used in this work, and is an implicit finite volume method (FVM) designed to solve this type of interface equation while not being overly diffusive.

Turbulence and discretization Turbulence is in principle included in the above model, but requires infinitely fine discretization in time and space to be accurate. In practice, turbulence is instead introduced by doing time averaging of (2), by introducing "turbulent viscosity", and by introducing turbulent kinetic energy and its diffusion and relation to turbulent viscosity. In this work the common Reynolds Averaged Navier Stokes (RANS) $k - \epsilon$ model is used, Versteeg and Malalasekera (2007).

For discretization of (2) and the two extra turbulence quantities, both the first order upwind and second order upwind schemes are used. For pressure velocity coupling

[1] www.bamo.eu/international/_ftp/msa755-14.pdf
[2] CFD = Computational Fluid Dynamics

both the SIMPLE (Semi Implicit Method For Pressure Linked Equations), ANSYS-Inc (2011), and PISO (Pressure Implicit with Splitting of Operators), ANSYS-Inc (2011), are used.

Boundary and initial conditions The inlet boundary conditions are specified as a mass flow inlet (Section "I") with a specified free surface level and mass flows of liquid and gas (air) specified individually. The lightest phase (gas) is specified as the primary phase. The outlet conditions are specified as a pressure outlet, with the pressure profile set to "from neighboring cell" as the fluid is expected to have supercritical flow ((11), etc.) at the outlet. All walls are specified as no-slip walls, and the default $k-\epsilon$ ANSYS-Fluent wall function is used, ANSYS-Inc (2011). The top of the channel is specified as a pressure outlet with atmospheric pressure. To save computational time, the symmetry of the flume is exploited.

For initialization of the problem both patching the fluid volume with a flat liquid level and running the simulations starting with a "empty" channel is used.

Solver settings and meshing All simulations used the staggered grid, finite volume CFD solver ANSYS-Fluent. The simulations are run in transient using the first order implicit formulation until a steady state solution is obtained. Assessing convergence can be a challenge in CFD, and the residuals may not provide the full picture, Versteeg and Malalasekera (2007). Therefore in addition to monitoring the residuals, multiple surface monitors monitoring the weighted average velocity perpendicular to the flow direction are used to assess convergence. When the simulations are deemed to be in steady state, the solver is switched to steady state and all residuals are reduced to 10^{-4}.

For all 3D drawing and meshing the CFD pre-processor GAMBIT is used. A structured mesh is used, leading to a cell count for the mesh (half geometry) of ca. 3×10^5. Symmetry along the x axis is utilized.

3.2 Approximate 1D model

The Saint Venant Equations Under certain assumptions including uniform flow in cross sectional area A in the x-direction, the Navier Stokes equations can be simplified to the Saint Venant Equations (SVE), Aldrighetti (2007), (5)–(6)

$$\frac{\partial A}{\partial t} = -\frac{\partial \dot{V}}{\partial x} \tag{5}$$

$$\frac{\partial \dot{V}}{\partial t} = -\frac{\partial}{\partial x}\left(\frac{\dot{V}^2}{A}\right) - gA\frac{\partial h}{\partial x}\cos\theta + gA\sin\theta - \frac{F'_{\mathrm{f}}}{\rho} \tag{6}$$

where $\dot{V}$ is volumetric flow rate, g is gravity, h is fluid surface level, and F'_{f} is the friction force per unit length. Level h and cross sectional area A are related via the geometry of the flume. For these types of equations, a *friction slope* S_{f} is introduced, related to F'_{f} as

$$\frac{F'_{\mathrm{f}}}{\rho} \triangleq gAS_{\mathrm{f}}.$$

For filled pipes, the friction slope would be

$$S_{\mathrm{f}} = \frac{f}{2}\frac{\frac{\dot{V}}{A}\left|\frac{\dot{V}}{A}\right|\wp}{gA} \tag{7}$$

where $\wp$ is the wetting perimeter and f is Fanning's friction factor Bird et al. (2002). For shallow water in open flumes, the Gauckler–Manning–Strickler formula is often used, Chow (1959)

$$S_{\mathrm{f}} = k_{\mathrm{M}}^2\frac{\frac{\dot{V}}{A}\left|\frac{\dot{V}}{A}\right|\wp^{4/3}}{A^{4/3}}, \tag{8}$$

where k_{M} is Manning's friction coefficient.

In Jin and Fread (1997), an approximate friction slope for the Herschel-Bulkley model in (3) is given as

$$S_{\mathrm{f}} = \frac{\tau_0}{\rho g\frac{A}{\wp}}\left[1 + \left(\frac{(\epsilon+1)(\epsilon+2)\left|\frac{\dot{V}}{A}\right|}{(0.74+0.656\epsilon)\left(\frac{\tau_0}{K}\right)^{\epsilon}\frac{A}{\wp}}\right)\right]^{\frac{1}{\epsilon+0.15}}. \tag{9}$$

Wave velocities By linearizing the SVE around the steady solution (subscript s), the model can be decomposed into two advection equations of form Martinson and Barton (2002)

$$\frac{\partial \sigma_j}{\partial t} = -\lambda_j\frac{\partial \sigma_j}{\partial x} + \phi_j$$

where the wave velocities λ_j are given by

$$\lambda = \left(\sqrt{\frac{gA_{\mathrm{s}}\cos\theta}{\frac{\partial A}{\partial h}\big|_{\mathrm{s}}}}\cdot(N_{\mathrm{Fr}}+1),\ \sqrt{\frac{gA_{\mathrm{s}}\cos\theta}{\frac{\partial A}{\partial h}\big|_{\mathrm{s}}}}\cdot(N_{\mathrm{Fr}}-1)\right), \tag{10}$$

and the *Froude number* N_{Fr} is given as

$$N_{\mathrm{Fr}} \triangleq \frac{\frac{\dot{V}_{\mathrm{s}}}{A_{\mathrm{s}}}}{\sqrt{\frac{gA_{\mathrm{s}}\cos\theta}{\frac{\partial A}{\partial h}\big|_{\mathrm{s}}}}}. \tag{11}$$

For high velocity flow, $N_{\mathrm{Fr}} > 1$ (*supercritical* flow), both wave velocities are positive, and both boundary conditions (h, $\dot{V}$) must be given at $x = 0$. For low velocity flow, $N_{\mathrm{Fr}} < 1$ (*subcritical* flow), one wave velocity is positive, and the other is negative, and one boundary condition must be given at $x = 0$ while the other must be given at $x = L$.

Steady state analysis In this section, subindex "s" is introduced to indicate steady operation. In steady state, $\dot{V}_{\mathrm{s}}$ is constant, and the remaining equation can be rewritten as

$$\frac{dh_{\mathrm{s}}}{dx} = \frac{\frac{\dot{V}_{\mathrm{s}}^2}{gA_{\mathrm{s}}^3}\frac{\Delta W}{L_{\mathrm{r}}}h_{\mathrm{s}} + (\sin\theta - S_{\mathrm{fs}})}{\cos\theta\,(1-N_{\mathrm{Fr}}^2)} \tag{12}$$

where it has been assumed that area A forms an isosceles trapezoid with change of width ΔW over length L_{r} of the flume reach. Comparing with Fig. 1, $L_{\mathrm{r}} = 0.99$ for Section "I"; $\Delta W = 0.3-0.2 = 0.1$ for Section "II", etc. The *critical condition* occurs when $N_{\mathrm{Fr}} = 1$, which leads to the critical level $h_{\mathrm{s}}^{\mathrm{c}}$ given by

$$A^3\left(h_{\mathrm{s}}^{\mathrm{c}}\right) = \frac{\dot{V}_{\mathrm{s}}^2}{g\cos\theta}\left.\frac{\partial A}{\partial h}\right|_{\mathrm{s}}^{\mathrm{c}}. \tag{13}$$

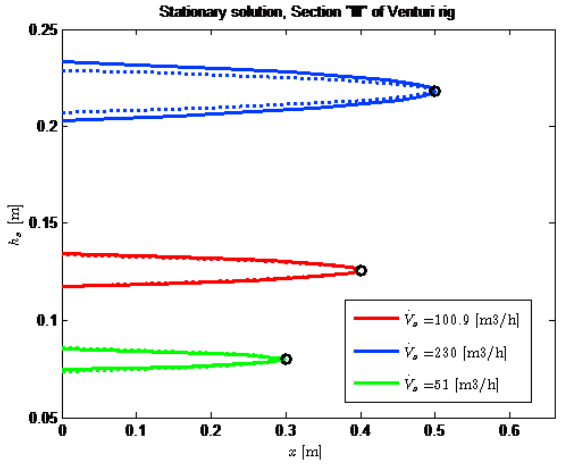

Fig. 2. Analytic solution $h_s(x)$ for Section "III" of Fig. 1 with specified critical point (x_c, h_s^c) (black circle), assuming Fanning friction with $f = 0.002$ (solid) and assuming Manning friction with $W \gg h_s$ (dotted).

At the critical condition (level h_s^c, at position x_c), the model in (12) breaks down.

With $\Delta W = 0$ and rectangular A with flume width W, the critical level from (13) becomes

$$h_s^c = \left(\frac{\dot{V}_s^2}{gW^2 \cos\theta} \right)^{\frac{1}{3}} \tag{14}$$

For this case of $\Delta W = 0$ and flume width W, supercritical flow implies $h_s < h_s^c$, while subcritical flow implies $h_s > h_s^c$.

The *uniform* level is found as $\frac{dh_s}{dx} = 0 \Longrightarrow S_{fs} = \sin\theta \geq 0$. With $\Delta W = 0$ and flume width W, the wetting perimeter is $\wp = W + 2h$. For Manning friction, the uniform level is thus found by solving the implicit equation

$$k_M^2 \frac{\frac{\dot{V}_s}{h_s^u W} \left| \frac{\dot{V}_s}{h_s^u W} \right| (W + 2h_s^u)^{4/3}}{(h_s^u W)^{4/3}} = \sin\theta; \tag{15}$$

we see that this expression breaks down when $\theta = 0$.

With $\Delta W = 0$, (12) is a separable differential equation, and analytic solutions can be found in some cases, giving implicit expressions for h_s in the form $x = \mathcal{F}(h_s)$. By computing a number of values x for h_s in a given range while requiring that the *solution goes through the critical point* denoted (x_c, h_s^c), typical solutions are as in Fig. 2.

A key point here is that the steady model in (12) with $\theta = 0$ does not admit a solution for $x > x_c$when the solution is required to go through the critical point. Obviously, the system does have a level when $x > x_c$; to find the complete solution when the solution passes through the critical point, it is necessary to keep the momentum balance in integral form in order to properly conserve the continuity of the momentum across the critical point,

$$h_{i+1} = h_i + \frac{1}{\cos\theta} \left(\frac{\dot{V}^2}{g(\bar{A}_{i+\frac{1}{2}} \cdot \bar{A}_{i-\frac{1}{2}})} - \frac{\dot{V}^2}{g\bar{A}_{i+\frac{1}{2}}^2} + \Delta x \left(\sin\theta - S_f\right)_{i+\frac{1}{2}} \right). \tag{16}$$

This implies that when going through the critical point, we can not use a "marching" method (e.g. Runge Kutta);

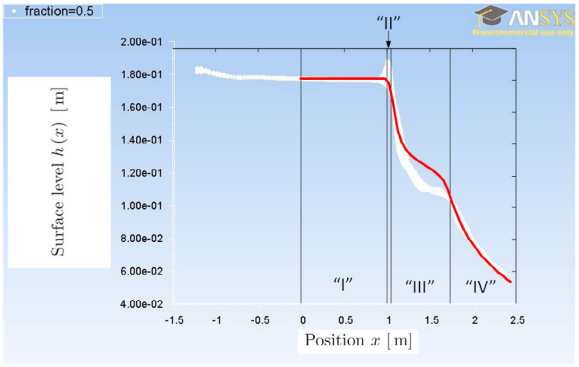

Fig. 3. Flow level profile in the Venturi flume with subcritical upstream flow condition; solution of SVE (solid red) overlaid over CFD solution. The location of Sections "I" – "IV" of the Venturi flume are indicated.

Table 1. Properties of Kaolin-based fluid Haldenwang (2003).

Properties	**Fluid**
Particle conc./vol. (%)	7.1
density, ρ [kg / m^3]	1118.5
yield stress, τ_0 [Pa]	10.551
fluid behavior index, K [Pa s^n]	0.834
fluid consistency index, $\frac{1}{\epsilon}$	0.387

instead the discretized model must use information from both downstream and upstream to the critical point. On the other hand, if the solution does not go through the critical point, the ODE formulation of (12) with a "marching" discretization algorithm can be used.

4. SIMULATION RESULTS

4.1 Case: water

We consider the case of $\theta = 0$, with water as fluid and flow rate 100.9 m^3 / h. CFD simulations are in excellent agreement with the flow rate-level tables specified by the flume manufacturer (maximum relative error of all simulations of 2%). Figure 3 shows the result of solving the SVE overlaid over the CFD solution in Malagalage et al. (2013).

In solving the SVE of the form (5) and (6), only the upstream boundary condition corresponding to the input flow rate of 100.9m^3 is specified. No downstream boundary is imposed since the flow is a free flow, and since it is revealed by CFD simulation that the flow passes through a critical point. The applied Manning roughness coefficient is 0.003. As can be seen, the result conforms to the CFD simulation result.

4.2 Case: drilling fluid

We change the Venturi flume slope to $\theta = 4°$, and consider a fluid characterized by the Herschel-Bulkley friction model with properties as given in Table 1.

Non-Newtonian fluid flow is often associated with high velocity to avoid fluid particle settling. This implies *supercritical* conditions and a corresponding level h_s which

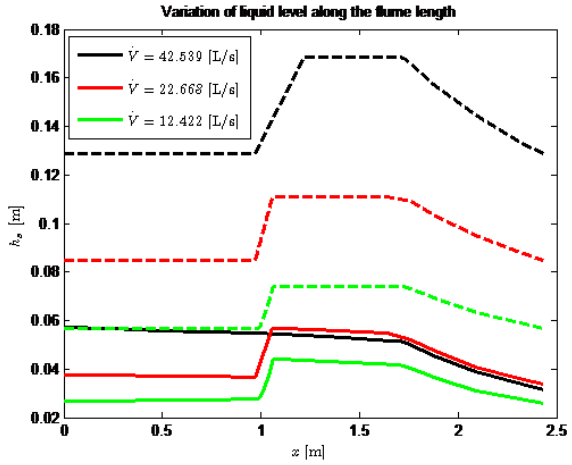

Fig. 4. Supercritical flow level profile (solid; above flume bed) in the Venturi flume with critical level (dashed); $W = 0.2\,\mathrm{m}$.

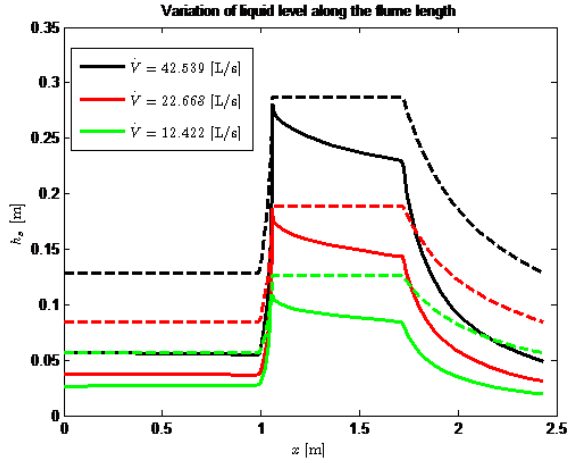

Fig. 5. Supercritical flow level profile (solid; above flume bed) in the Venturi flume with critical level (dashed); $W = 0.09\,\mathrm{m}$.

is lower than the critical level; the solution is then found by solving (12). Here, we have used steady flow rates of $\{12.422, 22.668, 42.539\}$ [L/s]. The boundary conditions for the level is thus given upstream, at the inlet to Section "I" of Fig. 1 according to Haldenwang (2003). Figure 4 shows the resulting steady solutions.

From Fig. 4, we see that the Venturi flume does not lead to an increase in the level up to the critical level despite the hydraulic jump in the throat section (Section "III"), and it is not possible to find the flow rate from this design.

Next, we consider redesigning the Venturi flume by reducing the width of Section "III" to $W = 0.09$ [m]. The result is shown in Fig. 5.

In Fig. 5, it is seen that a hydraulic jump occurs in the channel throat section (Section "III") towards its exit, and this jump approaches the critical level.

4.3 Discussion

The results in the two cases indicate that the 1D steady state Saint Venant equation can predict a flow in a Venturi flume. Solving the SVE gives information about the flow rate and level distribution in the flume.

In the water case where the level goes through the critical point, the flume is divided into 50 discrete cells. Using a dynamic SVE, steady state is reached within 30 [s] taking some 1.5 [s] of computation time. In the drilling fluid case where the level reaches critical level due to hydraulic jump, the simulation of the steady SVE is executed with the MATLAB ode23 solver, which uses 10768 discretization points and takes 5.5 [s] to solve on a fairly standard PC.

CFD with results as in the backdrop of Fig. 3 gives much more information than SVE. However, to find these results takes in the order of 5 [h] of computer time. This time can be reduced somewhat if the initial transient from empty flume can be eliminated, but the computation time will still be high.

It has been indicated that by measuring the highest level in the throat section and assume this is the critical level, we can compute the flow rate using (14). However, the exact location where the critical level is reached, varies with the flow rate. Furthermore, for measurements, it is desirable with a steady, noise-free level. An alternative is thus to instead measure the level at uniform conditions, $h_{\mathrm{s}}^{\mathrm{u}}$, and compute $\dot{V}_{\mathrm{s}}$ by equating $S_{\mathrm{fs}}\left(h_{\mathrm{s}}^{\mathrm{u}}, \dot{V}_{\mathrm{s}}\right) = \sin\theta$ similar to in (15), where we use the Herschel-Bulkley expression for friction slope. Thus

$$\dot{V}_{\mathrm{s}} = \frac{\left(W h_{\mathrm{s}}^{\mathrm{u}}\right)^2}{W + 2h_{\mathrm{s}}^{\mathrm{u}}} \left[\left(\frac{W h_{\mathrm{s}}^{\mathrm{u}}}{W + 2h_{\mathrm{s}}^{\mathrm{u}}} \frac{\rho g}{\tau_0} \sin\theta \right)^{\epsilon+0.15} - 1 \right] \times \frac{(0.74 + 0.656\epsilon)}{(\epsilon+1)(\epsilon+2)} \left(\frac{\tau_0}{K} \right)^{\epsilon}. \tag{17}$$

Whether we use the Herschel-Bulkley model or some other friction model, the velocity expression will depend on the viscosity of the fluid.

Often, due to the short length of the flume, the uniform level is not reached, and (17) does not apply. Based on Bernoulli's equation, ISO (2013) develops an implicit expression for $\dot{V}_{\mathrm{s}}$ as

$$\dot{V}_{\mathrm{s}} = \left(\frac{2}{3}\right)^{\frac{3}{2}} \sqrt{\frac{g}{\beta}} \left(1 - \frac{0.006L}{W}\right) \left(1 - \frac{0.003L}{h_{\mathrm{s}}}\right)^{\frac{3}{2}} \times \left(1 + \frac{\beta \left(\frac{\dot{V}_{\mathrm{s}}}{W}\right)^2}{2g h_{\mathrm{s}}^3} \right)^{\frac{3}{2}} W h_{\mathrm{s}}^{\frac{3}{2}} \tag{18}$$

where L and W relates to the length and width of the throat section, and β is a tuning factor to handle different viscosities. Level h_{s} is measured in the middle of the throat section.

Another alternatively is to use the fully dynamic SVE, and combine the model with multiple level measurements in a state estimation scheme.

5. CONCLUSIONS

In this paper, CFD simulations of water flow in a zero slope Venturi flume have given excellent agreement with experimental results in the literature. Next, a simplified 1D model based on the Saint Venant Equations (SVE) has been analyzed, and found to give good agreement with the CFD model; better agreement is expected with improved tuning of boundary conditions for the SVE model. The SVE model has been used to simulate the case of drilling fluid flow in the same Venturi flume, with a 4° slope of the flume. Because low flow rate may lead to particle settling for drilling fluid, a high flow rate study is carried out. The study indicates that little information about the flow rate can be found using the nominal width of the Venturi flume. However, by narrowing the throat section of the flume, a significant jump in the level is achieved, and this level jump holds information about the flow rate.

Four possible methods for deriving the flow rate from the level jump are discussed in Section Discussion: (i) measuring the maximal level gives the flow rate independently of the fluid properties, (14), but the accurate level is complicated to measure, (ii) measuring the uniform level, the flow rate can be found if the fluid properties are known, (17) — but depends on a sufficiently long flume to reach uniform conditions, (iii) measuring some mid-way level can be used to derive the flow rate (18), but this method also depends on the fluid properties, and (iv) combining the transient SVE model in (5), (6) with multiple level measurements via state estimation is possible, but also depends on the fluid properties.

Future work will involve testing the various methods on a Venturi rig. Challenges for this future work include sensor set-up, the numerics of solving the SVE model, and efficient estimation algorithms.

REFERENCES

Aldrighetti, E. (2007). *Computational hydraulic techniques for the Saint Venant Equations in arbitrarily shaped geometry*. Ph.D. thesis, Universit'a degli Studi di Trento, Dipartimento di Matematica.

ANSYS-Inc (2011). *Ansys FLUENT Users's Guide*, 14 edition.

Bird, R.B., Stewart, W.E., and Lightfoot, E.N. (2002). *Transport Phenomena*. John Wiley & Sons, New York, second edition.

Chow, V.T. (1959). *Open-Channel Hydraulics*. McGraw-Hill.

Gupta, R.S. (2008). *Hydrology and Hydraulic Systems*. Waveland Press, third edition edition.

Haldenwang, R. (2003). *Flow of Non-Newtonian Fluids in Open Channels*. Ph.D. thesis, Cape Technikon, Cape Town, South Africa.

Hauge, S. and Øien, K. (2012). Deepwater horizon: Lessons learned for the norwegian petroleum industry with focus on technical aspects. *Chemical Engineering transactions*, 26, 621–626.

Hirt, C. and Nichols, B. (1981). Volume of fluid (vof) method for the dynamics of free boundaries. *Journal of Computational Physics*, 39(1), 201 – 225. doi: http://dx.doi.org/10.1016/0021-9991(81)90145-5.

ISO (2013). Flow measurement structures-rectangular, trapezoidal and u-shaped flumes. Technical Report ISO 4359, International Organization for Standardization, Switzerland.

Jin, M. and Fread, D. (1997). One-dimensional routing of mud/debris flows using nws fldwav model. In C. lung Chen (ed.), *Debris-Flow Hazards Mitigation: Mechanics, Prediction, and Assessment*, 687–696. ASCE, New York.

Malagalage, A., Berg, C., Agu, C., Chhantyal, K., and Mohammadi, F. (2013). Simulation of open channel flow for mass flow measurement. Msc project, Telemark University College.

Martinson, W.S. and Barton, P.I. (2002). Index and Characteristic Analysis of Linear PDAE Systems. *SIAM Journal on Scientific Computing*, 24(3), 905–923.

Smith, R., Chery, D., Jr., K.R., and Gwinn, W. (1981). Supercritical flow flumes for measuring sediment-laden flow. Technical Report Bulletin No. 1655, U.S. Department of Agriculture.

Versteeg, H.K. and Malalasekera, W. (2007). *An introduction to computational fluid dynamics : the finite volume method*. Pearson Education Ltd. cop., Harlow, England, New York.

Wilson, K. (1991). Flume design for homogeneous slurry flow. *Particulate Science and Technology*, 9, 149–159.

Paper B

A Godunov-Type Scheme for the Drift Flux Model with Variable Cross Section

Abbasi, Mohammad H., Sajad Naderi Lordejani, Naveen Velmurugan, Christian Berg, Laura Iapichino, Will H.A. Schilders, and Nathan van de Wouw. "A Godunov-Type Scheme for the Drift Flux Model with Variable Cross Section." Journal of Petroleum Science and Engineering 179 (August 1, 2019): 796–813. https://doi.org/10.1016/j.petrol.2019.04.089.

Authors' role in the article: Literature review, ideas, implementation and critical review.

Journal of Petroleum Science and Engineering 179 (2019) 796–813

Contents lists available at ScienceDirect

Journal of Petroleum Science and Engineering

journal homepage: www.elsevier.com/locate/petrol

A Godunov-type Scheme for the Drift Flux Model with Variable Cross Section

M.H. Abbasi[a,*], S. Naderi Lordejani[b], N. Velmurugan[c], C. Berg[d,e], L. Iapichino[a], W.H.A. Schilders[a], N. van de Wouw[b,f]

[a] Department of Mathematics and Computer Science, Eindhoven University of Technology, the Netherlands
[b] Department of Mechanical Engineering, Eindhoven University of Technology, the Netherlands
[c] Centre Automatique et Systèmes, MINES ParisTech, France
[d] Kelda Drilling Controls, Norway
[e] Department of Electrical Engineering, IT and Cybernetics, University of South-Eastern Norway, Norway
[f] Department of Civil, Environmental and Geo-Engineering, University of Minnesota, USA

ARTICLE INFO

Keywords:
Drift Flux Model
Finite-volume scheme
Variable cross section
Well-balanced scheme
Two-phase flow
Non-conservative PDE

ABSTRACT

This paper presents a modification of a classical Godunov-type scheme for the numerical simulation of a two-phase flow in a pipe with a piecewise constant cross-sectional area. This type of flow can occur in wellbores during drilling for oil and gas as well as after well completion. Contrary to classical finite-volume schemes, the numerical scheme proposed in this paper captures the steady-state solution of the system without generating non-physical discontinuities in the numerical solution close to the locations of discontinuities in the cross-section. Moreover, the proposed scheme can be extended to problems with piecewise continuous cross-sectional area. This extension is achieved by discretization of the area along the spatial domain and converting the piecewise continuous area into a piecewise constant area. The proposed scheme reduces to the classical scheme when the cross-sectional area is constant along the spatial domain. For the purpose of computational efficiency, the modification to the classical scheme is only applied at the locations of area variation and the numerical solver reduces to the classical scheme where the cross-sectional area is constant. It is also shown that the proposed scheme can be effectively used to simulate two-phase flows arising from the perturbation of the steady-state solution. The effectiveness of the proposed scheme is shown through illustrative numerical simulations. Finally, it should be noted that the proposed scheme retains the same order of accuracy as the underlying classical scheme.

1. Introduction

Reliable models and accurate numerical solutions for single- and two-phase flows are necessary for many industrial applications, such as drilling for oil and gas and flow in fuel bundles and pipelines [1, 2, 3]. Modeling of the transient behavior of the flow dynamics in these industrial systems plays a crucial role in the design, decision making and control of such systems. For the simulation of two-phase flows, the one-dimensional Drift Flux Model (DFM), which is constituted by a set of first-order nonlinear hyperbolic partial differential equations, has gained attention [4, 5] due to its balance between predictive capabilities and simplicity. Compared to the two-fluid model, the DFM is favorable from a numerical simulation perspective [6]. In addition, the DFM remains hyperbolic over a wider region of the variables and it is also more accurate than the two-fluid model in homogeneous two-phase regimes [6].

In many industrial applications, the computational domain, typically a pipe, frequently has a variable cross-sectional area along its length. In particular, a drilling well experiences discontinuities in the cross-sectional area [7] as schematically illustrated in Figure 1. These area discontinuities affect the resonance frequency of the wave propagation effects inside the system, especially the rapid pressure dynamics. If this phenomenon is not considered, the model may lose its predictive capacity. Moreover, in the scope of controller design for Managed Pressure Drilling (MPD), the system performance may seriously deteriorate when such effects are not appropriately represented in the model. Hence, a model that accounts for such phenomena is required.

Two-phase flow in a pipe with variable cross-sectional area increases the complexity of the governing model and, subsequently, its numerical solution as a non-conservative term is added to the governing equations [8]. This means that after adding this term, all derivatives

* Corresponding author.
E-mail address: m.h.abbasi@tue.nl (M.H. Abbasi).

https://doi.org/10.1016/j.petrol.2019.04.089
Received 6 February 2019; Received in revised form 12 April 2019; Accepted 24 April 2019
Available online 06 May 2019
0920-4105/

over the spatial variable cannot be gathered into a single differential term.

Classical finite-volume schemes are suitable for numerical simulation of conservative hyperbolic PDEs, such as the DFM with a constant cross-sectional area [4, 9, 10]. However, these classical methods cannot be effectively used to solve non-conservative PDE models, such as the DFM with variable cross-sectional area [11]. A common approach to incorporate the area variation is to treat the non-conservative term as a source term [12]. This treatment leads to non-physical and numerical spikes in the numerical solution and, subsequently, this approach cannot be reliably used [11].

Addressing the issue of the presence of non-conservative terms in mathematical models of various systems in the scope of numerical implementation is an active research area. Different methods have been developed for the simulation of the behavior of a single-phase flow in a pipe with a variable cross-sectional area. Instead of treating the non-conservative term as an additional source term, a modification to the Rusanov scheme [13] has been proposed in [14] to capture the steady-state solution of the Euler equations. However, this method is not well-balanced in the presence of non-zero flow in the system, i.e., the numerical solution does not preserve the steady-state solution for non-zero flow scenarios. A model-based modification of the input arguments of the finite-volume scheme has also been introduced in [8, 11, 15]. All the mentioned works deal with the variable cross-sectional area in single-phase flow systems while two-phase flows frequently occur in many realistic industrial applications [1, 2, 3, 16].

To the best of the authors' knowledge, the effect of non-conservative terms in two-phase flow models has been studied only to a rather limited extent for conservative shock capturing schemes. As an example, in [17], the non-conservativeness in the two-fluid model originating from the state variables is considered. However, the non-conservativeness originating from the variable cross-sectional area is not discussed. Therefore, this paper focuses on developing a reliable numerical approach for the DFM capturing the effects of variations in the cross-sectional area by introducing a model-based scheme, inspired by [11].

The results of this paper can be used to simulate the flow of gas and liquid mixtures in pipelines. In particular, this kind of flow is common in the upstream, midstream and downstream sector of the oil and gas industry. As in the upstream sector, for any drilling well, the understanding of the flow (and pressure) dynamics in the drill-string and annulus is essential. Herein, the drill-string consists of a series of drill pipes and the bottom hole assembly (assembly of heavy weight drill pipes and mud motors). Together these system components represent a drastically varying flow path, both inside the drill-string and the annulus (refer to Figure 1). In drilling operations for oil and gas, multi-phase fluid flow arises in several cases, such as gas influx into the annulus or during under-balanced drilling where the gas is also present in the drill-string in addition to the annulus. Moreover, the proposed method can be used to validate hydraulics models in a drilling well with the DFM, as an extension to [16]. In many studies for the DFM validation in a drilling well, such as e.g. the one in [16], the effect of area discontinuity has been ignored. However, dealing with the field data, the effects of these discontinuities should be taken into account and the developments in this paper support this. The work of this paper can then be used to support the operational design of MPD-based operations and controller design for MPD. In the midstream operations, multi-zone completion designs, using a liner or an open-hole in combination with tubings, pose a multi-phase flow scenario in a pipe with potentially variable cross-sectional area during the production phase. In the downstream sector, the refining and separation of the natural gas and crude oil can be simulated using the results of this paper.

Contributions of this paper are provided in two areas. First, this paper reviews the current techniques to deal with non-conservative terms within single-phase flow. These techniques, which are not applicable for the DFM, are adapted for the DFM. Secondly, new

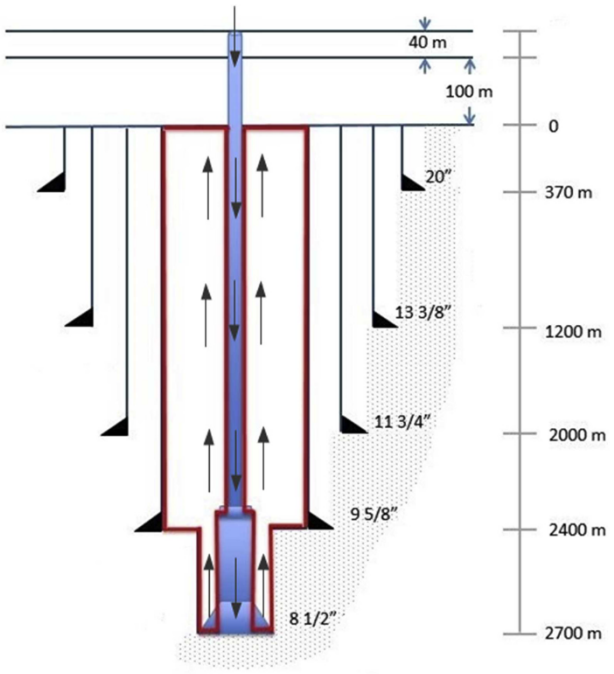

Figure 1. The discontinuous cross-section of area in a real drilling well with diameters shown in inch and depths shown in meter (as common in the drilling community). The path of the fluid is marked by black arrows. The data is extracted from [7].

approaches within the context of the DFM are introduced to deal with the non-conservative term induced by the variable cross-sectional area. Since the goal of this paper is to evaluate the merit of the scheme in capturing the effects of area variation, the effect of source terms such as friction and gravity has not been considered. The evaluation of the scheme in the absence of the source term is a common practice in the finite-volume community [18, 19, 11]. In addition, considering source terms raises the issue of the well-balancedness [20], which is beyond the scope of this paper. Incorporating these additional source terms is the subject of future works.

The structure of this paper is as follows. In Section 2, an overview of the model is given together with a comparison between the conservative and non-conservative DFM and the corresponding eigenvalue analysis is performed. Various methodologies to deal with the non-conservative term are proposed in Section 3. In Section 4, the effectiveness of the different variable cross-section treatments in preserving the steady-state solution is evaluated through numerical tests and, subsequently, transient simulations are performed. Finally, conclusions and recommendations for future works are presented in Section 5.

2. Two-Phase Flow Model

In this section, the DFM in case of constant and variable cross-sectional area is presented. Eigenvalue analysis is performed for the non-conservative system with variable cross-sectional area. Since the dynamics originating from the perturbation to the steady states are of numerical interest in this study, the steady-state solution is also presented in this section. Next, the necessary boundary conditions for both the transient and the steady-state model are defined.

2.1. Introduction to the Drift Flux Model

The Drift Flux Model is widely used to describe the behavior of two-phase flow systems [5, 21, 22, 23]. It consists of two mass balance equations, one for each phase, and one combined momentum balance equation for the mixture of the phases. The governing equations for

one-dimensional systems are given by

$$\frac{\partial(\alpha_l\rho_l)}{\partial t} + \frac{\partial(\alpha_l\rho_l u_l)}{\partial x} = 0, \tag{1a}$$

$$\frac{\partial(\alpha_g\rho_g)}{\partial t} + \frac{\partial(\alpha_g\rho_g u_g)}{\partial x} = 0, \tag{1b}$$

$$\frac{\partial(\alpha_l\rho_l u_l + \alpha_g\rho_g u_g)}{\partial t} + \frac{\partial(\alpha_l\rho_l u_l^2 + \alpha_g\rho_g u_g^2 + p)}{\partial x} = 0, \tag{1c}$$

where $\alpha(t, x)$, $\rho(t, x)$, $u(t, x)$ and $p(t, x)$ are, respectively, the volume fraction, density, velocity and pressure, which are functions of time t and the one-dimensional spatial coordinate x. The subscripts l and g denote the liquid and gas, respectively. Noteworthy, the DFM is based on the assumption of mechanical equilibrium between the two phases, i.e., the pressure of the gas and the pressure of the liquid are equal. The DFM as in (1) contains seven variables while it is expressed in only three equations. Thus, four other equations, called closure relationships, are required to, potentially, uniquely solve the system of equations. The most widely used closure relationships are listed below [24, 5]:

$$\alpha_l + \alpha_g - 1 = 0, \tag{2}$$

$$u_g - (Ku_{mix} + S) = 0, \tag{3}$$

$$p - \rho_g c_g^2 = 0, \tag{4}$$

$$p - ((\rho_l - \rho_0)c_l^2 + p_0) = 0. \tag{5}$$

Equation (2) implies that every section of the pipe is filled up with a mixture of the liquid and gas. The slip law (3), showing a static relation between the velocity of the gas and the liquid, compensates for the fact that only one momentum balance is included in the DFM. Here, K and S are, respectively, the distribution coefficient and the drift velocity of the gas relative to the liquid defined according to the flow regime [25, 26] and $u_{mix} = \alpha_l u_l + \alpha_g u_g$ is the velocity of the mixture. Equations (4) and (5) represent the equation of state (EOS) for the gas and liquid phases, respectively. c_l and c_g are the speeds of sound in the liquid and gas phases, which can be assumed to be constants or be functions of other variables, such as pressure. Finally, ρ_0 and p_0 are, respectively, the reference values for density and pressure around which the EOS for the liquid has been linearized.

Model (1) is based on the assumption that the cross-section is constant all along the spatial domain. When this does not hold, the DFM in (1) should be modified in order to take into account the cross-sectional variations. By including a variable cross-sectional area along the computational domain, $A = A(x)$, as used in [27], the system (1) changes to

$$\frac{\partial(\alpha_l\rho_l A)}{\partial t} + \frac{\partial(\alpha_l\rho_l u_l A)}{\partial x} = 0, \tag{6a}$$

$$\frac{\partial(\alpha_g\rho_g A)}{\partial t} + \frac{\partial(\alpha_g\rho_g u_g A)}{\partial x} = 0, \tag{6b}$$

$$\frac{\partial((\alpha_l\rho_l u_l + \alpha_g\rho_g u_g)A)}{\partial t} + \frac{\partial((\alpha_l\rho_l u_l^2 + \alpha_g\rho_g u_g^2 + p)A)}{\partial x} = p\frac{\partial A}{\partial x}, \tag{6c}$$

$$\frac{\partial A}{\partial t} = 0. \tag{6d}$$

Equation (6d) is trivial and it is only added to enable the eigenvalue analysis presented later. Notably, system (1) can be written in the conservative form while system (6) cannot be written in such a form due to the presence of the term $p\partial A/\partial x$ (in (6c), all terms concerning spatial derivatives of the state variables cannot be gathered in one single term and therefore the system (6) is non-conservative). Therefore, the area variation included in (6) significantly affects the solution, in particular the wave reflection pattern inside the domain of a pipe with a discontinuous area. For this type of cross-sectional characteristics, the term $p\partial A/\partial x$ becomes an impulsive force per unit length acting on an infinitesimally small spatial interval. This means that when a fluid particle passes a location with discontinuity in the area, it experiences an excessively large force (an impulsive force) for an infinitesimally short period of time that leads to a finite change in the momentum of the particle. The effect of such impulsive forces cannot be captured appropriately by the classical finite-volume schemes. Therefore, other methods are needed to solve this system of equations.

In the following section, an eigenvalue analysis of the system (6) is carried out to explain the effect of a variable cross-sectional area on the solution.

2.2. Eigenvalue Analysis of the non-conservative DFM

To perform the eigenvalue analysis, $Q := [\alpha_g \quad u_l \quad p \quad A]^T$ is defined as the state variable vector and by inserting the closure laws into the PDEs (6), the system in (6) can be rewritten in a compact form as follows:

$$J_1(Q)\frac{\partial Q}{\partial t} + J_2(Q)\frac{\partial Q}{\partial x} = 0, \tag{7}$$

where the concise representation of J_1 and J_2 (by partially inserting the closure laws) are as below

$$J_1(Q) = \begin{bmatrix} -\rho_l & 0 & \frac{\alpha_l}{c_l^2} & 0 \\ \rho_g & 0 & \frac{\alpha_g}{c_g^2} & 0 \\ \rho_g u_g - \rho_l u_l + \alpha_g\rho_g \frac{K(K-1)u_l + S)}{(1-K\alpha_g)^2} & \alpha_l\rho_l + \alpha_g\rho_g\frac{K\alpha_l}{(1-K\alpha_g)} & \frac{\alpha_l u_l}{c_l^2} + \frac{\alpha_g u_g}{c_g^2} & 0 \\ 0 & 0 & 0 & 1 \end{bmatrix},$$

$$J_2(Q) = \begin{bmatrix} -\rho_l u_l & \alpha_l\rho_l & \frac{\alpha_l u_l}{c_l^2} & \frac{\alpha_l\rho_l u_l}{A} \\ \rho_g\frac{u_g - K\alpha_g u_l}{(1-K\alpha_g)} & \alpha_g\rho_g\frac{K\alpha_l}{(1-K\alpha_g)} & \frac{\alpha_g u_g}{c_g^2} & \frac{\alpha_g\rho_g u_g}{A} \\ a_{31} & a_{32} & \frac{\alpha_l u_l^2}{c_l^2} + \frac{\alpha_g u_g^2}{c_g^2} + 1 & 0 \\ 0 & 0 & 0 & 0 \end{bmatrix}. \tag{8}$$

where

$$a_{31} = \rho_g u_g^2 - \rho_l u_l^2 + 2\alpha_g\rho_g u_g\frac{K((K-1)u_l + S)}{(1-K\alpha_g)^2},$$

$$a_{32} = 2\alpha_l\rho_l u_l + 2\alpha_g\rho_g u_g\frac{K\alpha_l}{(1-K\alpha_g)}.$$

It should be noted that although the area is a known variable, it is considered to be one of the states of the system to facilitate the analyses and to enable writing system (6) in the format of (7). This is the main reason for keeping the last trivial equation in system (6). For the DFM, the eigenvalues of the matrix $J_1^{-1}J_2$ have the following form [5]:

$$\lambda_1 = u_l + \omega, \quad \lambda_2 = u_g, \quad \lambda_3 = u_l - \omega, \quad \lambda_4 = 0, \tag{9}$$

where ω is the speed of sound in the mixture of the gas and the liquid [5]. In case of no-slip, i.e., $K = 1$, $S = 0$, after computing the eigenvalues and casting the results into the format of (9), the speed of sound in the mixture can be analytically written as follows known as Wood or Wallis speed of sound [28, 29, 30]:

$$\omega = c_l c_g\sqrt{\frac{\rho_l\rho_g}{\bar{\rho}(\alpha_g\rho_l c_l^2 + \alpha_l\rho_g c_g^2)}}, \tag{10}$$

with $\bar{\rho} = \alpha_l\rho_l + \alpha_g\rho_g$.

In the case when slip occurs between the two phases, computing the analytical speed of sound in the mixture is complex, if not impossible. Thus, simplified surrogates for the speed of sound have been suggested;

for instance the surrogate in [5] is introduced for cases with $\alpha_g\rho_g \ll \alpha_l\rho_l$ and $0 < \alpha_g < 1$ as below:

$$\omega \simeq \sqrt{\frac{p}{\alpha_g\rho_l(1 - K\alpha_g)}}. \tag{11}$$

Notably, although the gas and the liquid phase play a symmetric role in (6), the contribution of the phases are non-symmetric in the eigenvalues (9) due to the closure laws (2)-(5). For a detailed analysis of the eigenvalue problem of the conservative DFM, the reader may refer to [31]. The eigenvalue λ_4 shows that there is a stationary wave in the computational domain that becomes visible when the cross-sectional area is discontinuous and $\partial A/\partial x$ becomes closer to the impulse function.

Remark 1. *Equation* (11) *becomes ill-posed when* α_g *tends to zero or* $K\alpha_g \to 1$. *When* $K > 1$, *the singular point even occurs for* $\alpha_g < 1$. *In these cases, other surrogate formulations should be used* [23], *which have not been studied in this paper.*

Remark 2. *In some special cases, the speed of sound* ω *becomes very low, even less than* c_g, *in the presence of both phases. However, in the special application of drilling for oil and gas, phase velocities are still lower than* ω *and the flow is subsonic. Henceforth, we only consider subsonic flows.*

In general, dynamics of the problems studied in this paper are the perturbation dynamics with respect to the steady-state solution. Thus, finding the steady-state solution is the first step towards solving this type of problems.

2.3. Steady-state solution

For obtaining the analytical steady-state solution of system (6), the partial derivatives of the variables with respect to time are set to zero and the following system of equations should be solved:

$$\frac{\partial(\alpha_l\rho_l u_l A)}{\partial x} = 0, \tag{12a}$$

$$\frac{\partial(\alpha_g\rho_g u_g A)}{\partial x} = 0, \tag{12b}$$

$$\frac{\partial((\alpha_l\rho_l u_l^2 + \alpha_g\rho_g u_g^2 + p)A)}{\partial x} = p\frac{\partial A}{\partial x}. \tag{12c}$$

By embedding (12a) and (12b) into (12c), simplified governing equations are obtained as in (13)

$$\frac{\partial(\alpha_l\rho_l u_l A)}{\partial x} = 0, \tag{13a}$$

$$\frac{\partial(\alpha_g\rho_g u_g A)}{\partial x} = 0, \tag{13b}$$

$$\alpha_l\rho_l u_l A\frac{\partial u_l}{\partial x} + \alpha_g\rho_g u_g A\frac{\partial u_g}{\partial x} + A\frac{\partial p}{\partial x} = 0. \tag{13c}$$

After inserting the closure laws and considering the slip law (3), the steady-state solution of the new state variable $W := [u_l \quad u_g \quad \alpha_g \quad p]^T$ is governed by the system of equations:

$$M(W, x)\frac{\partial W}{\partial x} = E(W, x), \tag{14}$$

where the concise representation of M and E (by partially inserting the closure laws) are as below

$$M(W, x) = \begin{bmatrix} -K(1-\alpha_g) & 1 - K\alpha_g & K(u_l - u_g) & 0 \\ (1-\alpha_g)\left(\frac{p-p_0}{c_l^2} + \rho_0\right) & 0 & -\left(\frac{p-p_0}{c_l^2} + \rho_0\right)u_l A & \frac{(1-\alpha_g)u_l A}{c_l^2} \\ 0 & \alpha_g\frac{p}{c_g^2}A & \frac{p}{c_g^2}u_g A & \alpha_g\frac{u_g A}{c_g^2} \\ (1-\alpha_g)\left(\frac{p-p_0}{c_l^2} + \rho_0\right)u_l & \alpha_g\frac{p}{c_g^2}u_g A & 0 & A \end{bmatrix},$$

$$E(W, x) = \begin{bmatrix} 0 \\ -(1-\alpha_g)\left(\frac{p-p_0}{c_l^2} + \rho_0\right)u_l\frac{\partial A}{\partial x} \\ -\alpha_g\frac{p}{c_g^2}u_g\frac{\partial A}{\partial x} \\ -\left((1-\alpha_g)\left(\frac{p-p_0}{c_l^2} + \rho_0\right)u_l^2 + \alpha_g\frac{p}{c_g^2}u_g^2\right)\frac{\partial A}{\partial x} \end{bmatrix}. \tag{15}$$

Notably, the term $\partial A/\partial x$ represents an impulsive term at the discontinuities of $A(x)$, which leads to discontinuities in the steady-state solution of W. To solve this system for discontinuous function $A(x)$, left- or right-continuity of the function should be specified to be able to define the area at any location.

The initial condition for the simulations in the presence of area variation is the solution of (14)-(15) unless otherwise mentioned. If a system starts from its unique steady-state solution, the numerical solution should remain on the same solution afterwards. Therefore, a significant discrepancy between the numerical simulation and the steady-state initial condition reveals the poor performance of the scheme, which may be hard to diagnose in dynamical simulations. Thus, this test is a powerful measure for assessing the necessary performance of a scheme, i.e., predicting the correct steady-state solution.

Equations (14)-(15) represent a two-point boundary value problem due to the boundary conditions specified at both ends, which are detailed in the next section.

2.4. Boundary conditions

As three PDEs are involved in the system of (14), three physical boundary conditions have to be specified. For subsonic flow, it is typical to set a specific mass flow rate of the liquid and the gas at the left boundary (at $x = 0$) and a specific pressure at the right boundary (at $x = L$) [5, 32]. Henceforth, the mass flow rate of the liquid and gas are, respectively, denoted by $\dot{m}_l$ and $\dot{m}_g$ (i.e., $\dot{m}_l := \alpha_l\rho_l u_l A$ and $\dot{m}_g := \alpha_g\rho_g u_g A$), and the pressure at the right boundary is denoted by p_R.

However, for finding the numerical solution of system (6), all conservative variables should be prescribed at the boundaries. Since the number of conservative variables at each boundary is more than the number of physical boundary conditions, additional conditions at the boundary are required to find the unique solution for the boundary variables. For instance, at the right boundary, only pressure is prescribed and other variables should be obtained by some compatibility equations. By following the approach described in [32], characteristic boundary conditions are combined with the physical boundary conditions in order to fulfill all the necessary conditions at the boundaries. The characteristic boundary equations can be found in [32]. Under the assumption of constant area only at the boundaries, the characteristic boundary equation corresponding to the pressure wave propagating in the downstream direction $\lambda_1 = u_l + \omega$ reads as:

$$\frac{\mathrm{d}}{\mathrm{d}t}p + \rho_l\omega(u_g - u_l)\frac{\mathrm{d}}{\mathrm{d}t}\alpha_g - \rho_l\alpha_l(u_g - u_l - \omega)\frac{\mathrm{d}}{\mathrm{d}t}u_l = 0,$$
$$\text{with} \quad \frac{\mathrm{d}}{\mathrm{d}t} = \frac{\partial}{\partial t} + (u_l + \omega)\frac{\partial}{\partial x}. \tag{16}$$

Similarly, for the gas volume wave $\lambda_2 = u_g$, we have:

$$\frac{\mathrm{d}}{\mathrm{d}t}p + \frac{p}{\alpha_g(1 - K\alpha_g)}\frac{\mathrm{d}}{\mathrm{d}t}\alpha_g = 0, \quad \text{with} \quad \frac{\mathrm{d}}{\mathrm{d}t} = \frac{\partial}{\partial t} + u_g\frac{\partial}{\partial x}. \tag{17}$$

Finally, for the pressure wave propagating in the upstream direction $\lambda_3 = u_l - \omega$, we have:

$$\frac{\mathrm{d}}{\mathrm{d}t}p - \rho_l\omega(u_g - u_l)\frac{\mathrm{d}}{\mathrm{d}t}\alpha_g - \rho_l\alpha_l(u_g - u_l + \omega)\frac{\mathrm{d}}{\mathrm{d}t}u_l = 0,$$
$$\text{with} \quad \frac{\mathrm{d}}{\mathrm{d}t} = \frac{\partial}{\partial t} + (u_l - \omega)\frac{\partial}{\partial x}. \tag{18}$$

The discrete version of equations (16) and (17) are solved at the right boundary and discrete version of equation (18) is solved at the left boundary.

Remark 3. *Before going through the numerical solvers, it should be noted that, in this paper, the function $A(x)$ is piecewise continuous and it is discretized over the spatial domain. After such discretization, $A(x)$ becomes piecewise constant as it is constant within each grid cell and the discontinuities occur only at the interfaces. Then, in the case of discontinuous area, wherever the computation of $\partial A/\partial x$ is required, for instance in the steady-state calculations, the spatial derivative of $A(x)$ is approximated by the finite difference method.*

Remark 4. *Some existing methods to deal with the variable cross-section are based on adapting the Rusanov scheme* [18]. *For the sake of a fair comparison, we also consider the Rusanov scheme as our numerical scheme. However, the method introduced in this paper is a universal modification that can be used along with any numerical scheme such as the AUSMV scheme* [5].

3. Numerical solvers for the DFM with piecewise continuous cross-section

In this section, different approaches are presented to deal with the non-conservative term in the DFM; some of which are proposed in this paper and some are extensions of existing methods for (6). The effects of variable cross-sectional area in the DFM and Euler equations are similar; a stationary wave is added to the existing waves in both cases. Therefore, the strategies introduced in different works such as [4, 8, 11, 12] to deal with non-conservative terms in the Euler equations with area variation are the main source of inspiration for this work.

For the sake of completeness, some terminologies widely used in the context of finite-volume method are introduced beforehand. For a general first-order PDE of the form

$$\frac{\partial u}{\partial t} + \frac{\partial}{\partial x}(f(u)) = S(u, t, x), \ \text{with } t \in \mathrm{I} = [0, \mathrm{T}], \ x \in \Omega = [0, \mathrm{L}], \tag{19}$$

u is called the conservative variable, f is called the mathematical flux function and S is the source term. Furthermore, primitive variables with physical interpretation are defined, denoted by v. For instance, for the system (1), the conservative variables are $u = [\alpha_l\rho_l \quad \alpha_g\rho_g \quad \alpha_l\rho_l u_l + \alpha_g\rho_g u_g]^T$ and primitive variables are any combination of three independent variables, such as $v = [\alpha_g \quad u_l \quad p]^T$. Finite-volume discretization is commonly employed to solve such PDEs by a discretization of the spatial computational domain Ω and the temporal computational domain I, as shown in Figure 2. Assume that we are interested in the solution at the i-th spatial grid cell at the time step $n + 1$ (the green block in Figure 2). First-order Godunov-type schemes numerically solve (19) by

$$U_i^{n+1} = U_i^n - \frac{\Delta t}{\Delta x}(F(U_i^n, U_{i+1}^n) - F(U_{i-1}^n, U_i^n)) + \Delta t\, S(U_i^n, t^n, x_i), \tag{20}$$

where U_i^n is the spatial average of the conservative variable u over i-th cell at the time instant $t^n = n\Delta t$, schematically shown at different grid cells by red lines in Figure 2. Similarly, V_i^n is the spatial average of the primitive variables v, which will be used later. Also, Δt and Δx refer to temporal and spatial discretization step sizes, respectively.

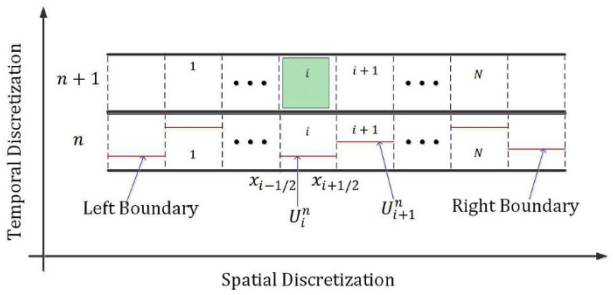

Figure 2. An illustration of the finite-volume spatial and temporal discretization; green block: the desired solution at the next time step, red lines: constant solutions within each grid cell at the current time step.

The numerical flux function F is a scheme-dependent function of the conservative variables. The classical Rusanov scheme [13] for the system (6) employs a flux function as below:

$$F(U_i^n, U_{i+1}^n) = \frac{f(U_{i+1}^n) + f(U_i^n)}{2} - \lambda_{i+1/2}^n(U_{i+1}^n - U_i^n), \tag{21}$$

with

$$f = [\alpha_l\rho_l u_l A, \quad \alpha_g\rho_g u_g A, \quad (\alpha_l\rho_l u_l^2 + \alpha_g\rho_g u_g^2 + p)A]^T, \tag{22a}$$

$$U = [\alpha_l\rho_l A, \quad \alpha_g\rho_g A, \quad (\alpha_l\rho_l u_l + \alpha_g\rho_g u_g)A]^T, \tag{22b}$$

and

$$\lambda_{i+1/2}^n = \frac{1}{2}\max(\{|u_l^n| + \omega^n, |u_g^n|\}_{i+1}, \{|u_l^n| + \omega^n, |u_g^n|\}_i), \tag{23}$$

where the operator "max"gives the maximum value of its arguments, and $\lambda_{i+1/2}^n$ is the half of maximum local eigenvalue of (9) computed at the left-hand and right-hand side of the interface $x_{i+1/2}$ at the time instant t^n. Below, various methods for dealing with the non-conservative term are presented.

3.1. First approach: source term approximation

The first approach involves considering the non-conservative term in (6), $p\partial A/\partial x$, as a source term. In other words in (20), the term $S(U_i^n, t^n, x_i)$ is taken equal to an approximation of $(p\partial A/\partial x)_i^n$, with the conservative variable vector and mathematical flux function as in (22). When the area is discontinuous, this source term approaches an impulsive force. Different approaches such as the one in [12] have tried to approximate this term in different ways.

3.2. Second approach: modified Rusanov scheme

The second approach is adopted from [14] for dealing with the non-conservative Euler equations by modifying the Rusanov scheme. Clain and Rochette in [14] adapted this scheme to enforce the numerical solution to be steady-state-preserving for zero flow for the system of the non-conservative Euler equations. The extension of the approach in [14] to the DFM is as below:

$$U_i^{n+1} = U_i^n - \frac{\Delta t}{\Delta x}((F(U_i^n, U_{i+1}^n) + G_{i+1/2}^{-,n}) - (F(U_{i-1}^n, U_i^n) + G_{i-1/2}^{+,n})), \tag{24}$$

with

$$F(U_i^n, U_{i+1}^n) = \frac{f(U_{i+1}^n)+f(U_i^n)}{2} - \lambda_{i+1/2}^n A_{i+1/2} \begin{bmatrix} (\alpha_l\rho_l)i+1_n - (\alpha_l\rho_l)i_n \\ (\alpha_g\rho_g)i+1_n - (\alpha_g\rho_g)i_n \\ (\alpha_l\rho_l u_l + \alpha_g\rho_g u_g)i+1_n - (\alpha_l\rho_l u_l + \alpha_g\rho_g u_g)i_n \end{bmatrix},$$
$$A_{i+1/2} = \max(A_{i+1}, A_i), \tag{25}$$

where A_i is the cross-sectional area at the center of i-th grid cell (it is assumed that the area is constant within each grid cell and only changes at the interfaces) and

$$G_{i+1/2}^{-,n} := -\frac{A_{i+1}-A_i}{2}\begin{bmatrix}0\\0\\p_i^n\end{bmatrix},\quad G_{i-1/2}^{+,n} := \frac{A_i - A_{i-1}}{2}\begin{bmatrix}0\\0\\p_i^n\end{bmatrix}. \tag{26}$$

In other words, the third entry of the following vector which appears in (24),

$$\frac{-1}{\Delta x}(G_{i+1/2}^{-,n} - G_{i-1/2}^{+,n}) = \frac{A_{i+1}-A_{i-1}}{2\Delta x}\begin{bmatrix}0\\0\\p_i^n\end{bmatrix}$$

approximates the term $p\partial A/\partial x$. Clain and Rochette in [14] prove that the modified scheme is well-balanced in the case of zero flow.

3.3. Third approach: novel, modified Rusanov scheme

The third method is inspired by the idea behind the second approach, by applying further modifications to the scheme in (25). The new modification, proposed here, is motivated by the need to capture the steady-state solution with higher accuracy. In the second approach, when evaluated at the steady-state solution at the presence of flow inside the domain, we obtain $U_i^{n+1} \neq U_i^n$, and therefore, the numerical solution deviates from the actual steady-state solution. This approach is motivated by enforcing the last entry of U_i^n, which is $((\alpha_l\rho_l u_l + \alpha_g\rho_g u_g)A)_i^n$, to be well-balanced. By using the fact that the mass flow rates of both phases are constant at every location during a steady-state solution, the new modification of the scheme is introduced by the flux function as given below:

$$F(U_i^n, U_{i+1}^n)_{i+1/2} = \frac{f(U_{i+1}^n)+f(U_i^n)}{2} - \lambda_{i+1/2}^n A_{i+1/2}\begin{bmatrix} (\alpha_l\rho_l)i+1_n - (\alpha_l\rho_l)i_n \\ (\alpha_g\rho_g)i+1_n - (\alpha_g\rho_g)i_n \\ \frac{\left(\alpha_l\rho_l u_l A + \alpha_g\rho_g u_g A\right)i+1_n}{A_{i+1/2}} - \frac{\left(\alpha_l\rho_l u_l A + \alpha_g\rho_g u_g A\right)i_n}{A_{i+1/2}} \end{bmatrix}, \tag{27}$$

with the same f and U mentioned in the previous section. In this case, while starting from the steady-state solution, the third entry of the flux function F computed by (27), i.e., $(\alpha_l\rho_l u_l A + \alpha_g\rho_g u_g A)_{i+1}^n - (\alpha_l\rho_l u_l A + \alpha_g\rho_g u_g A)_i^n$, becomes zero; therefore, at least the deviation of the third entry of conservative variable at the first time-step is zero and this modification outperforms the second approach. Similar to the second approach, this scheme reverts to the original Rusanov scheme when there is no change in the cross-sectional area.

3.4. Fourth approach: model-based modification

The next novel method, proposed here, is obtained through modifying the conservative variables before calculating the flux functions that allows one to treat the non-conservative term in an indirect way, regardless of the type of the Godunov scheme. The underlying idea is inspired by [8, 11] and consists of defining the solution as follows:

$$U_i^{n+1} = U_i^n - \frac{\Delta t}{\Delta x}(F(U_i^n, U_{i+1}^{*,n}) - F(U_{i-1}^{*,n}, U_i^n)), \tag{28}$$

where U_{i+1}^* and U_{i-1}^* are the modified conservative variables, which are henceforth called *starred* conservative variables. All conservative variables U and the mathematical flux function f (which will be used in the computation of F) in this approach are defined according to (1), not (6), as the effect of area is included in the starred variables, meaning that

$$\mathrm{U}=[\alpha_l\rho_l,\quad \alpha_g\rho_g,\quad \alpha_l\rho_l u_l + \alpha_g\rho_g u_g]^T,$$

$$\mathrm{f}=[\alpha_l\rho_l u_l,\quad \alpha_g\rho_g u_g,\quad \alpha_l\rho_l u_l^2 + \alpha_g\rho_g u_g^2 + p]^T.$$

First of all, an explanation to this approach is provided, and then, the computational steps for computing U_{i+1}^* and U_{i-1}^* at the i-th spatial grid cell is established to obtain the numerical solution by (28).

As mentioned in the eigenvalue analysis in Section 2.2, a stationary time-independent wave (corresponding to λ_4 in (9)) lies in the system that should be captured by (28). To this end, the method proposed in this section is composed of two steps. In the first step, the effect of the stationary wave generated by the non-conservative source term is captured. As the stationary waves are time-independent, steady-state model is employed to reconstruct this type of waves. In the second step, the effect of the non-stationary waves is taken into account. The latter waves are governed by (1) as the effect of the stationary wave is already considered in the first step.

This approach is visualized in Figure 3, where the first step mentioned above is denoted by ① and the second step is denoted by ②.

Assume that U_i^{n+1} is required (the green block in Figure 3). This grid cell is surrounded by two interfaces at $x_{i+1/2}$ and $x_{i-1/2}$. The conservative variables at the right-hand and left-hand side of the interface $i+1/2$ are shown by U_{i+1} and U_i, respectively, in Figure 3. Similarly, the left- and right-hand side values for the interface $i-1/2$ can be defined.

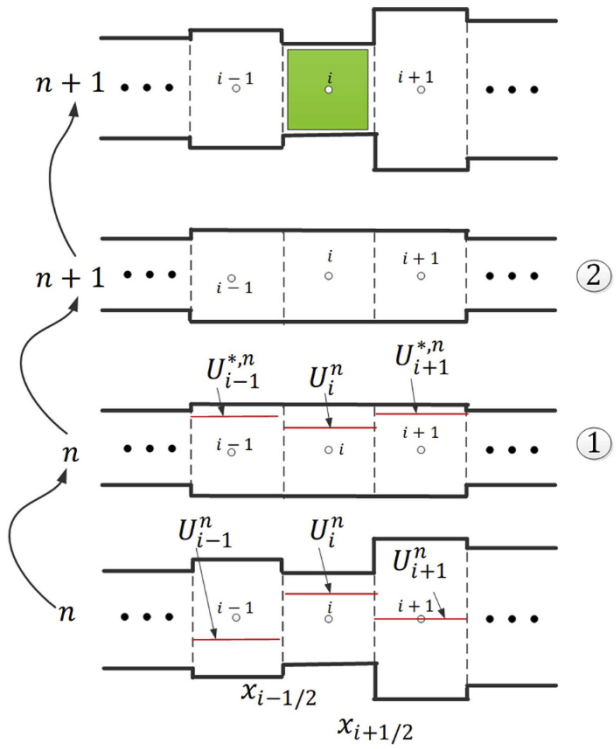

Figure 3. Finite-volume modification for the fourth approach, model-based modification.

In this approach, the conservative and primitive variables affecting the solution in the $i-$th cell, U_{i+1} and U_{i-1}, are modified such that these variables contain the effect of the stationary waves at the inlet and outlet of the cell. The starred values are denoted by U^*_{i+1} and U^*_{i-1} in Figure 3 at level ①. Now, as the system has a constant area only over the i-th grid cell and its neighboring cells, classical finite-volume discretization can be applied on (1) at level ① to obtain the solution at the i-th spatial grid cell. It should be noted that the area is assumed to be constant over only these three grid-cells while the area of other grid cells do not affect the solution of the i-th grid cell at the current time step $n+1$. Therefore, the solution obtained by (28) contains both the effect of the stationary and non-stationary waves.

After providing the intuition on how this method works, the framework for finding the starred values is established here. As the stationary waves are time-independent, the steady-state solution of the non-conservative system (6) is exploited to find algebraic constraints that capture the stationary waves. Recalling steady-state equations in (13), we have

$$\begin{aligned}
&\frac{\partial(\alpha_l\rho_l u_l A)}{\partial x} &&= 0,\\
&\frac{\partial\left(\alpha_g\rho_g u_g A\right)}{\partial x} &&= 0,\\
&A\left(\alpha_l\rho_l u_l\frac{\partial u_l}{\partial x} + \alpha_g\rho_g u_g\frac{\partial u_g}{\partial x} + \frac{\partial p}{\partial x}\right) &&= 0.
\end{aligned}$$

To find an algebraic relation over the area discontinuity, (13) should be integrated over the interface. However, (13c) is difficult to be integrated analytically over the spatial domain and needs more investigation. This differential equation can be simplified, as shown in the following Lemma 1.

Lemma 1. *The equation* (13c) *is equivalent to the following equation if both phases are present in the system:*

$$\begin{aligned}
&\bar{m}_g\left(u_g\frac{\partial u_g}{\partial x} + \frac{1}{\rho_g}\frac{\partial p}{\partial x}\right) + \bar{m}_l\left(u_l\frac{\partial u_l}{\partial x} + \frac{1}{\rho_l}\frac{\partial p}{\partial x}\right)\\
&\quad + (u_l - u_g)\left(\bar{m}_g\alpha_l\frac{\partial u_g}{\partial x} - \bar{m}_l\alpha_g\frac{\partial u_l}{\partial x}\right) = 0,
\end{aligned} \tag{29}$$

where $\bar{m}_l = A\alpha_l\rho_l u_l$ and $\bar{m}_g = A\alpha_g\rho_g u_g$.

Proof. From (13c), we have:

$$\bar{m}_g\frac{\partial u_g}{\partial x} + \bar{m}_l\frac{\partial u_l}{\partial x} + A\frac{\partial p}{\partial x} = 0.$$

As variables $\alpha_l u_l$ and $\alpha_g u_g$ are not constantly zero in general due to the presence of both phases, we can multiply the above equation by these two variables:

$$\alpha_l u_l\left(\bar{m}_g\frac{\partial u_g}{\partial x} + \bar{m}_l\frac{\partial u_l}{\partial x} + A\frac{\partial p}{\partial x}\right) = 0,$$

$$\alpha_g u_g\left(\bar{m}_g\frac{\partial u_g}{\partial x} + \bar{m}_l\frac{\partial u_l}{\partial x} + A\frac{\partial p}{\partial x}\right) = 0.$$

Summation of the above equations and using the identity $\alpha_g + \alpha_l = 1$ leads to:

$$\begin{aligned}
&\bar{m}_g\alpha_l u_l\frac{\partial u_g}{\partial x} + \bar{m}_l(1-\alpha_g)u_l\frac{\partial u_l}{\partial x} + A\alpha_l u_l\frac{\partial p}{\partial x} + \bar{m}_g(1-\alpha_l)u_g\frac{\partial u_g}{\partial x}\\
&\quad + \bar{m}_l\alpha_g u_g\frac{\partial u_l}{\partial x} + A\alpha_g u_g\frac{\partial p}{\partial x} = 0.
\end{aligned}$$

Rewriting the above relation leads to the claimed equation (29). ∎

The relation in (29) cannot be simplified further unless additional assumptions are made. In the following sections, we analyze the DFM in two categories.

3.4.1. DFM without slip

Assume that there is no slip between the two phases, i.e., $K = 1$ and $S = 0$ in (3) and subsequently

$$\hat{u}: = u_l = u_g. \tag{30}$$

In this case, as $u_l - u_g = 0$ in (29), system (13) changes to:

$$\frac{\partial(\alpha_l\rho_l\hat{u}A)}{\partial x} = 0,$$

$$\frac{\partial(\alpha_g\rho_g\hat{u}A)}{\partial x} = 0,$$

$$A\alpha_l\rho_l\hat{u}\left(\hat{u}\frac{\partial\hat{u}}{\partial x} + \frac{1}{\rho_l}\frac{\partial p}{\partial x}\right) + A\alpha_g\rho_g\hat{u}\left(\hat{u}\frac{\partial\hat{u}}{\partial x} + \frac{1}{\rho_g}\frac{\partial p}{\partial x}\right) = 0.$$

As $\partial p/\partial x = c_l^2\partial\rho_l/\partial x = c_g^2\partial\rho_g/\partial x$, the above equation is integrable over x. Therefore, over the interface, the following set of functions are set to be constant:

$$\alpha_l\rho_l\hat{u}A = \text{constant}, \tag{31a}$$

$$\alpha_g\rho_g\hat{u}A = \text{constant}, \tag{31b}$$

$$\alpha_l\rho_l\hat{u}A\left(\frac{\hat{u}^2}{2} + c_l^2\ln\rho_l\right) + \alpha_g\rho_g\hat{u}A\left(\frac{\hat{u}^2}{2} + c_g^2\ln\rho_g\right) = \text{constant}. \tag{31c}$$

Equations (31a)-(31b) represent the mass flow continuity at the interface. Equation (31c) governs the rate of energy exchange at the interface. In other words, the term $\hat{u}^2/2$ is the kinetic energy per unit mass of each phase. Also, $c_{l,g}^2\ln\rho_{l,g}$ is the potential energy of the compressible liquid and gas per unit mass. Therefore, at the interface, the mass and energy continuity should be preserved.

For instance, for finding $U^*_{M_1}$ from U_{M_1}, we should solve:

$$(\alpha_l\rho_l\hat{u})^*_{M_1}A_{M_2} = (\alpha_l\rho_l\hat{u}A)_{M_1}, \tag{32a}$$

$$(\alpha_g\rho_g\hat{u})^*_{M_1}A_{M_2} = (\alpha_g\rho_g\hat{u}A)_{M_1}, \tag{32b}$$

$$\begin{aligned}
&\left(\alpha_l\rho_l\hat{u}\left(\frac{\hat{u}^2}{2} + c_l^2\ln\rho_l\right) + \alpha_g\rho_g\hat{u}\left(\frac{\hat{u}^2}{2} + c_g^2\ln\rho_g\right)\right)^*_{M_1}A_{M_2}\\
&\quad = \left(\alpha_l\rho_l\hat{u}A\left(\frac{\hat{u}^2}{2} + c_l^2\ln\rho_l\right) + \alpha_g\rho_g\hat{u}A\left(\frac{\hat{u}^2}{2} + c_g^2\ln\rho_g\right)\right)_{M_1},
\end{aligned} \tag{32c}$$

where M_1 and M_2 refer to two neighboring cells, see Algorithm 1 for more details.

However, when the slip law is not discarded, finding an algebraic relation becomes hard as the third term $(u_l - u_g)(\bar{m}_g\alpha_l\partial u_g/\partial x - \bar{m}_l\alpha_g\partial u_l/\partial x)$ in (29) is not negligible. In order to extend the applicability of the fourth approach for cases with slip, extra physical assumptions should be made, which is dealt with below.

3.4.2. DFM with slip

In this case, the analytical integration of the momentum equation (13c) is challenging. In [33], the authors claim that the DFM cannot be endowed with an entropy pair unless restrictive assumptions such as no-slip are made. This fact that the integration of the momentum equation is challenging might be related to the lack of an entropy inequality. Alternatively, here, we try to impose some physical assumptions to be able to integrate the momentum equation.

It is assumed that at the interfaces of area variation, the ratio of volume and mass composition of the mixture do not change (in other words, still mass continuity is maintained). This assumption is valid when one of the phases is dominant in volumetric sense in the pipe or the area varies smoothly. Otherwise, in situations where both phases occupy the space rather equally and the area variation is sudden, this assumption is less accurate. These two assumptions result in constant volumetric fraction and mass fraction of each phase at the interface, respectively. Meaning that at each interface, the following conditions hold:

$$\frac{\alpha_l}{\alpha_g + \alpha_l} = \text{constant} \Rightarrow \alpha_{l,g} = \text{constant}, \tag{33a}$$

$$\frac{\alpha_l \rho_l}{\alpha_l \rho_l + \alpha_g \rho_g} = \text{constant} \Rightarrow \frac{\rho_l}{\rho_g} = \text{constant}. \tag{33b}$$

Then (13c) is rewritten as below:

$$A\rho_g\left(\alpha_l \frac{\rho_l}{\rho_g} u_l \frac{\partial u_l}{\partial x} + \alpha_g u_g \frac{\partial u_g}{\partial x} + \frac{1}{\rho_g}\frac{\partial p}{\partial x}\right) = 0 \overset{A\rho_g \neq 0}{\Rightarrow} \alpha_l \frac{\rho_l}{\rho_g}\frac{u_l^2}{2} + \alpha_g \frac{u_g^2}{2} + c_g^2 \ln\rho_g = \text{constant}.$$

Finally, the set of algebraic constraints under the set of assumptions mentioned in (33) for $\rho_g > 0$ is defined as:

$$\alpha_l \rho_l u_l A = \text{constant}, \tag{34a}$$

$$\alpha_g \rho_g u_g A = \text{constant}, \tag{34b}$$

$$\alpha_l \frac{\rho_l}{\rho_g}\frac{u_l^2}{2} + \alpha_g \frac{u_g^2}{2} + c_g^2 \ln\rho_g = \text{constant}. \tag{34c}$$

Still the mass continuity exactly holds. The kinetic energy of both phases and the potential energy of the gaseous phase can still be detected in (34c). This is due to the assumption that we consider that one of the phases is dominant in space. Therefore, the potential energy due to the expansion of the dominant phase, here gas, is only reflected in the algebraic relation. Moreover, due to the assumption of the prevalence of one phase, the area has been disappeared from (34c). We emphasize again if both phases are rather equally present in the pipe and the area variation is sudden, the relation (34c) is not accurate.

Similar to the previous set of assumptions, for finding $U^*_{M_1}$ from U_{M_1}, the following set of algebraic equations should be solved:

$$(\alpha_l \rho_l u_l)^*_{M_1} A_{M_2} = (\alpha_l \rho_l u_l A)_{M_1}, \tag{35a}$$

$$(\alpha_g \rho_g u_g)^*_{M_1} A_{M_2} = (\alpha_g \rho_g u_g A)_{M_1}, \tag{35b}$$

$$\left(\alpha_l \frac{\rho_l}{\rho_g}\frac{u_l^2}{2} + \alpha_g \frac{u_g^2}{2} + c_g^2 \ln\rho_g\right)^*_{M_1} = \left(\alpha_l \frac{\rho_l}{\rho_g}\frac{u_l^2}{2} + \alpha_g \frac{u_g^2}{2} + c_g^2 \ln\rho_g\right)_{M_1}, \tag{35c}$$

where M_1 and M_2 refer to the neighboring cells, see Algorithm 1 for more details.

All steps involved in the fourth approach are summarized in Algorithm 1. Now, a justification on the performance of this approach is presented in the following claims.

Algorithm 1. Fourth approach: model-based modification.

Input: $U^n_{i-1}, U^n_i, U^n_{i+1}, A_{i-1}, A_i, A_{i+1}$
Output: $U^{n+1}_i = ([\alpha_l\rho_l \;\; \alpha_g\rho_g \;\; \alpha_l\rho_l u_l + \alpha_g\rho_g u_g]^T)^{n+1}_i$

Compute primitive variables, $V^n_{i-1}, V^n_i, V^n_{i+1}$, from conservative variables, $U^n_{i-1}, U^n_i, U^n_{i+1}$ [12],
if $A_{i+1} \neq A_i$ **then**
  Solve (32) or (35), based on the assumption taken in Section 3.4, with $M_1 = i+1$ and $M_2 = i$, obtain $V^{*,n}_{i+1}$ and then $U^{*,n}_{i+1}$
else
  $U^{*,n}_{i+1} = U^n_{i+1}$
end if
if $A_i \neq A_{i-1}$ **then**
  Solve (32) or (35), based on the assumption taken in Section 3.4, with $M_1 = i-1$ and $M_2 = i$, and obtain $V^{*,n}_{i-1}$ and then $U^{*,n}_{i-1}$,
else
  $U^{*,n}_{i-1} = U^n_{i-1}$
end if
Compute U^{n+1}_i via (28).

Claim 1. *For any given U^0_i in $x_i \in [0, L]$ that satisfies (13), then $U^n_i = U^0_i \;\; \forall \;\; n \in \mathbb{N}$, if no-slip condition (30) is assumed to obtain the solution using Algorithm 1.*

Proof. Starting from a steady-state solution U^0_i, according to (13) and using (31), we have:

$$(\alpha_l\rho_l\hat{u}A)_{M_2} = (\alpha_l\rho_l\hat{u}A)_{M_1}, \tag{36a}$$

$$(\alpha_g\rho_g\hat{u}A)_{M_2} = (\alpha_g\rho_g\hat{u}A)_{M_1}, \tag{36b}$$

$$\left(\alpha_l\rho_l\hat{u}A\left(\frac{\hat{u}^2}{2} + c_l^2\ln\rho_l\right) + \alpha_g\rho_g\hat{u}A\left(\frac{\hat{u}^2}{2} + c_g^2\ln\rho_g\right)\right)_{M_2} = \left(\alpha_l\rho_l\hat{u}A\left(\frac{\hat{u}^2}{2} + c_l^2\ln\rho_l\right) + \alpha_g\rho_g\hat{u}A\left(\frac{\hat{u}^2}{2} + c_g^2\ln\rho_g\right)\right)_{M_1}. \tag{36c}$$

Comparing equations (36) with (32) reveals that $U^*_{M_1} = U_{M_2}$. Using this property in (28), by replacing M_1 and M_2as described in Algorithm 1 yields

$$U^{n+1}_i = U^n_i - \frac{\Delta t}{\Delta x}(F(U^n_i, U^n_i) - F(U^n_i, U^n_i)) = U^n_i. \tag{37}$$

Solving (37) recursively yields $U^n_i = U^0_i$. Thus, the proposed scheme captures the steady-state solution exactly. For the case with slip and assumptions (33), the scheme captures the steady-state solution only approximately.

Claim 2. *In case of constant cross-sectional area, i.e., $\partial A/\partial x = 0$, the solution U^n_i obtained from (28) is equal to that obtained from (20) if no-slip condition (30) is assumed.*

Proof. For the case of constant area over two neighboring cells and assuming no-slip condition, (32) reduces to

$$(\alpha_l\rho_l\hat{u})^*_{M_1} = (\alpha_l\rho_l\hat{u})_{M_1},$$
$$(\alpha_g\rho_g\hat{u})^*_{M_1} = (\alpha_g\rho_g\hat{u})_{M_1},$$
$$\left(\alpha_l\rho_l\hat{u}\left(\frac{\hat{u}^2}{2} + c_l^2\ln\rho_l\right) + \alpha_g\rho_g\hat{u}\left(\frac{\hat{u}^2}{2} + c_g^2\ln\rho_g\right)\right)^*_{M_1} = \left(\alpha_l\rho_l\hat{u}\left(\frac{\hat{u}^2}{2} + c_l^2\ln\rho_l\right) + \alpha_g\rho_g\hat{u}\left(\frac{\hat{u}^2}{2} + c_g^2\ln\rho_g\right)\right)_{M_1},$$

where a candidate solution would be $U^*_{M_1} = U_{M_1}$. Then, by following Algorithm 1, (28) reduces to

$$U^{n+1}_i = U^n_i - \frac{\Delta t}{\Delta x}(F(U^n_i, U^n_{i+1}) - F(U^n_{i-1}, U^n_i)).$$

This is similar to (20) with zero source terms (since area is constant and $\partial A/\partial x = 0$) and the modified scheme reverts back to the classical scheme. This feature is reflected in Algorithm 1 to accelerate the numerical solution. Again we should mention that for the case with slip and assumptions (33), the scheme recovers the classical scheme only approximately when the area is constant.

Remark 5. *After finding the starred values through solving the algebraic*

constraints, the numerical solution of (6) can be computed. If the starred-values are not found, one cannot compute the numerical solution by this method and other methods should be followed. Since these constraints exploit the steady-state equation (13), there is the possibility that these constraints are not satisfied either when starting at initial conditions far from the steady-state solution or when abrupt perturbations occur inside the domain. Notably, the algebraic constraints (32) and (35) may also have multiple solutions. Although the assumption of starting close to the steady-state solution is restrictive, there are many applications in the industry for which the analysis of perturbations with respect to the steady-state solution is important. In addition, studying the perturbations of steady-state solution of different systems has been the subject of many other studies [34, 35]. Moreover, this work can be the first step towards solving the non-conservative DFM by understanding the restrictions of the current approach. For a more in-depth discussion on features of the solution of the algebraic constraints, refer to Appendix A at the end of this paper, where the procedure to choose the feasible solution in case of multiple solutions is also explained.

In the following section, numerical results associated with each approach are discussed.

4. Numerical Results

Numerical results in this section are divided into five categories. First, in order to find the best scheme to solve system (6), the methods introduced in Section 3 have tested their ability to preserve the steady-state solution of system (6) with a piecewise constant cross-sectional area. Second, the most accurate approach, in the sense of capturing the steady-state solution, is used to compute the solution of (6) by imposing no variation in cross-sectional area in order to compare its performance with the solution obtained from the classical scheme of (21) applied to (1). Third, the selected approach has been tested for a transient flow modeling in a horizontal pipe with piecewise constant cross-sectional area. Fourth, the method is tested on a piecewise continuous cross-sectional area, both for capturing the steady-state solution and performing transient simulations. Finally, an error convergence study is performed.

The values of the parameters involved in system (6) are summarized in Table 1. The steady-state solution of (14) is acquired by the bvp4c solver of MATLAB. This solver approximates the solution to (13) in an iterative way while considering the boundary values at both ends of the computational domain [36].

Remark 6. *In Sections 4.1 and 4.2 for the fourth approach, lines 2,4 − 7,9 − 11 of Algorithm 1 are ignored to test the performance of the new model-based modified scheme to automatically recover the classical scheme in locations where the area is constant. After becoming assure of the performance at constant area locations, the entire Algorithm 1 is used in other sections.*

Remark 7. *As mentioned before, to make fair comparisons between this approach and the second and the third approaches introduced in previous sections, we use the Rusanov scheme as the case study. However, the modification introduced in the fourth approach can be applied to other finite-volume schemes in a similar manner; only the numerical flux function F in (21) should be changed according to the finite-volume scheme.*

Remark 8. *The Rusanov scheme is subject to the CFL condition*

$$\Delta t = CFL \frac{\Delta x}{\max(|\lambda_1|, |\lambda_2|, |\lambda_3|, |\lambda_4|)}, \tag{38}$$

where λ_i, $i \in \{1,2,3,4\}$ are given by (9). For all simulations in this section, we estimate $\max(|\lambda_1|, |\lambda_2|, |\lambda_3|, |\lambda_4|) \approx c_l$ and set $CFL = 1$. Then, according to the chosen Δx, the temporal discretization Δt is specified.

Table 1
Test case parameters.

ρ_0	p_0	$\dot{m}_l$	$\dot{m}_g$	c_g	c_l
1000 kg/m^3	1 bar	0.3 kg/s	0.003 kg/s	316 m/s	1000 m/s

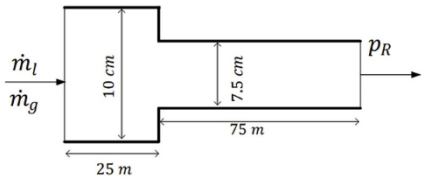

Figure 4. Configuration of the computational domain.

Remark 9. *To the best of authors' knowledge, no Riemann solution for the DFM with variable cross-sectional area has been published. Before doing any transient simulations, the performance of the scheme at the steady state is evaluated. For transients, the performance of the scheme is assessed against the classical Rusanov scheme for the case of constant cross sectional area along the pipe. For a reference solution for piecewise constant area, refer to Appendix B. For a general piecewise continuous cross-sectional area, no reference solution exists for transient simulations.*

4.1. Preservation of the steady-state solution

This section is dedicated to checking the steady-state preservation of the numerical approaches proposed in Section 3. Since for the set of algebraic relations (31) in the fourth approach, no slip between the phases is considered, i.e., $K = 1$ and $S = 0$, we apply the same condition in this section to perform a fair comparison between different approaches. Figure 4 shows the computational domain for this case study that is a horizontal pipe with one discontinuity in diameter along its length. Moreover, the time horizon is 1 s with discretization steps $\Delta x = 1$ m. The pressure at the right boundary is also $p_R(t) = 1$ bar. It should be noted as the simulation is stopped at $t = 1$ s, there are still some transient effects in the solution.

4.1.1. First approach: source term approximation

The numerical solution of (6) obtained by the first approach mentioned in Section 3.1 in comparison with the solution of system (13) is shown in Figure 5.

Clearly, this kind of non-conservative remedy is afflicted by non-physical peaks at the locations of the discontinuities in the cross-sectional area where the impulsive force lies. As this method fails to capture the steady-state solution, it is not selected for further investigation by transient simulations.

4.1.2. Second approach: modified Rusanov scheme

After modifying the Rusanov scheme as explained in Section 3.2, the solution of this test case is shown in Figure 6.

Clearly, this modification suffers from non-physical jumps at the locations of the area discontinuities. This should not be a surprise since this modification is proved in [14] to be well-balanced only in the case of zero flow inside the domain. However, in the presence of flow, the performance of this scheme is not necessarily satisfactory in the sense that it is incapable of preserving the steady-state solution, similar to the presented results. Therefore, this method is also not studied further in this paper.

4.1.3. Third approach: novel, modified Rusanov scheme

The results for the third type of modification is shown in Figure 7.

Apparently, the results of the new modified Rusanov are better than the first and second approach in preserving the steady-state solution except for relatively small discontinuity jumps in the mass flow rate. These jumps are related to the approximation of the integral $\int_{x_{i-1/2}}^{x_{i+1/2}} p\, \partial A/\partial x\, dx$ by $p_i(A_{i+1} - A_{i-1})/2$. This numerical deficiency pollutes the numerical solutions. Another weakness of this approach is that by increasing the spatial rate of cross-section variation in the

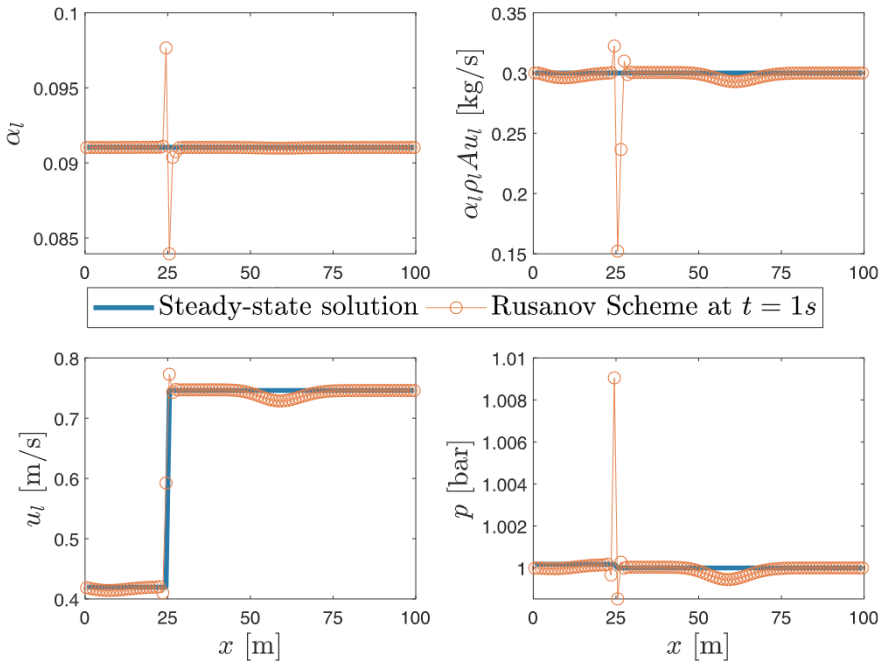

Figure 5. Liquid phase variables of system (6) by using original Rusanov scheme on variable area and the first approach: source term approximation.

discretized sense at a certain location (i.e., higher jumps in the cross section and a larger impulsive force), the solution deviates from the actual steady-state solution even further. Therefore, this method is also not selected for further investigation.

4.1.4. Fourth approach: model-based modification

The numerical results obtained by using the fourth approach with the set of algebraic constraints in (31) are demonstrated in Figure 8.

The numerical results show a significant accuracy in the preservation of the steady-state solution of the PDEs (6). Compared to the previous results, pressure and mass flow rate are preserved with significantly higher accuracy. The small deviation from steady-state is due to the error in solving the algebraic relations (31).

The simulation results for the set of algebraic constraints in (34) are depicted in Figure 9.

This set of assumptions also performs well in capturing the steady-state solution. As obvious from the top-left side of Figure 9, the gas phase is dominant here and α_l, and subsequently α_g, change negligibly over the interface. In addition, due to the very small change of pressure apparent from bottom-right side of Figure 9, the assumption of constant ρ_l/ρ_g over the interface is also valid.

Comparing all the results, the last method outperforms the other methods in capturing the steady-state solution. Therefore, the proposed modification in Section 3.4 together with the set of algebraic constraints (31) and (34) has been used for transient simulations. In these simulations, if the no-slip condition is imposed, the set of algebraic constraints (31) is used; otherwise, the algebraic constraints at the location of area variation are governed by (34). Since this approach uses a

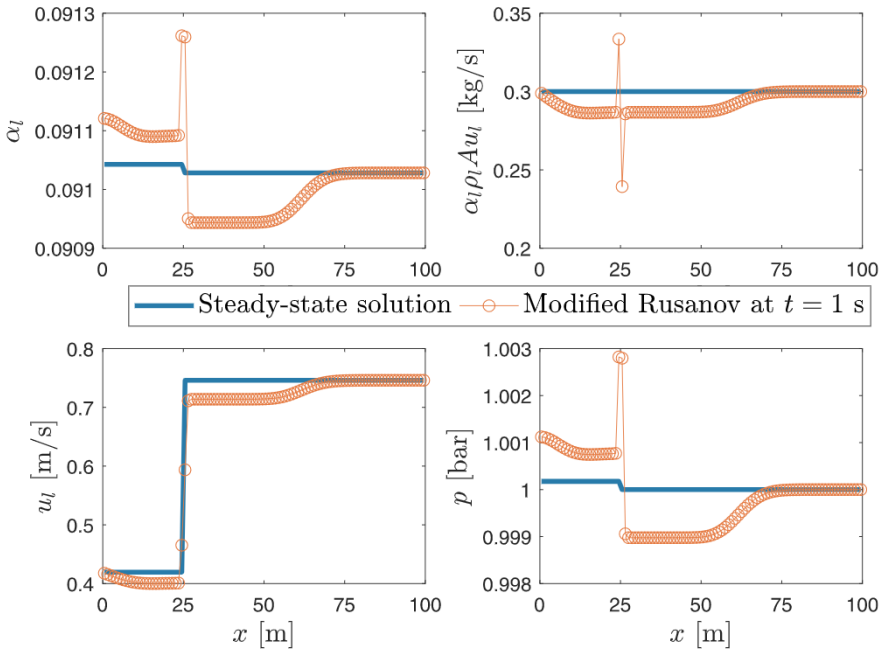

Figure 6. Liquid phase variables of system (6) by using Rusanov scheme on variable area and the second approach: modified Rusanov scheme in Section 3.2.

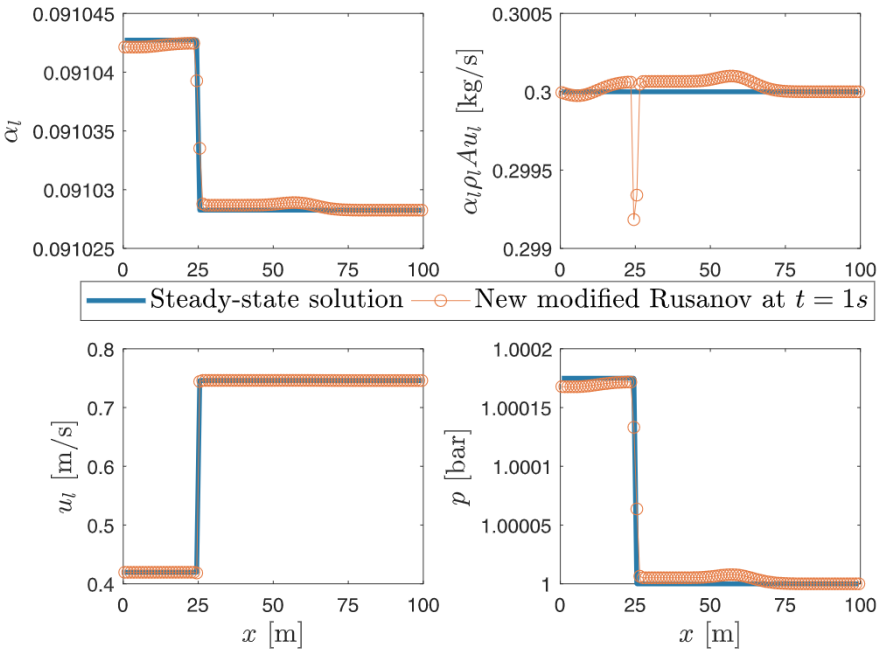

Figure 7. Liquid phase variables of system (6) by using Rusanov scheme on variable area and the third approach: novel, modified Rusanov scheme in Section 3.3.

model-based modification, it does not suffer from any non-physical discontinuities in the solution of the state variables.

4.2. Comparisons in case of constant area

In this section, the performance of the proposed scheme to accurately characterize the dynamic behavior of the system in the case of constant area is analyzed. In order to do so, the result of the classical Rusanov scheme (21) applied to (1) is compared with the result of the model-based modified Rusanov scheme (31) or (34) applied to (6) in case of constant cross-sectional area. It should be noted again that the full Algorithm 1 is not implemented here as mentioned in Remark 6.

For the case of constant cross-sectional area, various benchmark tests for the DFM have been introduced. One well-known benchmark test is the DFM shock-tube problem, where the parameters of the simulation are taken from [5]. A horizontal pipe with the constant diameter of 0.1 m and length of 100 m is divided into two sections at the middle length of the pipe. For the left half of the pipe, the initial data are as below:

$$\alpha_g = 0.55,\ u_l = 10.37 \text{ m/s},\ p = 80450 \text{ Pa}.$$

For the right half of the pipe, we set

$$\alpha_g = 0.55,\ u_l = 0.561 \text{ m/s},\ p = 24282 \text{ Pa}.$$

In addition, discretization steps are $\Delta x = 1$ m, and $K = 1.07$ and $S = 0.216$.

First, we apply the modified Rusanov scheme (28) along with (34) on system (6) and compare the results with the original Rusanov

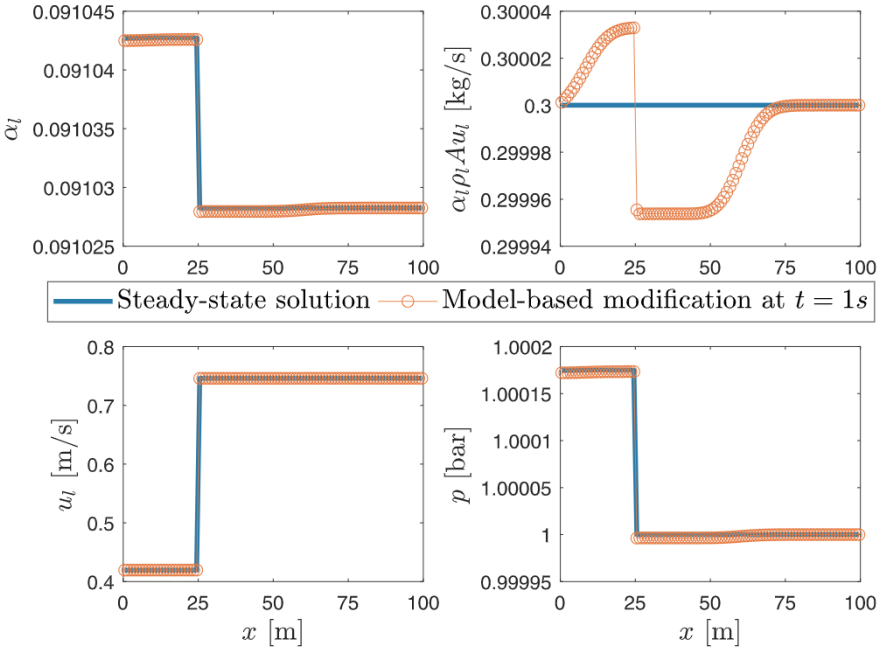

Figure 8. Liquid phase variables of system (6) by using Rusanov scheme on variable area and the fourth approach, model-based modification, together with (31).

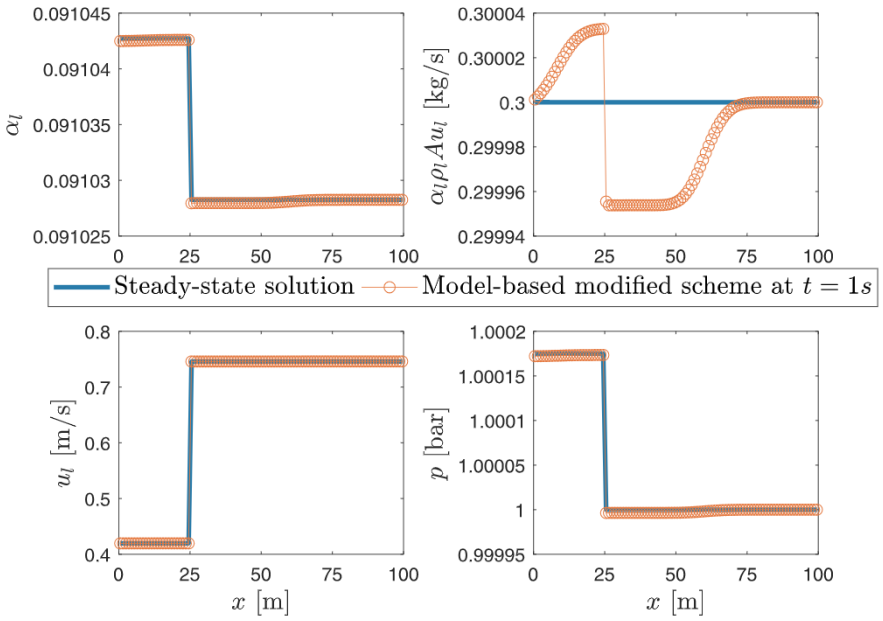

Figure 9. Liquid phase variables of system (6) by using Rusanov scheme on variable area and the fourth approach, model-based modification, together with (34).

scheme (21) applied to system (1). Both solutions should correspond exactly with each other, as seen in Figure 10. As the area is constant, the assumptions made for the DFM with slip as in (33) are valid. The reference solution is obtained on a fine discretization of $\Delta x = 0.1$ m with the classical Rusanov scheme.

Thus, in order to reduce the computational cost, the algebraic relations of (31) and (34) are enforced only at the locations where the cross-section varies. At the other locations, we set $U^*_{i+1} = U_{i+1}$ and $U^*_{i-1} = U_{i-1}$ as already noted in Algorithm 1.

4.3. Wave reflection in the presence of piecewise constant cross section

In this section, transients near the steady-state solution for a flow inside a pipe with piecewise constant cross-section are analyzed. At the location of discontinuous cross-section, any pressure wave is partially reflected back. Therefore, presence of the discontinuous cross-section dramatically affects the frequency response and the natural frequency of the system, which highly depends on the location and number of area variations. This kind of behavior has to be captured by the numerical simulation. In this section, the wave reflection behavior in the model-based modified Rusanov scheme together with (31) in both cases of discontinuous and constant cross-section of area are compared as another criterion for assessing the performance of the scheme.

The wave propagation can be excited by variation of mass flow rates at the left boundary or a pressure change at the right boundary. In this simulation, the pressure at the right boundary $p_R(t)$ is increased from 1 bar to 1.2 bar at $t = 1$ s to initiate a propagating pressure wave inside the domain. Other simulation parameters are shown in Table 1 with $K = 1$ and $S = 0$ with the pipe shown in Figure 4. The comparison of pressure wave propagation and reflection between two boundaries and area discontinuities can be observed in Figure 11 and 12.

The reference solution is obtained as explained in Appendix B. In Figure 11, the reference solution is obtained on a coarse with $\Delta x = 1$ m (the same spatial resolution as the solution with the modified scheme) and a fine grid with $\Delta x = 0.1$ m. Result of the modified scheme and the reference solution are very close to each other. It can be observed that

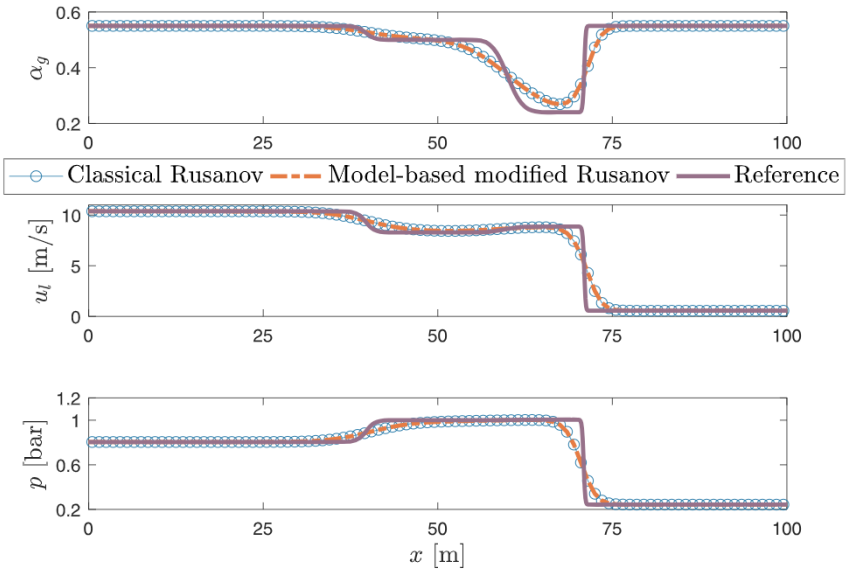

Figure 10. Performance of model-based modified and classical Rusanov scheme for shock tube test, constant area.

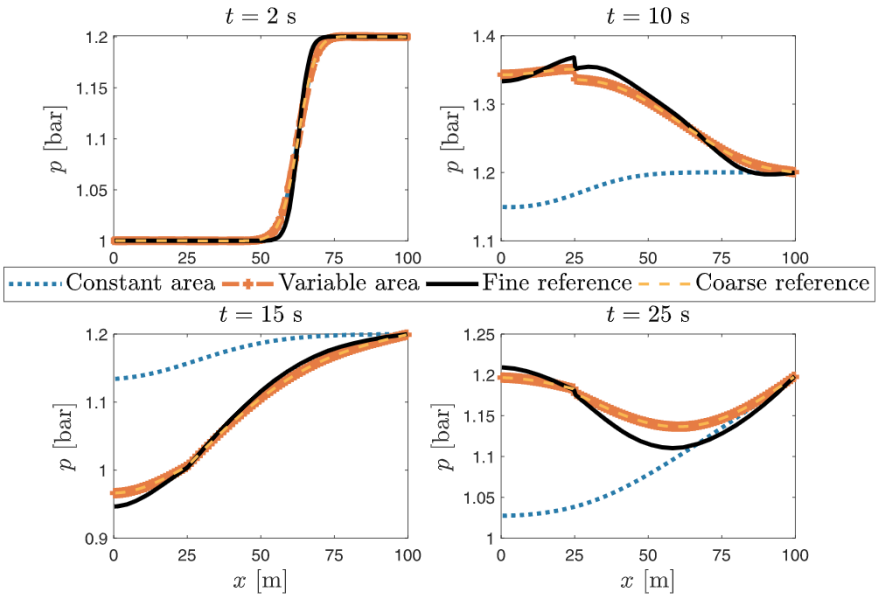

Figure 11. Effect of discontinuous cross section in pressure reflection (the variable cross-section is defined in Figure 4 for the top case and the constants cross section is with diameter of 7.5 cm for the bottom case).

the pressure front generated at the location of discontinuous area (in this case at $x = 25$ m which is shown by dashed black line in Figure 12) opposes the incoming pressure waves and this front partially reflects back the pressure waves as obvious from the top part of Figure 12 at around $t = 3$ s and similarly at the other time instants. This feature, which changes the wave propagation pattern inside the domain, has been well predicted by the scheme. In case of constant area, no pressure reflection occurs until the pressure wave reaches the other boundary.

Remark 10. This example resembles a choke plugging scenario within managed pressure drilling operations. When the mud gets stuck in the choke installed at the top of the annulus, the choke pressure experiences a sudden increase. Due to this pressure increase, a pressure wave propagates inside the annulus, which can be analyzed similarly to the example in this section by adding relevant friction and gravity source terms into the governing equations.

4.4. Piecewise continuous cross section

Here, a two-phase flow inside a converging-diverging nozzle is investigated. The dimensions of the pipe are shown in Figure 13. The

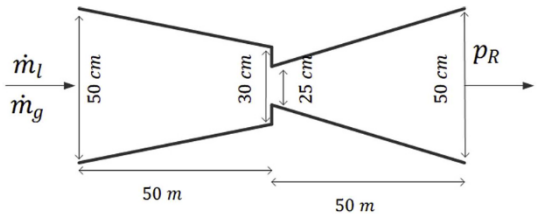

Figure 13. Dimension of the pipe with piecewise continuous cross-section.

simulation parameters are the same as in Section 4.3. Figure 14 depicts the gas velocity at different time instants.

The top-left plot in Figure 14 shows that the steady-state solution is captured well by the numerical scheme. Then, by increasing the pressure at the right boundary, the opposition force at the right boundary lowers the velocity inside the domain. This test case shows the capability of the proposed scheme both in capturing the steady-state solution and in the transient simulation of two-phase flow inside a pipe with piecewise continuous cross section.

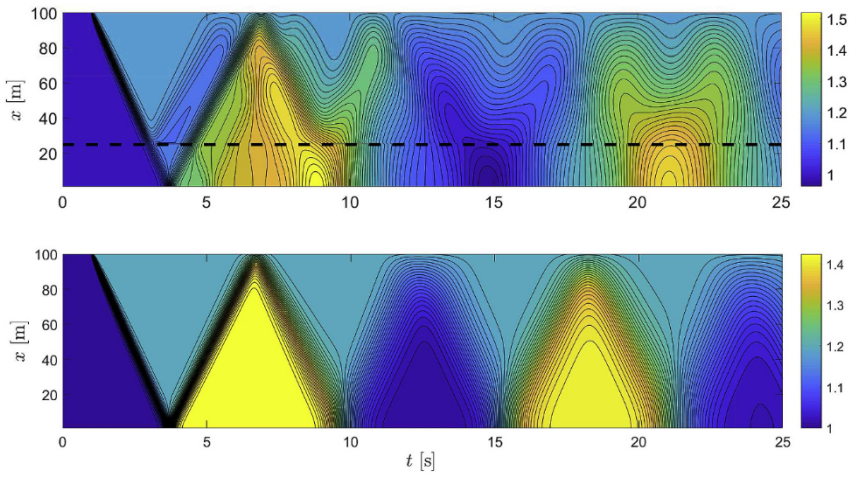

Figure 12. Space-time graph for pressure [bar] wave reflection pattern; top:variable cross section as in Figure 4, bottom: constant cross section with diameter of 7.5 cm.

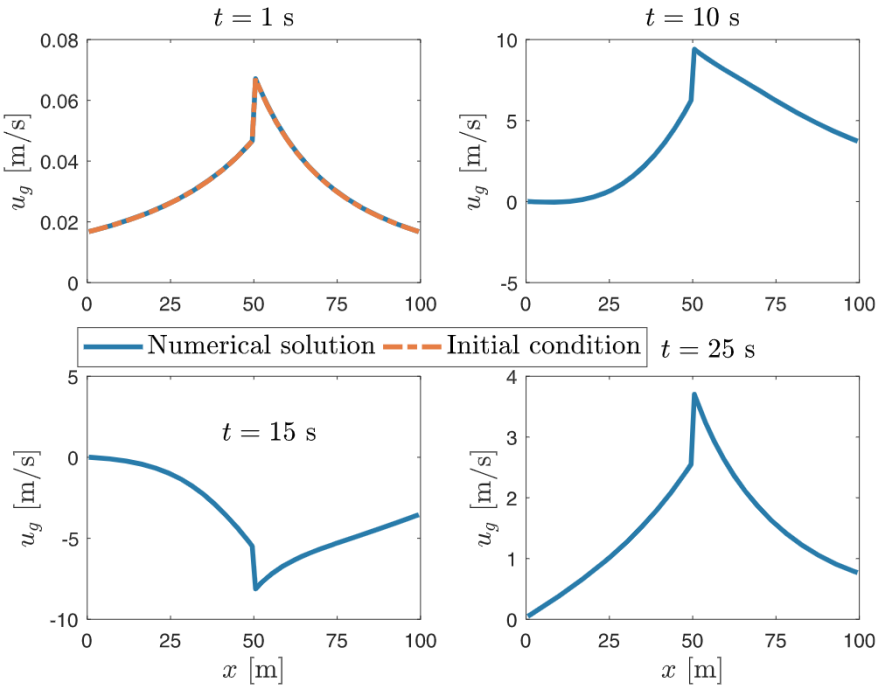

Figure 14. Gas velocity at different time instants.

4.5. Error convergence analysis

To accurately study the error convergence of the scheme, a test case should be introduced such that other aspects of the numerical solution does not affect the accuracy. For instance, $\partial A/\partial x$ and the mixture speed of sound ω should be analytically known. Therefore, a pipe with continuous cross section is selected as shown in Figure 15, which defines $\partial A/\partial x$ analytically. To know the analytical speed of sound, no slip condition is set, i.e., $K = 1$ and $S = 0$; then, ω is governed by (10). Other parameters are taken from Table 1. Boundary conditions do not change ($p_R(t) = 1$ bar) and the system remains on its steady-state.

In order to study convergence properties of the scheme, the number of grid-cells (N) are varied, the problem is solved with the model-based modified Rusanov scheme at other values for Δx (i.e., other number of grid-cells) and the solution (here the gas velocity) is compared with the reference solution at the last time instant, $t = 1$ s. The error is defined as the relative difference between the numerical gas velocity at the last time instant and the initial gas velocity at all locations, as in (39),

$$e = \frac{||u_g(x,\,1) - u_g(x,\,0)||_{L_r}}{u_g(x,\,0)_{L_r}}, \tag{39}$$

where $\|\cdot\|_{L_r}$ is the L_r norm of its argument over the spatial domain. The values for the error indicator (39) with increasing the number of the cells are reported in Table 2 and in Figure 16 for $r = 2, \infty$. The absolute value of the slope of each line is also depicted in this figure, confirming that the proposed scheme does not affect the order of accuracy of the underlying scheme (it is well-known that the classical Rusanov scheme is first order accurate [18]).

The small discrepancy between the order of accuracy at different level of the number of grid cells is due to the inaccuracy in solving the nonlinear algebraic constraints (31).

All discussions in this paper focused on first-order schemes; the extension to higher-order scheme can be done, which is beyond the scope of this paper. This will be the topic of future works.

Generally, this approach of dealing with variable cross-sectional area is problematic when the system (6) starts far from steady-state

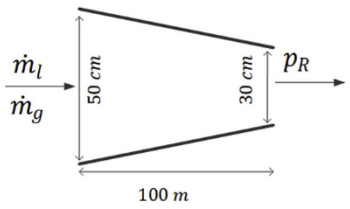

Figure 15. Dimension of the pipe with continuous cross-section to study the error convergence.

Table 2
Relative error convergence for the model-based, modified Rusanov scheme.

Number of cells	$r = 2$	$r = \infty$
50	0.012	0.0289
100	0.0061	0.0143
200	0.0031	0.0070
400	0.0015	0.0033
800	0.00076	0.0016

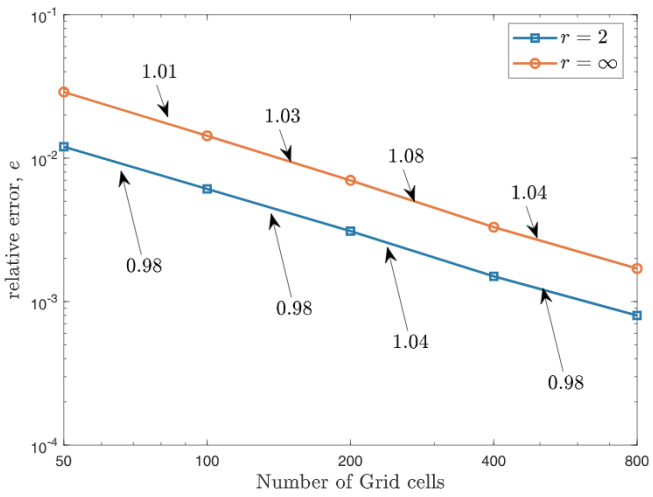

Figure 16. Relative error convergence by increasing the number of the grid cells with the model-based modified Rusanov scheme together with (31).

solution or when it is used for simulating abrupt dynamics. In this setting, an analysis has been presented in Appendix A.

5. Conclusions

This paper studied numerical solvers for the non-conservative Drift Flux Model in the presence of variable cross-sectional area. Different numerical approaches have been proposed and compared to the existing approaches in the sense of accurate preservation of the steady-state solution. It has been shown that one of the new proposed schemes, the model-based modified scheme, indeed captures the physical steady-state solution with an acceptable accuracy. The model-based modified scheme can be applied to piecewise continuous cross-sectional areas as well. This modified scheme reduces to the classical scheme in case of constant area and it is also shown that the modified scheme enables simulation of the wave reflection in case of discontinuous cross-sectional area. It has been numerically proved that the proposed modification retains the first order of accuracy of the underlying scheme. Based on the performance of the proposed scheme, it can be used for simulation of industrial applications such as the hydraulics of two-phase flow occurring in drilling for oil and gas in a well with discontinuous cross-sectional area.

Funding

This research has been carried out in the HYDRA project, which has received funding from the European Union's Horizon 2020 research and innovation program under grant agreement No 675731.

Acknowledgment

The authors would like to gratefully acknowledge the contribution of Dr. A.J.E.M. Janssen of TU Eindhoven, for his help with the analytical investigations of the function (A.3).

Appendix A. Initial conditions away from steady state

As mentioned in Section 3.4, for initial conditions far from the steady-state solution or simulating dynamics including abrupt changes in the input variables, the model-based modification (the fourth approach proposed in this paper) does not perform well. Due to the fact that equations in the DFM (6) are rather complicated, it is hard to find a framework for defining the applicability region of this method. Below, a brief explanation and an example are given for the case when the model-based modification cannot be applied.

Different from the results presented in the main text, here we analyze the algebraic constraints (34) in more detail and provide a qualitative insight why the algebraic constraints do not have a solution when the initial conditions for system (6) are far away from the steady-state solution. Similar analysis can be performed on the algebraic constraints (31).

To find the solution of the algebraic constraints, seven equations (three from (34) and four from closure laws of (2)-(5)) should be solved simultaneously to find the seven unknowns of primitive variables. Due to the nonlinearity of equations, these may have more than one solution or may not have any solution. This is investigated in this appendix by applying the following steps:

1. Since there are seven unknown variables in the equations, it is challenging to analyze the solutions. As a first step, we express the equations only in one variable, particularly in pressure.
2. The resulting single equation is a nonlinear function of pressure, which is hard to be analyzed. Therefore, the solution of that equation is investigated numerically.

Assume we aim to find the starred values $U^*_{M_1}$ from U_{M_1} by substituting (35a) and (35b) into (35c) and keeping pressure as the only variable. For reducing the number of variables and simplifying the equations, no slip between the phases, i.e., $\hat{u} := u_l = u_g$, is considered (it should be noted this is just an assumption for simplifying the computational procedure while the algebraic constraints of (34) are derived for general case of slip). Then, the simplified algebraic constraints of (35) change to:

$$(\alpha_l \rho_l \hat{u})^*_{M_1} = B, \tag{A.1a}$$

$$(\alpha_g \rho_g \hat{u})^*_{M_1} = C, \tag{A.1b}$$

$$\left(\alpha_l \frac{\rho_l}{\rho_g}\frac{\hat{u}^2}{2} + \alpha_g \frac{\hat{u}^2}{2} + c_g^2 \ln \rho_g\right)^*_{M_1} = D, \tag{A.1c}$$

with

$$B := \frac{(\alpha_l \rho_l \hat{u} A)_{M_1}}{A_{M_2}} \tag{A.2a}$$

$$C := \frac{(\alpha_g \rho_g \hat{u} A)_{M_1}}{A_{M_2}} \tag{A.2b}$$

$$D := \left(\alpha_l \frac{\rho_l}{\rho_g}\frac{\hat{u}^2}{2} + \alpha_g \frac{\hat{u}^2}{2} + c_g^2 \ln \rho_g\right)_{M_1}. \tag{A.2c}$$

By embedding (A.1a) and (A.1b) into (A.1c) and using the closure laws of (2)-(5) and keeping only pressure as the variable (denoting $p^*_{M_1}$ by p), a nonlinear function of pressure is obtained as follows:

$$\Phi(p) := \tfrac{1}{2}\varphi_1(p)\varphi_2^2(p) + c_g^2 \ln \tfrac{p}{c_g^2} - D, \tag{A.3}$$

where

$$\varphi_1(p) := \frac{\frac{p}{c_l^2}+F}{\frac{p}{c_g^2}} + \frac{C}{B}\left(\frac{p}{c_l^2}+F\right)\frac{1}{\frac{p}{c_g^2}+\frac{C}{B}\left(\frac{p}{c_l^2}+F\right)}\left(1-\frac{\frac{p}{c_l^2}+F}{\frac{p}{c_g^2}}\right), \tag{A.4a}$$

$$\varphi_2(p) := \frac{B\frac{p}{c_g^2}+C\left(\frac{p}{c_l^2}+F\right)}{\frac{p}{c_g^2}\left(\frac{p}{c_l^2}+F\right)}, \tag{A.4b}$$

with $F := \rho_0 - p_0/c_l^2$. Now, the solution of the algebraic constraints of (35) corresponds to the root of the function Φ in (A.3). Although function Φ is highly nonlinear and analytical investigation of the roots is challenging, analyzing the roots of the function Φ is easier compared to investigating the solution to the constraints (35). It can be shown that this equation either has one root, two roots or no root at all. Analytical investigation of the condition of having a root, however, is difficult, if not impossible. As the only variable in the function Φ is pressure, the roots can be found numerically by varying the pressure from zero to infinity and then we can analyze how many roots the function Φ has under different conditions.

This function tends to infinity as the pressure tends to zero or infinity when $B, C, D > 0$. In other words, for $p \to 0$ or $p \to \infty$, it holds that $\Phi \to \infty$. Thus, for Φ to have any real roots, the minimum of function Φ should be less than zero, which is highly dependent on the constant values of B, C, D, apparent from the dependence of the function on these constants. Hence, the necessary and sufficient condition for having solution(s) to the introduced algebraic constraints is $\Phi(p_{min}) < 0$ with $\Phi'(p_{min}) = 0$, where p_{min} is the unique value at which the minimum of Φ is attained. As mentioned previously, the analytical assessment of the roots of Φ is challenging, thus we tackle this numerically as follows with an example.

Consider the following test case as an example to show the fact that those algebraic constraints sometimes have multiple solutions and sometimes do not have any solution. If starting from the initial condition of shock tube problem presented in Section 4.2 accompanied with discontinuous area reduction at the middle cell of the pipe, say at the i-th cell, from $A_i = 1.5\ \mathrm{m}^2$ to $A_{i+1} = 1\ \mathrm{m}^2$, the evolution of function Φ with respect to p (as pressure varies from zero to infinity) for finding U_i^* and U_{i+1}^* values can be shown in Figure A.1.

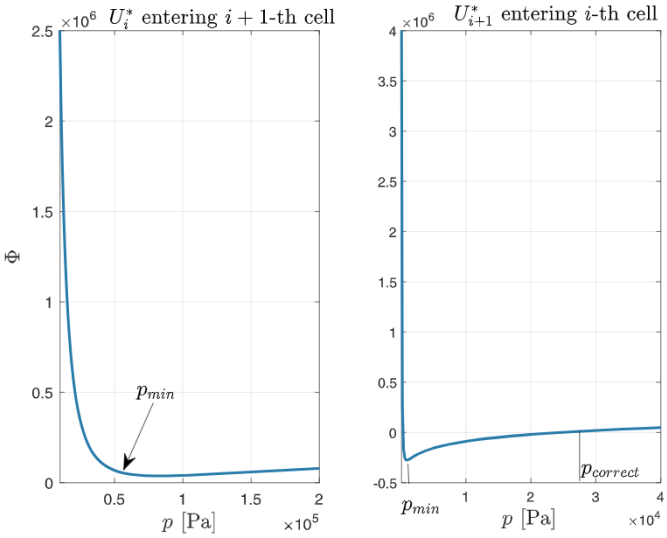

Figure A.1. Evolution of Φ function with pressure.

It can be noted that for finding the U_i^*, we do not have any solution, therefore the model-based modification fails to predict the solution (see the left plot in Figure A.1 that function Φ does not intersect the horizontal axis). In case of DFM, due to the complexity of the equations, it is hard to find a generic condition under which the constraint equations have solutions; unlike the case for Euler equations for which the condition is derived in [11]. However, a qualitative insight in the condition for the existence of a numerical solution can be provided as below. If we start exactly from steady-state solution, since the three algebraic constraints of (A.1) are defined by the steady-state equations, these equations are already satisfied. If starting close to steady states, the residuals of these equations are small and we are still in the region where the algebraic constraints can be satisfied by small changes in the primitive variables. In contrary, if we start from an initial condition far from steady-states, the residual of the algebraic constraints are large and it might be impossible to satisfy all seven equations simultaneously (in other words, $\Phi(p_{min}) > 0$ due to the values of B, C, D in (A.3)). Therefore, it is probable not to obtain solution if we start from inconsistent initial conditions, i.e., initial conditions far away from the steady-state solution. Analogous analyses can be carried out for abrupt dynamic changes in the simulation.

For U_{i+1}^*, we have two solutions (see right plot in Figure A.1). In case of having two solutions, one solution corresponds to the subsonic flow and the other to the supersonic flow. Following the same admissibility criterion of [11], a root which lies in the same side of p_{min} is chosen, meaning that

$$(p_{correct} - p_{min})(p_{i+1} - p_{min}) > 0 \tag{A.5}$$

where $p_{correct}$ is the correct root of function Φ that should be selected. Relying on this analysis, the second root should be selected in this simulation and the first root is ruled out.

Since in some cases, especially when the imposed assumptions (33) are not valid, we may not have the solutions of those algebraic relations, it is highly recommended to use the numerical method proposed in this paper when we start close to steady-state solution of the PDE. In industrial applications, it is often the case that system is simulated from steady states (or from rest) and the underlying dynamics are some perturbations to the steady-state solution. So, this is not a restrictive assumption in many cases. However, satisfying those algebraic relations to simulate the correct transient behavior comes at the expense of losing the solution in problems starting far from steady state. We leave further analysis of finding a better approach to future works. One tentative remedy could be a hybrid approach, combining the third and fourth approach proposed in this paper.

Appendix B. Reference solution for the transient simulation

As there is no Riemann solution for the DFM with variable cross-section, another method for having a reference solution for a transient case is used. In this method, at the location of area discontinuity, the pipe is divided into two different pipes that are connected to each other by some boundary conditions. For instance, the pipe in Figure 4 is broken into two different connected pipes, as shown in Figure B.2.

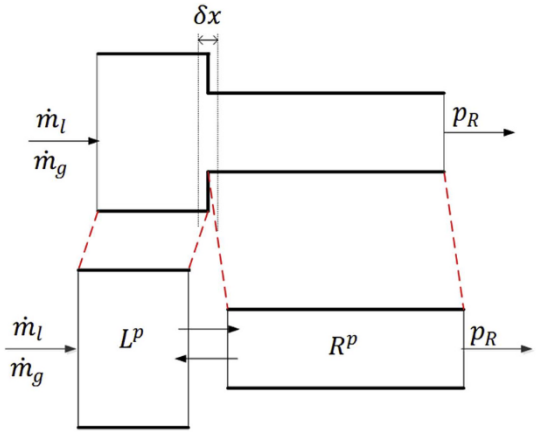

Figure B.2. Decomposition of pipes into many connected smaller pipes.

Within each smaller pipe, classical schemes with high resolution can be applied as each pipe has a constant area. At the interconnected boundary, at least six equations should be defined to obtain three primitive variables for each pipe. Then, by using the closure laws (2)-(5), all primitive variables can be obtained.

From the left pipe L^p, two characteristic-based boundary conditions corresponding to the waves moving downstream similar to (16) and (17) are written. From the right pipe R^p, one characteristic-based boundary condition moving upstream can be written similar to (18). Three more equations are required, which are obtained by integrating system (6) over the area discontinuity,

$$\int_{\delta x} \frac{\partial(\alpha_l \rho_l A)}{\partial t} dx + \int_{\delta x} \frac{\partial(\alpha_l \rho_l u_l A)}{\partial x} dx = 0, \tag{B.1a}$$

$$\int_{\delta x} \frac{\partial(\alpha_g \rho_g A)}{\partial t} dx + \int_{\delta x} \frac{\partial(\alpha_g \rho_g u_g A)}{\partial x} dx = 0, \tag{B.1b}$$

$$\int_{\delta x} \frac{\partial((\alpha_l \rho_l u_l + \alpha_g \rho_g u_g)A)}{\partial t} dx + \int_{\delta x} \frac{\partial((\alpha_l \rho_l u_l^2 + \alpha_g \rho_g u_g^2 + p)A)}{\partial x} dx = \int_{\delta x} p \frac{\partial A}{\partial x} dx, \tag{B.1c}$$

where δx is a very narrow band around each area discontinuity. For $\delta x \to 0$, the integrals related to the time derivations vanish and (B.1) simplifies to the following algebraic relations

$$(\alpha_l \rho_l u_l A)_{R^p} = (\alpha_l \rho_l u_l A)_{L^p}, \tag{B.2a}$$

$$(\alpha_g \rho_g u_g A)_{R^p} = (\alpha_g \rho_g u_g A)_{L^p}, \tag{B.2b}$$

$$\int_{\delta x} \left(\frac{\partial((\alpha_l \rho_l u_l^2 + \alpha_g \rho_g u_g^2)A)}{\partial x} + A \frac{\partial p}{\partial x} \right) dx = 0, \tag{B.2c}$$

where the subscript R^p and L^p refer to the right and left pipe. For no-slip condition $u_l = u_g = \hat{u}$, based on Lemma 1 and the algebraic equation (31c), we have

$$(\alpha_l \rho_l \hat{u} A)_{R^p} = (\alpha_l \rho_l \hat{u} A)_{L^p}, \tag{B.3a}$$

$$(\alpha_g \rho_g \hat{u} A)_{R^p} = (\alpha_g \rho_g \hat{u} A)_{L^p}, \tag{B.3b}$$

$$\left(\alpha_l \rho_l \hat{u} A \left(\frac{\hat{u}^2}{2} + c_l^2 \ln \rho_l \right) + \alpha_g \rho_g \hat{u} A \left(\frac{\hat{u}^2}{2} + c_g^2 \ln \rho_g \right) \right)_{R^p} = \left(\alpha_l \rho_l \hat{u} A \left(\frac{\hat{u}^2}{2} + c_l^2 \ln \rho_l \right) + \alpha_g \rho_g \hat{u} A \left(\frac{\hat{u}^2}{2} + c_g^2 \ln \rho_g \right) \right)_{L^p}. \tag{B.3c}$$

The other three equations have also been obtained. Then, the six boundary equations are complete and the simulation in each pipe can be solved with a high resolution Rusanov scheme to deliver the reference solution.

Appendix C. Supplementary data

Supplementary data related to this article can be found at https://doi.org/10.1016/j.petrol.2019.04.089.

References

Nikoofard, A., Aarsnes, U.J.F., Johansen, T.A., Kaasa, G.O., 2015. Estimation of states and parameters of a drift-flux model with unscented Kalman filter. IFAC Papers Online 48, 165–170.

Malekzadeh, R., Belfroid, S.P.C., Mudde, R.F., 2012. Transient drift flux modelling of severe slugging in pipeline-riser systems. International Journal of Multiphase Flow 46, 32–37.

Hammouda, N., Rao, Y.F., 2017. The effect of the advanced drift-flux model of ASSERT-PV on critical heat flux, flow and void distributions in CANDU bundle subchannels. Annals of Nuclear Energy 104, 197–213.

Flåtten, T., Munkejord, S.T., 2006. The approximate Riemann solver of Roe applied to a drift-flux two-phase flow model. ESAIM: Mathematical Modelling and Numerical Analysis 40, 735–764.

Evje, S., Fjelde, K.K., 2002. Hybrid flux-splitting schemes for a two-phase flow model. Journal of Computational Physics 175, 674–701.

Munkejord, S.T., 2006. Analysis of the two-fluid model and the drift-flux model for numerical calculation of two-phase flow, Ph.D. thesis, Norges Teknisk-Naturvitenskapelige Universitet. Fakultet for Ingeniørvitenskap og Teknologi.

IRIS, 2017. Test Wells - IRIS. http://www.iris.no/research/ullrigg/ullrigg-drilling-rig/test-wells, Accessed date: 28 January 2019.

Cuong, D.H., Thanh, M.D., 2015. A Godunov-type scheme for the isentropic model of a fluid flow in a nozzle with variable cross-section. Applied Mathematics and Computation 256, 602–629.

Evje, S., Fjelde, K.K., 2003. On a rough AUSM scheme for a one-dimensional two-phase model. Computers and Fluids 32, 1497–1530.

Varadarajan, P.A., Hammond, P.S., 2015. Numerical scheme for accurately capturing gas migration described by 1D multiphase drift flux model. International Journal of Multiphase Flow 73, 57–70.

Kröner, D., Thanh, M., 2005. Numerical solutions to compressible flows in a nozzle with variable cross-section. SIAM Journal on Numerical Analysis 43, 796–824.

Udegbunam, J.E., Fjelde, K.K., Evje, S., Nygaard, G., 2015. On the advection-upstream-splitting-method hybrid scheme: A simple transient-flow model for managed-pressure-drilling and underbalanced-drilling applications. SPE Drilling and Completion 30, 98–109.

Van Leer, B., 1977. Towards the ultimate conservative difference scheme III. upstream-centered finite-difference schemes for ideal compressible flow. Journal of Computational Physics 23, 263–275.

Clain, S., Rochette, D., 2009. First- and second-order finite volume methods for the one-dimensional nonconservative Euler system. Journal of Computational Physics 228, 8214–8248.

Helluy, P., Hérard, J.-M., Mathis, H., 2012. A well-balanced approximate Riemann solver for compressible flows in variable cross-section ducts. Journal of Computational and Applied Mathematics 236, 1976–1992.

de Carvalho, M.A.D., de Moraes Oliveira, G.F., Fernandes, L.D., Martins, A.L., Vega, M.P., 2019. Two-phase flow model validation during conventional / Pressurized Mud Cap Drilling (PMCD) scenarios. Journal of Petroleum Science and Engineering 172, 314–326.

Thanh, M.D., 2012. On a two-fluid model of two-phase compressible flows and its numerical approximation. Communications in Nonlinear Science and Numerical Simulation 17, 195–211.

Kurganov, A., Tadmor, E., 2000. New high-resolution central schemes for nonlinear conservation laws and convection–diffusion equations. Journal of Computational Physics 160, 241–282.

Liou, M.-S., Steffen, C.J., 1993. A New Flux Splitting Scheme. Journal of Computational Physics 107, 23–39 Bibtex: AUSM_original_euler.

Castro, M.J., Morales de Luna, T., Parés, C., 2017. Well-balanced schemes and path-conservative numerical methods. In: Abgrall, R., Shu, C.-W. (Eds.), Handbook of Numerical Analysis, volume 18 of *Handbook of numerical methods for hyperbolic problems*. Elsevier, pp. 131–175. https://doi.org/10.1016/bs.hna.2016.10.002.

Aarsnes, U.J.F., 2016. Modeling of two-phase flow for estimation and control of drilling operations, PhD thesis. Norges Teknisk Naturvitenskapelige Universitet.

Zuber, N., Findlay, J.A., 1965. Average volumetric concentration in two-phase flow systems. Journal of Heat Transfer 87, 453–468.

Isao, K., Mamoru, I., 1987. Drift flux model for large diameter pipe and new correlation for pool void fraction. International Journal of Heat and Mass Transfer 30, 1927–1939.

Holmes, J.A., 1977. Description of the Drift Flux Model in the Loca Code Relap-UK. In: Proceedings of the Conference on Heat and Fluid Flow in Water Reactor Safety. Institution of Mechanical Engineers paper C206/77, Manchester, UK, pp. 103–108.

Pompllio, R., 2014. Experimental analysis of air water two phase flow in vertical large pipes and development of drift flux models. Laurea magistrale / specialistica, Politecnico Di Milano, Italy.

Bhagwat, S.M., Ghajar, A.J., 2014. A flow pattern independent drift flux model based void fraction correlation for a wide range of gas–liquid two phase flow. International Journal of Multiphase Flow 59, 186–205.

Rommetveit, R., Vefring, E.H., 1991. Comparison of results from an advanced gas kick simulator With surface and downhole data from full scale gas kick experiments in an inclined well. Society of Petroleum Engineers.

Crouzet, F., Daude, F., Galon, P., Hérard, J.-M., Hurisse, O., Liu, Y., 2015. Validation of a two-fluid model on unsteady liquid–vapor water flows. Computers and Fluids 119, 131–142.

Wallis, G.B., 1656. One Dimensional Two-Phase Flow. Mcgraw-Hill.

Bansal, H., Schilders, W., van de Wouw, N., Iapichino, L., Koren, B., May 2017. Modified sound speed for the unification of single-phase and two-phase flow scenarios, NUMHYP17: Numerical methods for hyperbolic problems. Monte Verità.

da Silva Santim, C.G., Rosa, E.S., 2016. Roe-type Riemann solver for gas–liquid flows using drift-flux model with an approximate form of the jacobian matrix. International Journal for Numerical Methods in Fluids 80, 536–568.

Fjelde, K.K., Karlsen, K.H., 2002. High-resolution hybrid primitive–conservative upwind schemes for the drift flux model. Computers and Fluids 31, 335–367.

Baudin, M., Berthon, C., Coquel, F., Masson, R., Tran, Q.H., 2005. A relaxation method for two-phase flow models with hydrodynamic closure law. Numerische Mathematik 99, 411–440.

Singer, A., GIillespie, D., Norbury, J., Eisenberg, R.S., 2008. Singular perturbation analysis of the steady-state Poisson–Nernst–Planck system: Applications to ion channels. European Journal of Applied Mathematics 19, 541–569.

Smith, H.L., Waltman, P., 1999. Perturbation of a globally stable steady state. Proceedings of the American Mathematical Society 127, 447–453.

Shampine, L.F., Kierzenka, J., Reichelt, M.W., 2000. Solving boundary value problems for ordinary differential equations in matlab with bvp4c.

Paper C

A Well-Balanced Godunov-Type Scheme for the Euler Equations and the Drift Flux Model with Laminar Friction and Gravitation

Abbasi, Mohammad H., Sajad Naderi Lordejani, Christian Berg, Laura Iapichino and Nathan van de Wouw. "A Well-Balanced Godunov-Type Scheme for the Euler Equations and the Drift Flux Model with Laminar Friction and Gravitation"

Submitted to Journal of Computational Physics

Authors' role in the article: Ideas, implementation and critical review.

Manuscript submitted to Journal of Computational Physics. Not available in USN Open Archive.

Paper D

Pressure wave propagation in Managed Pressure Drilling- model comparison with real life data

Berg, Christian, Jon Åge Stakvik, Bernt Lie, Knut Vaagsaether, and Glenn-Ole Kaasa. "Pressure Wave Propagation in Managed Pressure Drilling- Model Comparison with Real Life Data," 60th SIMS conference, International Conference on Applied Energy (ICAE) 2019.

Authors' role in the article: Ideas, implementation and writing.

Pressure wave propagation in Managed Pressure Drilling- model comparison with real life data

Christian Berg[1,3] Jon Åge Stakvik[2,3] Bernt Lie[1] Knut Vaagsaether[1] Glenn-Ole Kaasa[3]

[1]Department of Electrical Engineering, IT and Cybernetics, University of South-Eastern Norway, Norway, Bernt.Lie@usn.no

[2]Department of Engineering Cybernetics , Norwegian University of Science and Technology, Norway

[3]Kelda Drilling Controls, Norway, cbe@kelda.no

Abstract

Drilling for oil and gas is a complex process, involving pumping of fluid through kilometers of pipes. Even though the drilling fluid has a high speed of sound ($\approx$1000 m/s), the large lengths involved make pressure wave propagation significant at timescales where such phenomena can usually be neglected in other processes. Managed pressure drilling, a technological extension of conventional drilling, adds a choke on the return flow from the drilling process. Significant work has been done in recent years on creating a simplified model of the process, often by neglecting distributed dynamics, and using this for controller design. This paper compares the simplified model most often used, with a distributed partial differential equation (PDE) model and compare the performance to measured data for wave propagation while doing managed pressure drilling. Fluid structure interaction and theoretical vs recorded speed of sound are discussed.

Keywords: Managed pressure drilling, PDE, wave propagation, FSI

1 Introduction

Managed pressure drilling (MPD), today considered an "unconventional" drilling technology, is a natural technological advancement of conventional drilling. MPD is forecasted to grow significantly in the future, with key industry players indicating that it might be the new "conventional" in the near future.

Drilling for oil and gas is a complex process with complex dynamic behaviour. The dynamics of the entire system has to be understood for controller and estimator design if the prognosed future growth and adoption is to be achieved.

For MPD, significant work has been done in recent years by control engineers/researchers on simplifying the mathematical model for the process to aid in controller and estimator design. A schematic view of the process is given in Figure 1. The most often used of these simplified models is the one by (Kaasa *et al.*, 2012). Multiple estimation and control strategies based on this simplified model has been published (Stakvik *et al.*, 2016), (Stakvik *et al.*, 2017), (Zhou *et al.*, 2011), (Stamnes *et al.*, 2008),

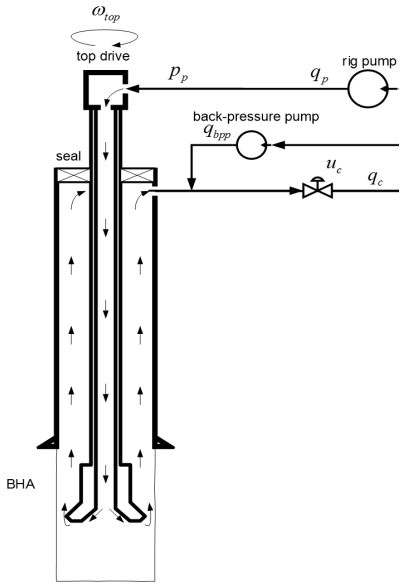

Figure 1. Managed pressure drilling. Drilling fluid is circulated from the rig mud pumps and down the drill string. At the bottom of the well bore the drilling fluid flows out through the drill bit via nozzles, and is then circulated up to the surface in the annular space between the drill string and annulus.

(Hauge *et al.*, 2012). There is also ongoing research on designing estimators and controllers based on a linearised PDE distributed model (Aarsnes *et al.*, 2014), (Aarsnes *et al.*, 2012), (Anfinsen and Aamo, 2018). To verify design, controllers and estimators should in general always be tested on a system model that is higher fidelity than the model the design is based on to ensure that something critically important was not forgotten in the simplification. This paper compares the response of the simplified model by (Kaasa *et al.*, 2012) with a PDE based model for the process, and compare this to real drilling data from MPD operations.

2 Model

Considering the process shown in Figure 1 and conservation of mass and momentum, dynamic models for the process can be derived. The model by (Kaasa *et al.*, 2012),

disregards distributed effects in the drill string and annulus, and consider these as two volumes where mass should be conserved. To capture wave propagation, distributed effects should be considered, making the drill-string and annulus take the form of partial differential equations (Di Meglio and Aarsnes, 2015).

2.1 Simplified model

The ODE model presented in (Kaasa *et al.*, 2012) and given in (1-5) can be derived with the following assumptions: The drill string and annulus are treated as two volumes where mass is conserved, the drill string pressure loss as quadratic with flow (turbulent), the drill bit pressure loss as quadratic with flow, and the annulus pressure loss as linear with flow (laminar). Note that here, the annulus and drill string volumes are considered constant, and in and out flow of the drilled formation is not considered.

$$\frac{V_d}{\beta_d}\frac{\mathrm{d}p_p}{\mathrm{d}t} = q_p - q_{bit} \tag{1}$$

$$\frac{V_a}{\beta_a}\frac{\mathrm{d}p_c}{\mathrm{d}t} = q_{bit} + q_{bpp} - q_c \tag{2}$$

$$M\frac{\mathrm{d}q_{bit}}{\mathrm{d}t} = p_p - p_c - F_d q_{bit}^2 - F_a q_{bit} \tag{3}$$

$$M = \int_0^{L_d} \frac{\rho_d}{A_d(x)}\mathrm{dx} + \int_{L_a}^{0} \frac{\rho_a}{A_a(x)}\mathrm{dx} \tag{4}$$

$$q_c = g_c(z_c)K_c\sqrt{\frac{2}{\rho}(p_c - p_{co})} \tag{5}$$

In (1-5) V_d and V_a are drill string and annulus volumes, β_d and β_a are fluid modulus of compressibility $\beta = \frac{1}{\rho}\frac{\mathrm{d}\rho}{\mathrm{d}p}$, q_p is the pump flow, q_{bit} is a state representing flow from the drill string to the annulus, F_d and F_a are friction factors for the drill string and annulus, g_c is choke area as a function of choke position z_c, ρ_a, ρ_d are fluid densities in drill string and annulus, and A_d, A_a are flow cross sectional areas.

2.2 PDE model

If distributed effects are considered, the drill string and annulus can be modelled using the PDE system given in (6-7) representing conservation of mass and momentum, respectively.

$$\frac{\partial\rho}{\partial t} + \frac{\partial\rho u}{\partial x} = 0 \tag{6}$$

$$\frac{\partial\rho u}{\partial t} + \frac{\partial(\rho u^2 + p)}{\partial x} = -f(\rho,u) - g(\rho) \tag{7}$$

where ρ is density and u is velocity.

Putting (6-7) in vector form as in (8) and introducing temporary variables u_1, u_2.

$$\frac{\partial \mathrm{U}}{\partial t} + \frac{\partial}{\partial x}(F(\mathrm{U})) = S(\mathrm{U}) \tag{8}$$

$$\begin{aligned}
\mathrm{U} &= \begin{bmatrix}\rho\\ \rho u\end{bmatrix} = \begin{bmatrix}u_1\\ u_2\end{bmatrix}\\
F(\mathrm{U}) &= \begin{bmatrix}\rho u\\ \rho u^2 + p\end{bmatrix} = \begin{bmatrix}u_2\\ \frac{u_2^2}{u_1} + \frac{\partial p}{\partial\rho}u_1\end{bmatrix}\\
S(\mathrm{U}) &= \begin{bmatrix}0\\ -f(\rho,u) - G(\rho,\theta)\end{bmatrix} = \begin{bmatrix}0\\ -f(u_1,\frac{u_2}{u_1}) - G(u_1,\theta)\end{bmatrix}
\end{aligned} \tag{9}$$

Where $\partial p = \frac{\partial p}{\partial\rho}\partial\rho$ is used for removing p in (9). Then in pseudo linear form as

$$\frac{\partial \mathrm{U}}{\partial t} + A(\mathrm{U})\frac{\partial \mathrm{U}}{\partial x} = S(\mathrm{U}) \tag{10}$$

$$A(\mathrm{U}) = \frac{\partial F(\mathrm{U})}{\partial \mathrm{U}} = \begin{bmatrix}0 & 1\\ -\frac{u_2^2}{u_1^2} + \frac{\partial p}{\partial\rho} & 2\frac{u_2}{u_1}\end{bmatrix} \tag{11}$$

it can be found that the eigenvalues of $A(\mathrm{U})$ are $\lambda_{1,2} = u \pm \sqrt{\frac{\partial p}{\partial\rho}}$ where $\sqrt{\frac{\partial p}{\partial\rho}}$ is the speed of sound in the fluid.

The source terms $f(\rho,u)$ and $G(\rho,\theta)$ represent friction and hydrostatic pressure due to gravity, respectively. Friction is modeled as (12)

$$\begin{aligned}
f(\rho,u) &= \frac{1}{2}K_{fric} f \rho u^2\\
f &= \max\left(\frac{64}{\mathrm{Re}}, \frac{0.25}{(\log(\frac{\varepsilon}{3.7D} + \frac{5.74}{\mathrm{Re}^{0.9}}))^2}\right)\\
\mathrm{Re} &= \frac{\rho u D}{\mu}
\end{aligned} \tag{12}$$

where f is the Darcy friction factor, Re is the Reynolds number, ε is the surface roughness of the pipe, and D is the hydraulic diameter. $f = \frac{64}{\mathrm{Re}}$ represents laminar flow, $f = \frac{0.25}{(\log(\frac{\varepsilon}{3.7D} + \frac{5.74}{\mathrm{Re}^{0.9}}))^2}$ is an approximation (Swamee and K. Jain, 1976) to the Colebrook equation, and the maximum of these two is taken to cover both laminar and turbulent regimes. K_{fric} is a tuning factor to fit measured field data, ideally set to 1.

Hydrostatic pressure is modelled as (13) where θ is the local angle between the well bore and the horizontal.

$$G(\rho,\theta) = \rho g \sin(\theta) \tag{13}$$

There are numerous numerical approaches to solving the PDE system in (6-7), (Vytvytsky and Lie, 2017), (Palacios G and Da Silva, 2013) both with and without considering fluid structure interaction. The details of different methods for solving (6-7) with strengths and weaknesses is not elaborated in detail in this paper. Here a staggered grid approach is used.

For simulation, (6) is transformed into an equation for pressure. Assuming the density can be given as a linear function of pressure as in (14), (6-7) can be rewritten as (15-16).

$$\rho = \rho_0 + \frac{\rho_0}{\beta}(p - p_0)$$
$$\frac{d\rho}{dp} = \frac{\rho_0}{\beta} \tag{14}$$

$$\frac{\rho_0}{\beta}\frac{\partial p}{\partial t} + \frac{\partial \rho u}{\partial x} = 0 \tag{15}$$

$$\frac{\partial \rho u}{\partial t} + \frac{\partial \rho u^2}{\partial x} = -\frac{\partial p}{\partial x} - f(\rho, u) - g(\rho) \tag{16}$$

The system in (15-16) is integrated over a closed volume as given in (17-20) along the lines described in (Versteeg and Malalasekera, 2019).

$$\oint_{CV} (\frac{\rho_0}{\beta}\frac{\partial p}{\partial t} + \frac{\partial \rho u}{\partial x}) dV = 0 \tag{17}$$

$$\oint_{CV} (\frac{\partial \rho u}{\partial t} + u\frac{\partial \rho u}{\partial x}) dV = \oint_{CV} (-\frac{\partial p}{\partial x} + S_x) dV \tag{18}$$

Applying the Gauss divergence theorem; $\oint_{CV} \text{div}(\phi u) dV = \oint_{S} \mathbf{n} \cdot (\phi u) dS$

$$\oint_{CV} (\frac{\rho_0}{\beta}\frac{\partial p}{\partial t}) dV + \int_{A} \mathbf{n} \cdot (\rho u) dA = 0 \tag{19}$$

$$\oint_{CV} (\frac{\partial \rho u}{\partial t}) dV + \int_{A} \mathbf{n} \cdot (\rho u^2) dA = \oint_{CV} (-\frac{\partial p}{\partial x} + S_x) dV \tag{20}$$

Solving the integrals and discretizing in space yield (21-22).

$$V\frac{\rho_0}{\beta}\frac{\partial p}{\partial t} + (uA\rho)_{out} - (uA\rho)_{in} = 0 \tag{21}$$

$$V\frac{\partial \rho u}{\partial t} + (u^2 A\rho)_{out} - (u^2 A\rho)_{in} = -V\frac{p_{out} - p_{in}}{L} + S_x V \tag{22}$$

Doing the variable change $q = uA$, applying the chain rule to $\frac{\partial \rho u}{\partial t}$, and using that $q\frac{\partial \rho}{\partial t} = q\frac{\rho_0}{\beta}\frac{\partial p}{\partial t}$ yield (23-24).

$$V\frac{\rho_0}{\beta}\frac{\partial p}{\partial t} + (q\rho)_{out} - (q\rho)_{in} = 0 \tag{23}$$

$$\frac{V}{A}(\rho\frac{\partial q}{\partial t} + q\frac{\rho_0}{\beta}\frac{\partial p}{\partial t}) + (\frac{q^2\rho}{A})_{out} - (\frac{q^2\rho}{A})_{in} \ldots$$
$$\ldots = -A(p_{out} - p_{in}) + S_x V \tag{24}$$

With boundary conditions

$$q_{ds}(x = 0) = q_p \tag{25}$$

$$p_{ds}(x = L) = p_{an}(x = L) + \frac{1}{K_{nozzle}}(\frac{q_{ds}(x = L)}{A_{nozzle}})^2 \tag{26}$$

$$\rho u A_{an}(x = L) = \rho u A_{ds}(x = L) \tag{27}$$

$$p_{an}(x = 0) = p_c \tag{28}$$

The system solved is given in (29-30) where the pressure equation is solved in the grid cell centre and the flow equation is solved on a grid that has the cell centre on the pressure grid face.

$$\frac{\partial p}{\partial t} = -\frac{\beta}{V\rho_0}((q\rho)_{out} - (q\rho)_{in}) \tag{29}$$

$$\frac{\partial q}{\partial t} = -q\frac{\rho_0}{\rho\beta}\frac{\partial p}{\partial t} - \frac{1}{\rho L}((\frac{q^2\rho}{A})_{out} - (\frac{q^2\rho}{A})_{in}) \ldots$$
$$-\frac{A}{\rho L}(p_{out} - p_{in}) + S_x\frac{A}{\rho} \tag{30}$$

The spatial arrangement of states can be seen for an example case with $n = 3$ grid elements for flow and $n+1$ grid elements for pressure in Figure 2. The subscript g in $p_{0,g}$ and $p_{n+1,g}$ is to represent that this is a "ghost node". Ghost nodes are grid elements outside of the physical domain used to implement boundary conditions.

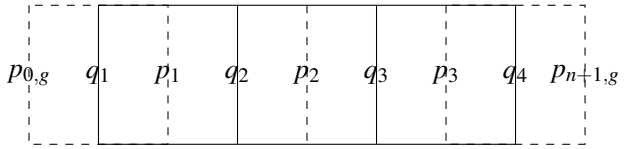

Figure 2. Staggered grid showing the spatial staggering of the system solved. If i represent grid number on the flow grid for q, and k represent grid number for the pressure grid for variables p and ρ, note that $i + \frac{1}{2} = k, k + \frac{1}{2} = i + 1$

From Figure 2 it can be seen that q_{out}, q_{in} (being q_2 and q_1 respectively for p_1) and p_{out}, p_{in}, (being p_1 and $p_{0,g}$ for q_1) is known directly due to the spatial staggering of states.

Variables that are not directly available on grid faces from the staggered arrangement (ρ in (29); q and $q\frac{\rho_0}{\beta}\frac{\partial p}{\partial t}$ in (30)) are found by using a first order up-winding in flow, as in (31)

$$\theta_{i+\frac{1}{2}} = \begin{cases} \theta_i & q > 0 \\ \theta_{i+1} & q < 0 \\ \frac{\theta_i + \theta_{i+1}}{2} & q = 0 \end{cases} \tag{31}$$

Equations (29-30) are solved in time by using a 4th order Runge Kutta method.

2.2.1 A brief discussion on equation of state

Using (14) as an Equation of State for the liquid will yield a speed of sound from the eigenvalue analysis in (10) as a function of ρ_0 and β given in (32)

$$c = \sqrt{\frac{\beta}{\rho_0}} \tag{32}$$

Drilling fluids are in most cases a mixture of water and weighting material (water based mud, WBM), oil, water and weighting material (oil based mud, OBM) or synthetic oil, water, and weighting material (Synthetic based mud, SBM). Drilling fluids usually also contain a small fraction of additives (emulsifiers, gelling agents, etc.), at a low volume fraction. The equivalent mixture bulk modulus should be found for use in (14) (Carcione and Poletto, 2000). Although all fluid components are only slightly compressible, the weighting material can be treated as incompressible compared to the water and oil. The volume fraction of additives are neglected here.

The mixture bulk modulus β_m can be found as in (33) where subscripts w, o, s denote water, oil and solids respectively.

$$\frac{1}{\beta_m} = \frac{\alpha_w}{\beta_w} + \frac{\alpha_o}{\beta_o} + \frac{\alpha_s}{\beta_s} \tag{33}$$

Here α_i is the volume fraction of that mixture component. Note that $\alpha_w + \alpha_o + \alpha_s = 1$. Assuming the solids component to be incompressible as $\beta_s >> \beta_o, \beta_w$, analogous to saying $\beta_s = \infty$ makes the last term on the RHS of (33) disappear.

The mixture density ρ_{m0} can be found as (34)

$$\rho_{m0} = \alpha_w \rho_{w0} + \alpha_o \rho_{o0} + \alpha_s \rho_{s0} \tag{34}$$

In practice, a pre-defined ratio of oil/water is used when mixing the drilling fluid, and then weighting solids is added to reach the desired liquid density. For WBM fluids there is no oil fraction, and solids are added to reach the desired density. This can be used to further simplify (33-34). By using oil-water ratio, $R_{ow} = \frac{\alpha_o}{\alpha_w}$, and the fact that the sum of all the component volume fractions is 1, (33-34) can be rewritten in forms that are simple for straight forward use, as given in (35-36) where the inputs are the mixture and component densities ρ_m, ρ_i, component compressibility β_i, and oil-water ratio R_{ow}.

$$\alpha_s = \frac{\rho_m - \rho_w + R_{ow}(\rho_m - \rho_o)}{\rho_s - \rho_w + R_{ow}(\rho_s - \rho_o)} \tag{35}$$

$$\beta_m = \frac{\beta_w \beta_o (1 + R_{ow})}{\beta_o (1 - \alpha_s) + R_{ow} \beta_w (1 - \alpha_s)} \tag{36}$$

For water based mud, $R_{ow} = 0$ and (35-36) are still valid. Equations (35-36) are only valid at a given pressure as the volume fractions change with pressure. In practice the effect of this is minor.

2.2.2 Fluid structure interactions (FSI)

If fluid structure interactions are considered, i.e., the flow cross sectional area changes with pressure, an equivalent bulk modulus β_e can be calculated and used in (23, 24). Note that the mixture bulk modulus β_m should still be used in the liquid Equation of State in (14).

Taking pipe expansion into account, equivalent bulk modulus can be calculated as (37). Here the possible compression of the drill string inside the annulus is neglected. For the full derivation of (37) in the context of the applied PDE, the reader is referred to (Carlsson, 2016).

$$\beta_e = \frac{\beta_m}{(1 + \frac{\beta_m D}{dE}\phi)} \tag{37}$$

In (37), β_m is mixture bulk modulus from (36), E is Young's modulus of the pipe, D is the pipe diameter, d is the pipe wall thickness, and ϕ is the pipe support factor. Here axial stresses are neglected, setting $\phi = 1$.

2.2.3 Gridding

In a real well geometry there are numerous changes in cross sectional area with axial position, mainly caused by the drill string consisting of different pipe sections screwed together. Spatial discretization (gridding) at the resolution required to capture all the changes exactly will require a large number of grid elements. Here, a gridding routine that ensures the grid volume and volume of the real geometry are exactly equal, is used. The real vs discretized geometry for the test well studied near the bottom hole assembly (BHA) is shown in Figure 3.

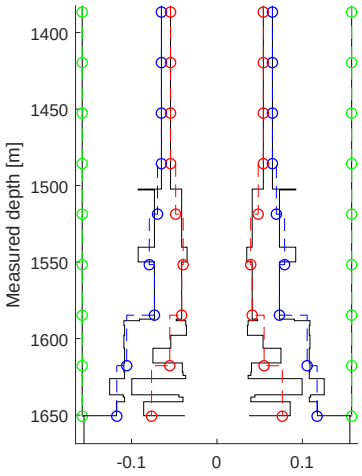

Figure 3. Volume conserving grid of bottom hole assembly (BHA). Solid black: Original geometry. Dashed green: Gridded well bore diameter (annulus). Dashed blue: Gridded drill string outer diameter (annulus). Dashed red: Gridded drill string inner diameter (drill string).

2.2.4 Boundary conditions

For comparison with field data, the algebraic relation between choke flow and choke pressure for the simplified model is skipped, and measured choke pressure is used directly as a boundary condition. This yields a simplified model with two ODE's, (as opposed to the three ODE's in the original model by (Kaasa *et al.*, 2012)) specified in (1, 3, 4). To compare the model's dynamic response to the measured data, the boundary values that are not specified are compared to measured data. That is, measured pump flow and choke pressure are used as boundary conditions.

Then, simulated and measured pump pressure and choke flow are compared. The simplified model has no choke flow when the choke pressure is specified, so only pump pressure is compared to measured pump pressure.

For the PDE model the boundary conditions for n grid elements are set as follows.

- Inlet
  - $p_0 = p_1$. That is, the inlet ghost node for pressure is set to the same value as the next grid element
  - $q_1 = q_{bc}$, the flow into the domain is specified
- Outlet
  - p_{n+1}, the outlet ghost node for pressure is set to $2p_{bc} - p_n$ where p_{bc} is the specified boundary pressure

2.3 Initial conditions

For the PDE model the initial conditions is set to the hydrostatic pressure for p, that is $p_i = \rho_0 g h_i$ where h_i is the grid vertical depth. The initial condition for flow q is set to zero. Flow is then ramped up to the flow rate in the start of case considered and simulation run for 150 seconds to reach steady state.

3 Comparison with field data

In MPD operations, if the choke controller is active, wave propagation phenomena are rarely visible. This is due to the choke pressure controller being used in the data the author has available is specifically designed to keep within the limits of the simplified model. During system commissioning, direct choke position control is used to verify calibration of the controller model, and pressure wave dynamics gets excited. When doing choke position control, the rate of change of the position is limited in the controller to about $\approx 5\%/\text{s}$ to avoid severe water hammer effects caused by the operator, but still fast enough that wave dynamics is excited. The controller in closed loop has access to the full choke actuator performance $\approx 25\%/\text{s}$, making the testing of the mentioned controller on a PDE model very important as it is easily able to excite wave dynamics in cases with improper tuning. For validation of the models with data, a time period from commissioning on a 1647m deep offshore well is used, as seen in Figure 4. The commissioning is performed in "cased hole", that is, the annulus has a steel casing going all the way to the bottom of the well and there is no "open hole" (exposed reservoir) .

In Figure 4, the pump flow rate is near constant, and the choke is closed and then opened again 3 times at various speeds, giving an increase in choke pressure (boundary condition), and then an increase in pump pressure (modelled), governed by the pressure dynamics of the well. The choke flow changes when the choke position is changed.

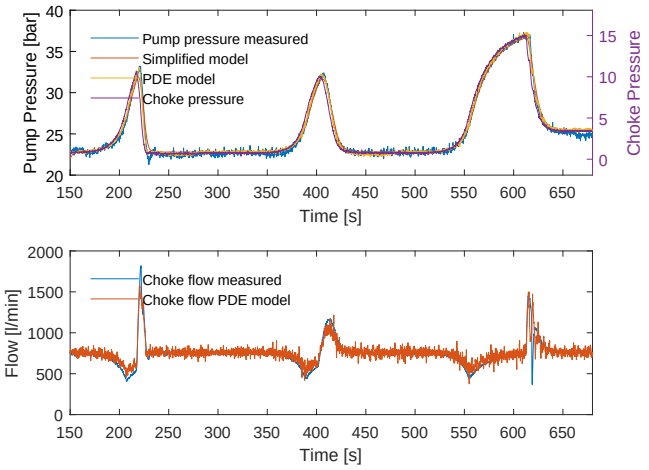

Figure 4. Steps in choke position during cased hole commissioning for 1647m deep offshore well. Top: Pressure simulated vs measured. Top right axis: Measured choke pressure (boundary condition). Bottom: Simulated vs measured choke flow.

This is caused by the compression/expansion of liquid and possible expansion of well geometry due to pressure.

3.1 Field data comparison, no fluid structure interactions

Here the response to the choke position steps are studied for all steps individually. Fluid structure interactions are not considered. Parameters used in the PDE and simplified model are given in Table 1. A "fudge factor" K_{fric} for friction in the PDE model was required to make the simulated pump pressure fit with the measured data. At the flow rates in the cases studied, the frictional pressure loss will be laminar in both the drill string and annulus. The assumption of Newtonian fluid in (12) is not really true for drilling fluids as they exhibit gelling behavior, something that will lead to a higher friction loss than for Newtonian fluids at low flow rates.

The noise on the pump pressure and choke flow in the PDE model is caused by noise on the choke pressure boundary condition. Filtering the noise on the signal is avoided as the phenomena studied are fast compared to the sampling rate. Figure 5 shows a close-up of the first step from Figure 4.

It is seen from Figure 5 that, qualitatively, the results of the PDE model fits reasonably well with the measured data. The PDE model under-predicts the changes of choke flow due to choke pressure. The response on pump pressure happens faster in the PDE model than in the measured data. This indicates that the wave propagation time in the PDE model is faster than in reality. The simplified model is able to predict pump pressure well when the pressure is increasing, but ends up giving a "smoothed" response on the more rapid opening of the choke.

Figure 6 shows the response in the second step, where both the increase and decrease of choke pressure is slower than that in the first step. It is clearly seen that as changes happen more slowly, the difference between the simplified

Table 1. Model parameters.

Parameter	Value	Unit
V_d	15.27	$[m^3]$
V_a	104.94	$[m^3]$
R_{ow}	4	$[-]$
$\rho_{m0} = \rho_d = \rho_a$	1210	$[kg/m^3]$
ρ_{w0}	1000	$[kg/m^3]$
ρ_{o0}	850	$[kg/m^3]$
ρ_{s0}	4200	$[kg/m^3]$
β_w	2.2e9	[Pa]
β_o	1.5e9	[Pa]
β_a (eq.36)	1.78e9	[Pa]
β_d (eq.36)	1.78e9	[Pa]
L_d	1651	[m]
L_a	1651	[m]
A_d	0.0092	$[m^2]$
A_a	0.0636	$[m^2]$
M (eq.4)	2.47e8	$[kg/m^4]$
μ	45e-3	$[Pa \cdot s]$
ε	4.5e-5	[m]
K_{fric}	2.4	$[-]$
A_{nozzle}	6.25e-04	$[m^2]$
K_{nozzle}	0.8	$[-]$

model, PDE model, and measured data becomes smaller. This is reasonable as that the main difference between the simplified and PDE model is whether distributed pressure effects are neglected. The effect of choke pressure on choke flow in the PDE model is still under-predicted, as in the first pressure step.

Figure 7 shows the response of the simplified and PDE model compared to field data for the third pressure step. In this step, the opening of the choke is even faster than that of the case in Figure 5. Note the "wave" in measured choke pressure. As for the two first cases, the results of the PDE and simplified model compared to field data is very similar at the increase of pressure with different response on opening the choke quickly. The previous observation of choke flow being under-predicted in the PDE model is visible when the pressure is increased, but not that clearly visible when the choke is opened.

3.2 Field data comparison, fluid structure interactions

Here the steps in the previous section is revisited, with fluid structure interactions (FSI) considered. Parameters used when FSI is considered are given in Table 2.

Figure 8 shows the PDE model with and without FSI in the first step. Considering FSI through (37), yields a lower β for the drill string and annulus, something that will increase the wave propagation time (decrease velocity) in the PDE model, as well as make the effect of choke pressure on choke flow be more significant. The assumption of no axial stresses used is not strictly true. For the annulus, the casing will mainly be under compression loads axially.

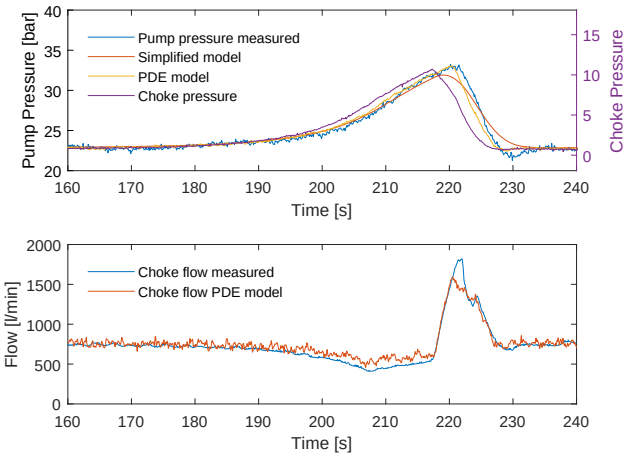

Figure 5. First step in choke position; slow closing and rapid opening of choke. Top: Pressure simulated vs measured. Top right axis: Measured choke pressure (boundary condition). Bottom: Simulated vs measured choke flow.

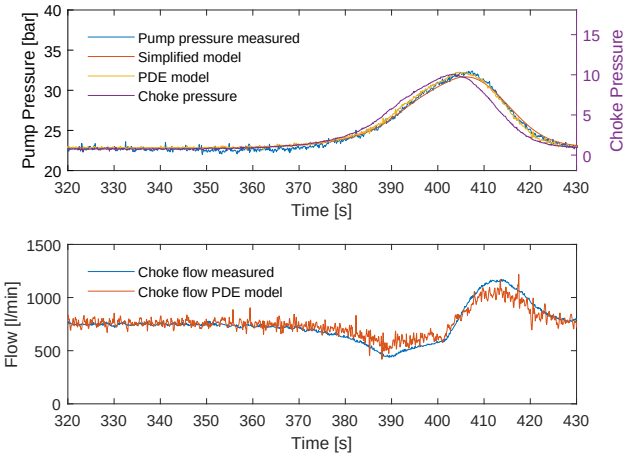

Figure 6. Second step in choke position; slow closing and opening of choke. Top: Pressure simulated vs measured. Top right axis: Measured choke pressure (boundary condition). Bottom: Simulated vs measured choke flow.

The neglected effect of compression of the drill string in the annulus together with the axial forces in the casing would likely lead to slightly lower effective bulk modulus. The drill string experiences both stretch and compression along the length.

As seen in Figure 8, the effect of choke pressure on flow becomes more significant when considering FSI, making the PDE model fit the measured flow data better compared to the model neglecting FSI. Wave propagation time reduces slightly when considering FSI, but there is still a mismatch between the PDE model and recorded data.

Figure 9 shows the PDE model compared to measured data for the second step in pressure, with and without FSI. Overall the results for the second pressure step are similar to the no FSI case, with the transient being slow enough that wave propagation effects are minor. The effect of choke pressure on choke flow compared to measured data is better when considering FSI than not considering FSI,

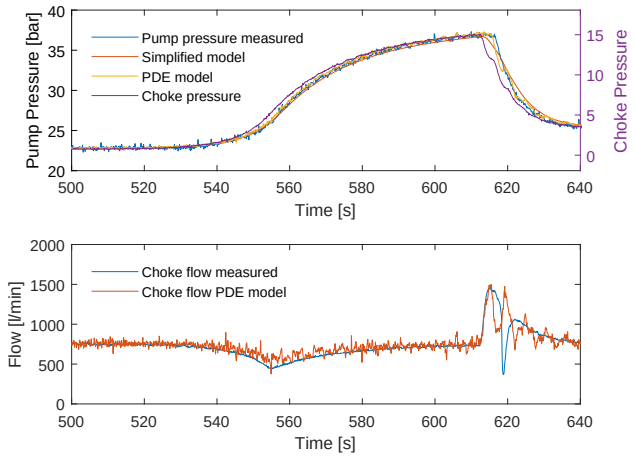

Figure 7. Third step in choke position; slow closing and very rapid opening of choke. Top: Pressure simulated vs measured. Top right axis: Measured choke pressure (boundary condition). Bottom: Simulated vs measured choke flow.

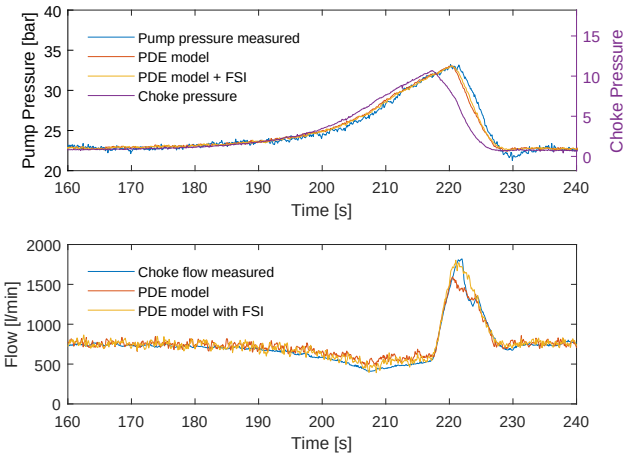

Figure 8. First step in choke position, comparison of original PDE-simulation and PDE-simulation considering fluid structure interactions. Top right axis: Measured choke pressure (boundary condition). Bottom: Simulated vs measured choke flow.

Table 2. Model parameters with FSI considered.

Parameter	Value	Unit
β_m (eq.36)	1.78e9	[Pa]
E	200e9	[Pa]
D_d	0.1086	[m]
d_d	0.0076	[m]
D_a	0.3153	[m]
d_a	0.0122	[m]
$\beta_{e,d}$ (eq.37)	1.57e9	[Pa]
$\beta_{e,a}$ (eq.37)	1.45e9	[Pa]

but the results of the PDE model still suggest that the used β_e is slightly too big, illustrated by compression and expansion (flow change due to pressure) being smaller in the PDE model considering FSI than recorded flow data.

Figure 10 shows the PDE model compared to measured data for the third step in pressure, with and without FSI. For the third pressure step, the effect of considering FSI is smaller than in the case of the first two steps. The simulation with FSI show a slightly larger change in choke flow from changing choke pressure, as is the case for the first two steps as well as a slightly increased wave propagation time. The deviation between simulated flow and measured flow when the pressure is reduced might be caused by sensor inaccuracies. The dynamic performance of the Coriolis flow meter at transients as fast as in Figure 10, is uncertain.

4 Conclusions

The response of the commonly used simplified model by (Kaasa *et al.*, 2012) and a distributed PDE based model has been compared to data from cased hole commissioning from an MPD system on an offshore well. It is shown that when changes are slow, the simplified and PDE based models show very similar response, matching quite closely that of the measured data. When the transient

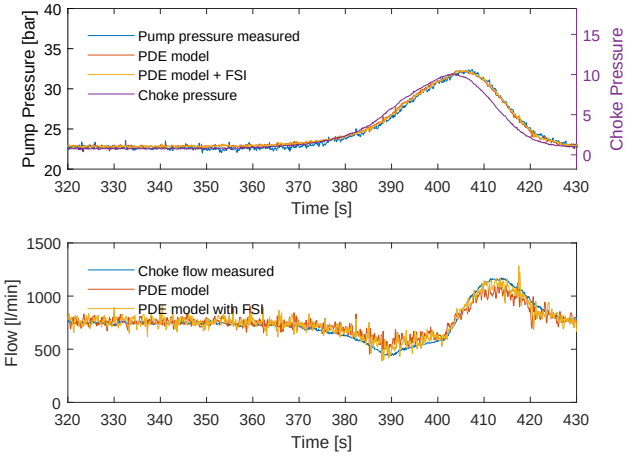

Figure 9. Second step in choke position. Slow closing and opening of choke, comparison of original PDE simulation and PDE simulation considering fluid structure interactions. Top right axis: Measured choke pressure (boundary condition). Bottom: Simulated vs measured choke flow.

changes are more rapid, a discrepancy between the simplified model and PDE model and measured data is seen. It is found that the PDE model under-predicts the effect of choke pressure on choke flow if only fluid properties are considered. When considering simple fluid structure interactions, the PDE model more closely fits the measured data. A discrepancy between the wave propagation time in the PDE model and measured data is observed. By manually "fudging" the system bulk modulus β_e, it is still not possible to make the PDE model fit with both choke flow and pump pressure (wave propagation time). To make the PDE model more closely fit the measured data, the well length or well volume and bulk modulus has to be changed. Well length and volume are considered quite well known, such that this result is indicative of something more fundamental missing from the PDE based model. The PDE model disregards 2-D effects on

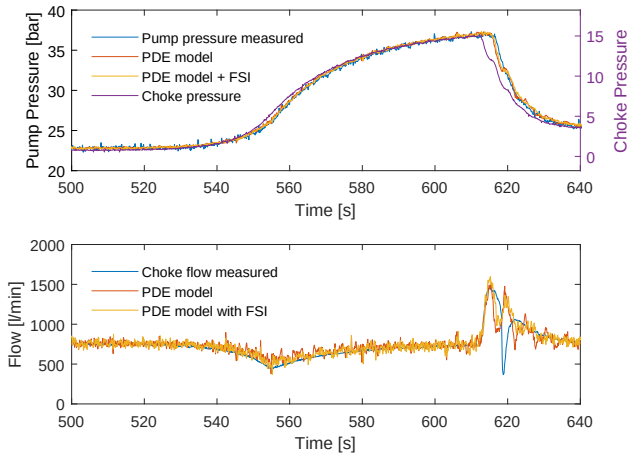

Figure 10. Third step in choke position. Very rapid opening of choke, comparison of original PDE simulation and PDE simulation considering fluid structure interactions. Top right axis: Measured choke pressure (boundary condition). Bottom: Simulated vs measured choke flow.

wave propagation, something that can increase the wave communication time. Further study of the discrepancy between the wave communication time in the 1D PDE model and recorded data, something that has been found in data from multiple wells, will require further work.

5 Acknowledgements

We thank Liobomyr Vytvysky on useful discussions on FSI in 1-D in compressible PDE models. This research has been partially funded by the the Norwegian Research Council in the Industrial PhD project "Modeling for automatic control and estimation of influx and loss in drilling operations" Project no 241586.

References

Ulf Jakob F Aarsnes, Ole Morten Aamo, and Alexey Pavlov. Quantifying error introduced by finite order discretization of a hydraulic well model. In *Control Conference (AUCC), 2012 2nd Australian*, pages 54–59, Aarsnes2012, 2012. IEEE. ISBN 1-922107-63-8.

Ulf Jakob Flø Aarsnes, Martin Standal Gleditsch, Ole Morten Aamo, and Alexey Pavlov. Modeling and Avoidance of Heave-Induced Resonances in Offshore Drilling. *SPE Drilling & Completion*, 29(04):454–464, December 2014. doi:10.2118/173178-PA.

Henrik Anfinsen and Ole Morten Aamo. Adaptive Output-Feedback Stabilization of 2 x 2 Linear Hyperbolic PDEs with Actuator and Sensor Delay. In *2018 26th Mediterranean Conference on Control and Automation (MED)*, pages 1–6, Zadar, June 2018. IEEE. ISBN 978-1-5386-7890-9. doi:10.1109/MED.2018.8442627.

José M Carcione and Flavio Poletto. Sound velocity of drilling mud saturated with reservoir gas. *Geophysics*, 65(2): 646–651, 2000. ISSN 0016-8033.

Joel Carlsson. Water Hammer Phenomenon Analysis using the Method of Characteristics and Direct Measurements using a "stripped" Electromagnetic Flow Meter. Master Thesis, 2016.

Florent Di Meglio and Ulf Jakob Flø Aarsnes. A distributed parameter systems view of control problems in drilling. *IFAC-PapersOnLine*, 48(6):272–278, 2015.

Espen Hauge, Ole Morten Aamo, and John-Morten Godhavn. Model-based estimation and control of in/out-flux during drilling. In *American Control Conference (ACC), 2012*, pages 4909–4914, Hauge2012mbe, 2012. IEEE. ISBN 1-4577-1095-1.

Glenn-Ole Kaasa, Øyvind N Stamnes, Ole Morten Aamo, and Lars S Imsland. Simplified hydraulics model used for intelligent estimation of downhole pressure for a managed-pressure-drilling control system. *SPE Drilling & Completion*, 27(01):127–138, 2012. ISSN 1064-6671. doi:10.2118/143097-PA.

Erika Palacios G and Carlos Da Silva. A finite volume study for pressure waves propagation in a straight section of pipeline with caviation. *The International Journal of Multiphysics*, 7(4):259–270, December 2013. ISSN 1750-9548. doi:10.1260/1750-9548.7.4.259.

Jon Åge Stakvik, Christian Berg, Glenn-Ole Kaasa, Ole Morten Aamo, and Urs Lehner. Adaptive Model Based Choke Control System for MPD Operations. In *SPE-179714-MS*, SPE, April 2016. Society of Petroleum Engineers. ISBN 978-1-61399-446-7. doi:10.2118/179714-MS.

Jon Åge Stakvik, Christian Berg, Glenn-Ole Kaasa, Robert Graham, and Antonio Torrealba. Model-Based Control in Managed Pressure Drilling. In *SPE/IADC Drilling Conference and Exhibition*. Society of Petroleum Engineers, 2017. ISBN 1-61399-501-6.

Øyvind Nistad Stamnes, Jing Zhou, Glenn-Ole Kaasa, and Ole Morten Aamo. Adaptive observer design for the bottomhole pressure of a managed pressure drilling system. In *Decision and Control, 2008. CDC 2008. 47th IEEE Conference On*, pages 2961–2966. IEEE, 2008. ISBN 1-4244-3123-9. doi:10.1109/CDC.2008.4738845.

Prabhata Swamee and Akalank K. Jain. Explicit equations for pipe-flow problems. *ASCE J Hydraul Div*, 102:657–664, May 1976.

Henk Versteeg and W Malalasekera. *An Introduction to Computational Fluid Dynamics : The Finite Volume Method / H. K. Versteeg and W. Malalasekera.* April 2019.

Liubomyr Vytvytsky and Bernt Lie. Comparison of elastic vs. inelastic penstock model using OpenModelica. In *The 58th Conference on Simulation and Modelling (SIMS 58) Reykjavik, Iceland, September 25th – 27th, 2017*, pages 20–28, September 2017. doi:10.3384/ecp1713820.

Jing Zhou, Ole Morten Aamo, and Glenn-Ole Kaasa. Switched control for pressure regulation and kick attenuation in a managed pressure drilling system. *Control Systems Technology, IEEE Transactions on*, 19(2):337–350, 2011. ISSN 1063-6536.

Paper E

The Influx Management Envelope Considering Real Fluid Behaviour

Berg, Christian, Naveen Velmurugan, Geir-Arne Evjen, and Martin Culen. "The Influx Management Envelope Considering Real Fluid Behaviour," SPE Drilling & Completion, Society of Petroleum Engineers, 2019.

Authors' role in the article: Ideas, implementation and writing.

Paper F

Cascaded Bottom Hole Pressure Control in Managed Pressure Drilling

Stakvik, Jon Age, Christian Berg, Glenn-Ole Kaasa, and Ole Morten Aamo. "Cascaded Bottom Hole Pressure Control in Managed Pressure Drilling." In 2017 IEEE Conference on Control Technology and Applications (CCTA), 2001–7. Mauna Lani Resort, HI, USA: IEEE, 2017. https://doi.org/10.1109/CCTA.2017.8062748.

Authors' role in the article: Ideas, implementation, system set up and operation in the field and writing/critical review.

Cascaded Bottom Hole Pressure Control in Managed Pressure Drilling*

Jon Åge Stakvik[1], Christian Berg[2], Glenn-Ole Kaasa[3] and Ole Morten Aamo[4]

***Abstract*— Today, in search of oil resources, marginal wells with narrow pressure windows are frequently being drilled. This requires accurate and precise control to balance the bottom hole pressure (BHP) between the pore and fracture pressure of the reservoir. Managed pressure drilling (MPD) is a technique introduced to enable improved pressure control when drilling. This paper presents a cascaded control structure for BHP, choke pressure and choke position in MPD operations. Estimators for the unknown bottom hole flow and uncertain BHP are developed to improve pressure control performance. The presented method is evaluated with field operation data from drilling two 4000 m deep wells. The results show that the pressure is maintained within acceptable margins through a series of operations.**

I. INTRODUCTION

One of the critical tasks in drilling is to control the bottom hole pressure (BHP). Drilling fluid, commonly referred to as "drilling mud", is pumped at high pressure from the mud pit down the drill string, through the drill bit and up the annulus while it carries cuttings to the surface, as illustrated in Fig. 1. At the surface the mud is separated from the cuttings by a shaker. Besides transporting cuttings to the surface the drilling mud maintains the pressure in the annulus at a desired level. In particular, it must be maintained above the formation pore pressure to prevent unwanted influx of hydrocarbons into the well. Furthermore, if the pressure becomes too low the well might collapse. On the other hand, if the pressure in the drilling mud exceeds the strength of the surrounding rock formation it can lead to fractures in the open hole section of the well. Consequently, it is necessary to maintain the pressure within the window which is specified by geophysical data. Imprecise pressure control leads to incidents that are time-consuming, expensive and dangerous, such as loss of mud, influx of formation fluid or, in the worst case, blowouts.

In conventional drilling operations the BHP is typically controlled by a constant mud weight during a section. The mud weight is designed to be as low as possible, i.e. some margin above the highest expected pore pressure in the section to be drilled. The section length is typically ended when the BHP gets too close to the weakest expected formation strength. For decades, this approach has extensively been used and is still the most common drilling method in wells with large pressure windows. However, conventional pressure control yields slow (hours) and inaccurate control which is not suitable for more demanding wells with narrow pressure windows and/or high frictional pressure losses.

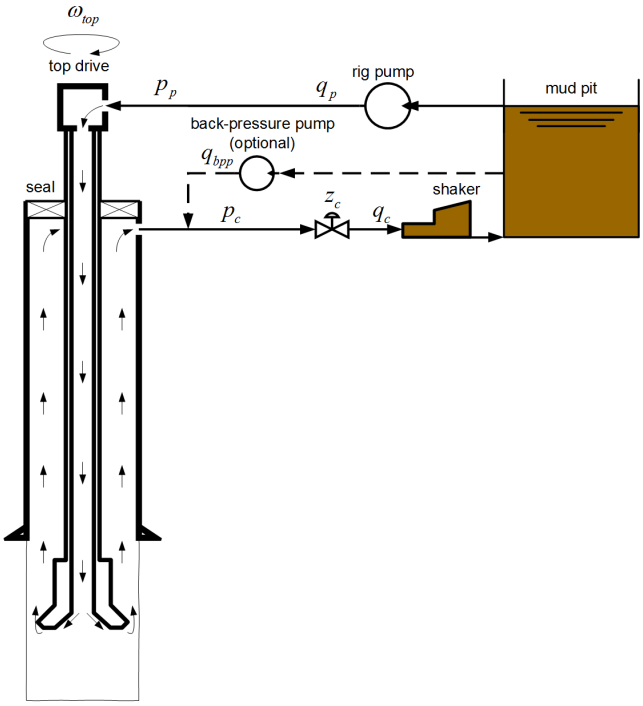

Fig. 1. Well configuration of a managed pressure drilling system. The drilling mud is injected by the rig pump while the outflow is controlled by a choke valve.

Today, marginal wells with narrow pressure windows are frequently being drilled. Managed pressure drilling (MPD) is a method that enables improved pressure control in wells with narrow pressure windows and varying formation pressures. In MPD, the annulus is sealed from the atmosphere by a rotating control device (RCD) and the annular flow is routed through a choke manifold where the upstream pressure is controlled by a choke valve. This enables fast and precise control of the annular pressure and, in contrast to conventional drilling, the pressure can be changed in matter of seconds. Additionally, MPD offers the possibility to drill longer sections than conventional drilling due to improved controllability of BHP.

MPD can be performed with manual operation of the

*This work was supported by the Norwegian Research Council (project no. 241636) through the Industrial PhD project.

[1]Jon Åge Stakvik is with Kelda Drilling Controls AS, Porsgrunn, Norway and is an industrial PhD candidate at the Norwegian University of Science and Technology (NTNU), Trondheim, Norway. jas@kelda.no

[2]Christian Berg is with Kelda Drilling Controls AS, Porsgrunn, Norway and is an industrial PhD candidate at the University College of Southeast Norway (HSN), Porsgrunn, Norway. cbe@kelda.no

[3]Glenn-Ole Kaasa is with Kelda Drilling Controls AS, Porsgrunn, Norway. gok@kelda.no

[4]Ole Morten Aamo is with the Institute of Engineering Cybernetics, Norwegian University of Science and Technology (NTNU), Trondheim, Norway. ole.morten.aamo@ntnu.no

choke opening, or automatic, where the choke position is modified by a control law. An automated MPD approach provides a higher accuracy than manual control. A critical drilling operation that must be handled by any automated MPD system is the connection. A connection is performed for every 27-29 m of drilling where the mud pumps are stopped to connect a new pipe segment to the top of the drill string. This operation introduces significant flow variations in the well where the BHP needs to be maintained within a given drilling window. The essential difficulty in connections is that no flow enters the annulus, and thus the pressure can only be maintained at the current level or reduced, but not increased. Optionally, a back-pressure pump can be installed, as illustrated in Fig. 1, which adds controllability when the rig pumps are shut down. However, several leading MPD suppliers have lately developed systems that do not require back-pressure pumps, for instance Schlumberger [1] and Weatherford [2], which offers a reduced footprint on the rig and less complex operational procedures. This paper presents results of a MPD operation performed without a back-pressure pump, and the scope is restricted to set-point changes and connections.

A number of papers have discussed control and estimation for MPD applications. Adaptive observer designs for the flow and pressure at the drill bit can be found in [3], [4] and a field experiment confirms these findings in [5]. An extensive review of control requirements for MPD is available in [6], and it specifies how an automated MPD system should act in normal and failure operations. In addition, [6] outlines results of drilling with MPD in a high-pressure high-temperature (HPHT) well in the Kvitebjørn field. More recently, a nonlinear control structure was developed and tested in a full scale drilling test rig [7] and shows satisfying results in set-point changes and connection operations. The development of a commercially available MPD system is presented in [8], where several important aspects regarding practical implementation are discussed, including the necessity of feedforward, and thus model-based control, to enhance performance.

This paper presents field results of a newly developed model-based industrial MPD system for cascaded control of the BHP. The development of the system has consisted of several years of focused research and testing and is now ready for industrial use. The paper is organized as follows; Section II presents a system overview of the well model and the cascaded control structure. Section III demonstrates the performance of the control solution with the necessary estimators. Section IV summarizes the conclusions of the paper.

II. Control Structure

Today, the hardware setup in MPD is typically very similar for most operations and consists of an RCD, which seals the annulus from the atmosphere, and a controllable choke manifold, as illustrated in Fig. 1. Several variations of MPD exist with the most common method being constant bottom hole pressure (CBHP) [9].

An overview of the control process presented in this paper is shown in Fig. 2, where the three blocks at the top right hand side illustrate the physical part of the system and the three blocks at the top left hand side the implemented cascaded control structure. The bottom block demonstrate the hydraulic model that generates bit flow and BHP estimates. As Fig. 2 suggests, the MPD system actively controls the BHP, p_{dh}, and choke pressure, p_c, by manipulation of the choke opening z_c. The suggested control structure has three layers, an outer BHP controller, a choke pressure controller and an inner choke position controller. These controllers are implemented in different time scales; the inner loop is faster than the middle loop and the middle loop is faster than the outer loop.

A. System Overview

The system shown in Fig. 2 consist of three controlled variables, the choke opening, the choke pressure and the BHP, where the choke position and pressure are measured at high sampling rates. In contrast, the BHP measurement is obtained by a pressure-while-drilling (PWD) sensor and transferred with mud-pulse telemetry. New signals are obtained every 20-30 seconds, but their value is reduced by having a significant time delay and, at times, low accuracy and reliability [6]. Moreover, these measurements are not available at low mud pump rates, but static pressure during a connection can be received after the pumps have restarted.

When a single annular fluid and steady state is considered, the BHP is influenced by the choke pressure according to the formula [5]

$$p_{dh} = \rho g h + F(q) + p_c \tag{1}$$

where ρ is the mud density, g the acceleration of gravity, h the true vertical depth of the well, $F(q)$ is the frictional annular pressure due to the flow q and p_c is the choke pressure.

Due to the low resolution of the BHP measurement an estimate of the BHP is required to control the BHP. This was obtained based on a low order model with use of topside measurements of the choke pressure and standpipe pressure, p_p. For a detailed procedure of how this can be performed the reader is advised to review [3]. Higher order models also exists for estimation of the BHP, and can offer more detailed modeling of the well at the price of increased complexity [10].

B. Choke Position Control

The innermost of the three cascaded control loops, illustrated in Fig 2, is the choke position control. It is provided with the desired choke opening set-point, $z_{c,sp}$, from the choke pressure control, and outputs the desired motor rotation speed, ω_u. This control loop is designed to be fast, such that it does not need to be considered in the design of the outer control loops. From preliminary actuator analysis the choke position control is implemented with a model based approach that includes feedforward and feedback control. To obtain feedforward control in set-point changes a reference filter with a maximum ramp speed is implemented.

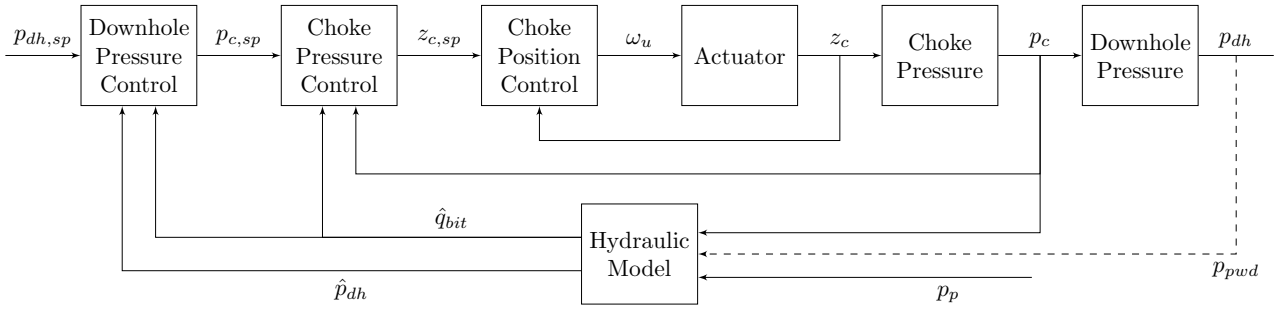

Fig. 2. Overview of control structure. The three blocks at the top left refer to the cascaded control structure and the three at the top right refer to the physical system. The hydraulic model estimates bit flow and bottom hole pressure from topside and PWD data.

C. Choke Pressure Control

The core control parameter in a MPD control system is the choke pressure, which is directly affected by the choke opening. By controlling the choke pressure the BHP can be modified as seen in (1). The choke pressure can be modelled as

$$\dot{p}_c = \frac{\beta}{V}(q_{bit} - q_c) \tag{2}$$

where β and V refer to the bulk modulus, representing compressibility, and annular volume respectively, while q_{bit} is the flow through the bit and q_c the flow through the choke given by the pressure difference over a flow restriction

$$q_c = K_c g(z_c)\sqrt{\frac{2}{\rho}(p_c - p_{co})}. \tag{3}$$

Here, K_c is the flow factor of a fully open choke, the choke characteristics, $g(z_c) \in [0, 1]$, translates the choke opening position, z_c, to an effective area opening and p_{co} is the pressure downstream the choke. The pressure control loop is developed based on (2) where the choke flow is designed to give the desired choke pressure, $p_{c,sp}$, by model based PI control design with feedforward control for tracking and disturbance rejection. The choke opening set-point, $z_{c,sp}$, is then obtained from feedback linearization of (3), similar to the procedure shown in [7]. The details of the implementation is out of the scope of this paper.

The rig sensors are exposed to disturbances and possible failures, which is especially critical for the choke pressure. For this reason, several sensors are used to add redundancy of each measurement. In addition, a choke pressure observer is designed based on choke opening and a measurement of the choke pressure. This observed choke pressure is then applied as the measured choke pressure in the implementation, and the control error is generated as the difference of the observed choke pressure and a filtered set-point value. The filter acts as a trajectory generator and ensures accurate tracking control in choke pressure set-point changes.

To effectively maintain the desired pressure during flow changes, for instance in connection scenarios, feedforward compensation is required. As the pump flow is frequently inaccurate and prone to errors it is not desired as a feedforward term. Instead, a bit flow estimate, $\hat{q}_{bit}$, based on choke and standpipe pressure measurements and tuned friction factors is generated by a hydraulic model[1]. The estimated bit flow acts as a filtered and delayed response of the pump flow and offers feedforward compensation in flow changes. With this flow estimate, the choke pressure controller automatically controls the desired choke position to minimize the effect of flow changes. In addition, the bit flow estimate is used to calculate the frictional contribution in the BHP estimator, which will be presented in the next section.

Due to continuous disturbances from, for instance, pumps and drill bit rotation, and to avoid unnecessary movements of the choke, the feedback error between the choke pressure and the desired pressure is restricted by a dead band close to zero to limit actuator overheating and wear and tear.

D. Bottom Hole Pressure Control

In MPD operations it is desired to maintain the BHP within the drilling window given by the rock formation. The desired BHP set-point, $p_{dh,sp}$, is given as a manual input and the choke pressure set-point, $p_{c,sp}$, is then controlled to obtain the correct BHP. The BHP is not available for continuous measurement, consequently it must be estimated based on topside measurements, such as the standpipe pressure and choke pressure, and updated with available BHP measurements, p_{pwd}, as illustrated in Fig. 2. Based on the BHP estimate a CBHP approach is performed by a cascaded control structure. This control structure necessitates slower control of the BHP than of the choke pressure to ensure time scale separation. This is performed by a slow PI control that modifies the choke pressure set-point such that the BHP converges to its desired value.

III. Results

The next sections demonstrate the performance of the cascaded control structure outlined in Section II. The data presented in this paper was obtained from two separate wells. The first was a 4000 m deep vertical well in the Umm al-Quwain region in Abu Dhabi. The second well was a 4000 m long well in the Archinskoye field in Siberia, Russia and

[1]Per definition the feedforward signal should be from a source in the external environment of the controller. This is not the case here, since $\hat{q}_{bit}$ is affected by the choke pressure. However, for simplicity this compensation will still be referred to as feedforward in this paper.

consisted of a 3000 m vertical section, drilled conventionally, followed by a 1000 m horizontal section, drilled with MPD, through several fractures in the rock formation. The first well was drilled with ordinary drilling mud. The vertical and first half of the horizontal sections in the second well was drilled with a mixture of water and nitrogen gas, while the second half of the horizontal section was drilled with crude oil produced while drilling. Note that in the Archinskoye well there was no measurement of the choke flow.

The sections in the result chapter are organized as follows. First, the performance of the inner choke position control is presented. Second, the performance of the choke pressure control is shown, together with necessary estimates of the bit flow and choke pressure. Third, the accuracy of the BHP estimator and control are demonstrated.

A. Choke Position Control

The performance of the inner choke position control loop is designed to be considerably faster than the choke pressure control loop. This difference in operating bandwidth ensures that the actuator dynamics do not need to be considered in the design of the choke pressure controller.

The performance of the actuator control is shown in Fig. 3 where the measured choke position, z_c, track the reference choke position, $z_{c,r}$ with negligible error. The reference choke position is generated by a second order reference filter. Fig. 3 also demonstrates the choke position control performance in choke pressure control mode. This illustrate the effect of the delay introduced by the choke position reference filter and its consequence on the pressure control performance. From the figure it is apparent that the choke position equals the choke position set-point satisfactorily. This result indicates that the choke pressure control is not affected by the inner choke position control loop. The spikes seen in Fig. 3 after 28 min and 34 min are caused by signal disturbances in the data logging.

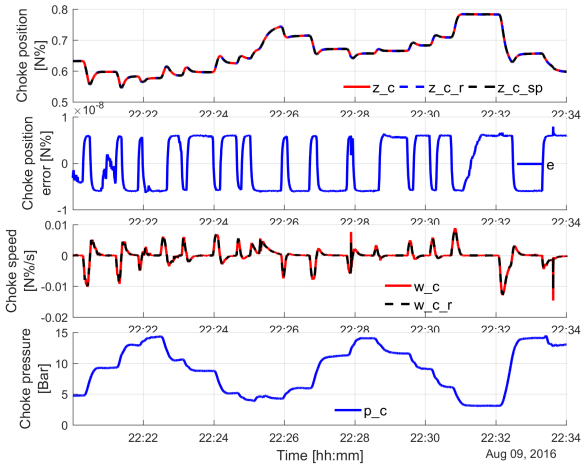

Fig. 3. Performance of choke position control in choke pressure control mode. The first subplot shows the choke opening measurement, reference and set-point. The second subplot shows the desired and measured actuator speed, the spikes seen in the measured speed at 28 and 34 min are caused by signal disturbances in the data logging. The third subplot presents the measured choke pressure.

B. Choke Pressure Control

1) Choke Pressure Observer: To ensure safe and robust feedback control of the choke pressure, as well as to reduce sensor noise, a pressure estimate is used to generate the choke pressure control error. A comparison of the choke pressure observer and a choke pressure measurement is illustrated in Fig. 4. Here, several set-point changes and two connections during a period of 25 min are performed while the estimated choke pressure equals the measured choke pressure.

2) Bit Flow Estimator: The bit flow estimator is used as a feedforward contribution to handle flow changes, e.g. during connections, and to calculate the frictional contribution in the BHP estimator. The bit flow is an unmeasured flow, therefore it is compared to the pump flow, q_p, and choke flow, q_c, in Fig. 5. The comparison in the first subplot shows the measured and estimated flow rates during four hours of drilling operation with three pump ramp-downs. The last two subplots show the standpipe pressure and choke pressure that affect the bit flow estimator. The bit flow estimate is demonstrated to track pump and choke flow, and will therefore provide an excellent feedforward contribution to the choke pressure control.

The bit flow estimator does not require a measurement of the pump flow, as demonstrated in Fig. 6. Here, the pump flow measurement freezes around time 10:40 due to a sensor error and stays frozen until this is detected almost two hours later. In this time period the bit flow continues to estimate the flow throughout a connection and the following flow ramp up. When the pump flow sensor is activated again it confirms the correctness of the estimated bit flow. This shows that the bit flow estimate can, in addition to its intended use, act as an indication of other sensor errors on the rig. Note that the choke flow, q_c, was routed through a different flow line in this operation and thus no choke flow or choke pressure measurements are presented in Fig. 6.

3) Choke Pressure Control Performance: The performance of the choke pressure controller is demonstrated in Fig. 7. Several set-point changes are performed followed by a connection where the pump flow is ramped down to zero while the choke pressure is kept constant. To reduce wear and tear in the actuator an error dead band of ± 1 bar was defined in the choke pressure controller, which is judged to be well within the required accuracy. When the pressure error is in this dead-band region, only feedforward control is active which explains the steady state errors seen in Fig. 7. In all set-point changes and in the connection the choke pressure is maintained within ± 2 bar, even through the abrupt pump changes during the connection.

The pressure control performance is further demonstrated in Fig. 8 where set-point changes in high pressure conditions are performed. When pressure alternates between high and low values, pressure control becomes more challenging due

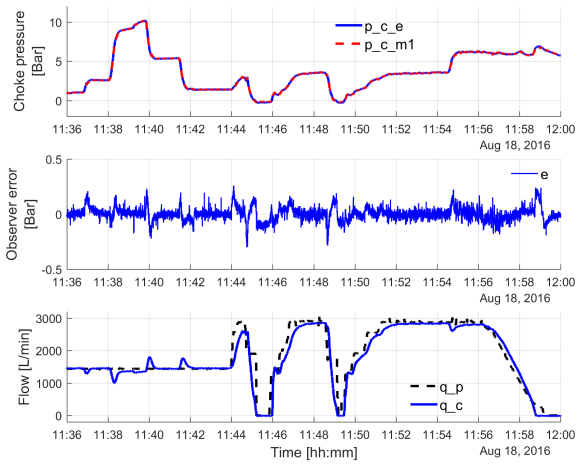

Fig. 4. Comparison of the choke pressure observer, $\hat{p}_c$, and the choke pressure measurement, p_c, through a period of several choke set-point changes and two connections. The first subplot shows the choke pressure, the second subplot presents the observer error between measured and estimated pressure and the third subplot shows the pump and choke flows. Data from the Umm al-Quwain well.

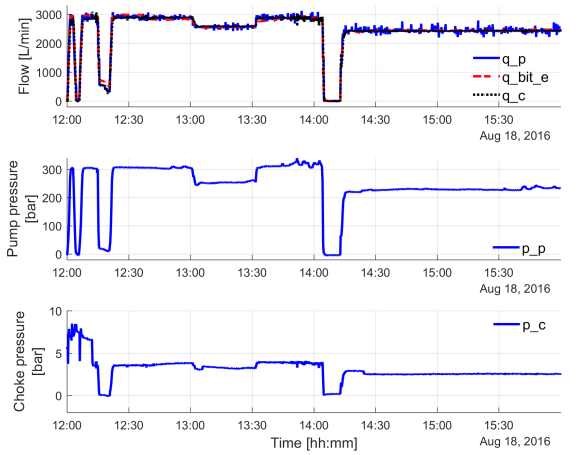

Fig. 5. Bit flow estimator compared to pump and choke flow for a period of 4 hours. The first subplot shows the estimated bit flow compared to pump and choke flow, the second subplot illustrates the standpipe pressure and the third subplot shows the choke pressure. Data from the Umm al-Quwain well.

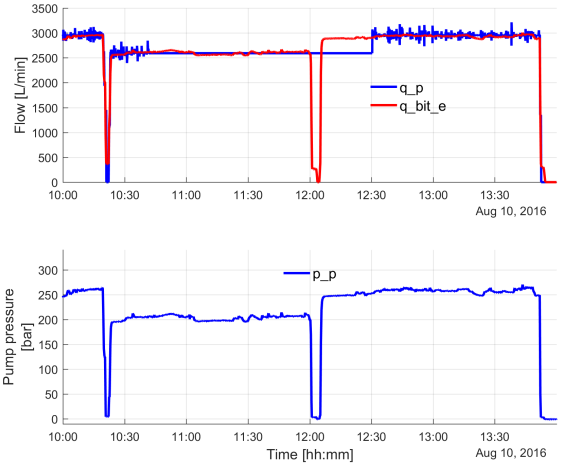

Fig. 6. Bit flow estimator compared to pump flow where the pump flow measurement froze between 10:40 and 12:30. The first subplot shows the estimated bit flow compared to pump flow, the second subplot illustrates the standpipe pressure and the third subplot presents the choke pressure. Data from the Umm al-Quwain well.

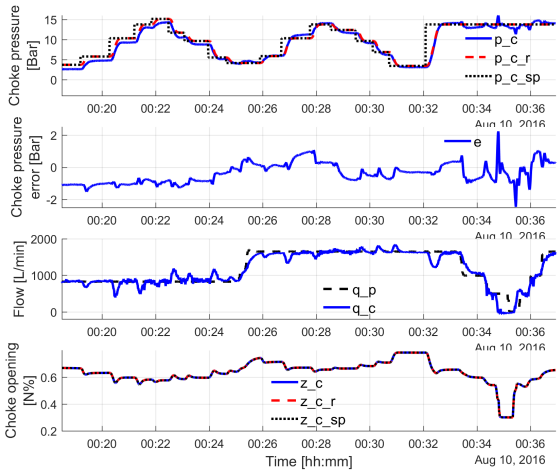

Fig. 7. Choke pressure control in set-point changes and connection. The first subplot illustrates the choke pressure control performance, the second subplot presents the control error, the third subplot shows the pump and choke flows and the fourth subplot illustrates the choke position movement. Data from the Umm al-Quwain well.

to variations of system gain. The feedback linearization procedure is designed to compensate for the varying system gain. The results from Fig 7 and Fig. 8 confirm that the feedback linearization achieves identical performance at high and low pressures.

A more challenging case for choke pressure control is shown in Fig. 9 where the set-point is increased from 40 bar to 80 bar in a well with multiple fractures. The well was drilled with a mixture of water and nitrogen gas, with a gas fraction that exceeded 50 % at the choke. In Fig. 9 the choke pressure is within ± 2 bar at all times, except for a short period around 14:13, which could be caused by pressure resonances or other disturbances in the well. When the choke pressure increased, the BHP exceeded the formation pressure a loss was observed. The loss can be identified from analysis of the estimated bit flow, which equals the pump flow at 40 bar choke pressure and shows zero flow for 80 bar choke pressure. The BHP goes from balancing the pore and formation pressure at 40 bar to exceed the formation pressure and take losses at 80 bar. The standpipe pressure does not increase as the choke pressure increases due to the heavy losses, and explains the drop in estimated bit flow.

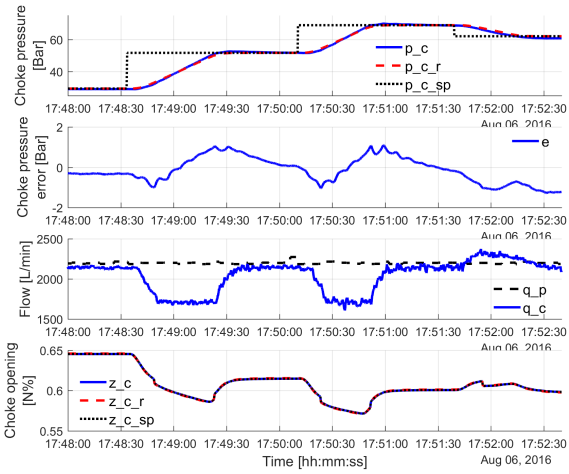

Fig. 8. Choke pressure control in set-point changes at high pressure. The first subplot illustrates the choke pressure control performance, the second subplot presents the control error, the third subplot shows the pump and choke flows and the fourth subplot illustrates the choke position movement. Data from the Umm al-Quwain well.

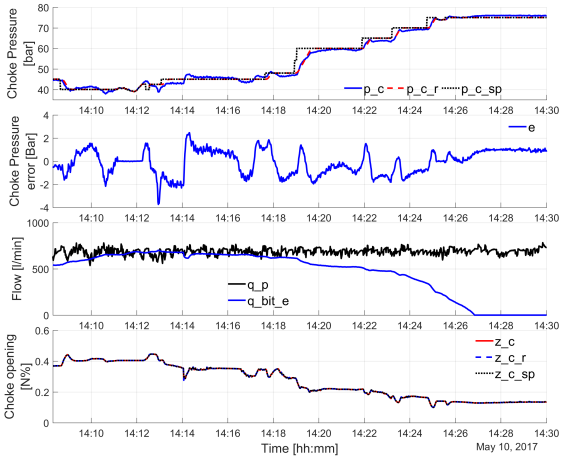

Fig. 9. Choke pressure control in set-point changes at high pressure with a significant amount of nitrogen gas mixed with water. The first subplot illustrates the choke pressure control performance, the second subplot presents the control error, the third subplot shows the pump and estimated bit flows and the forth subplot illustrates the choke position movement. Data from the Archinskoye well.

C. Bottom Hole Pressure Control

1) Bottom Hole Pressure Estimator: In Fig. 10 the estimated BHP is compared to the PWD measurements. In addition to the pressure comparison, the well depth and pump flow rate are shown in the figure. The PWD tool requires a certain flow rate to transfer BHP measurements, in this case more than 400 gal/min (approximately 1500 l/min). In the periods where the flow is less than 400 gal/min no pressure measurements are received topside, which is illustrated by the open periods of the PWD measurement in Fig. 10.

The red line in Fig. 10 shows the estimated BHP which

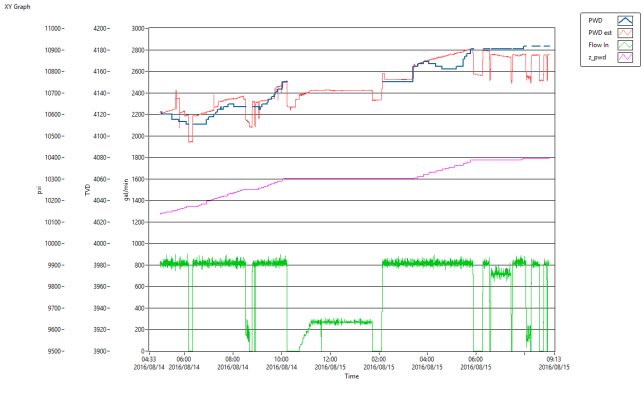

Fig. 10. Comparison of PWD data and BHP estimate. The blue line refers to PWD data, the red is the pressure estimate obtained from the BHP estimator, the purple is the measured depth and the green shows the pump flow. Data from the Umm al-Quwain well.

ideally should track the blue line of the PWD measurement. When the entire time range is analyzed there are two periods where the BHP estimate trend differently compared to the PWD measurements. The first error, at 06:00 pm, is seen as a sudden increase in BHP estimate while the measurement trends downwards. This is caused by an erroneous manual tuning of the density in the BHP estimator. However, this was quickly corrected, illustrated by the sudden decrease in pressure estimate. The second error, between 04:00 am and 06:00 am, is longer. Here, the trend of the PWD measurements and BHP estimator are opposite. This occurs when drilling, demonstrated by the increasing depth of the well, and intuitively the BHP should increase due to increased hydrostatic pressure. However, a lower density mud was pumped during a short time period due to human error. After this was detected, the mud weight was increased to the correct value and, as the lighter mud was circulated out of the annulus, the PWD measurement increased to the same pressure as the BHP estimator.

The data presented in Fig. 10 shows that, except during human errors, the BHP estimate is within a bound of 2-3 bar (30-45 psi) at all times. An alternative to the simple downhole estimator presented here would be a high fidelity simulator that runs in parallel with the control system. Such a solution would, if tuned properly, give more accurate results at the price of increased complexity. The achieved accuracy shown here was judged more than sufficient to control the BHP in the relevant well.

2) Bottom Hole Pressure Control Performance: The objective of most drilling operations is to maintain CBHP. A critical challenge in normal operation for the CBHP technique is to maintain pressure throughout a connection; a challenge that becomes more difficult when no back-pressure pump is available. In a connection, frictional pressure decreases as the pump flow is ramped down, consequently the controller must close the choke to increase choke pressure and maintain CBHP. In Fig. 11 the BHP control performance is presented in a set-point change followed by a connection. The choke pressure, shown in the third subplot, increases

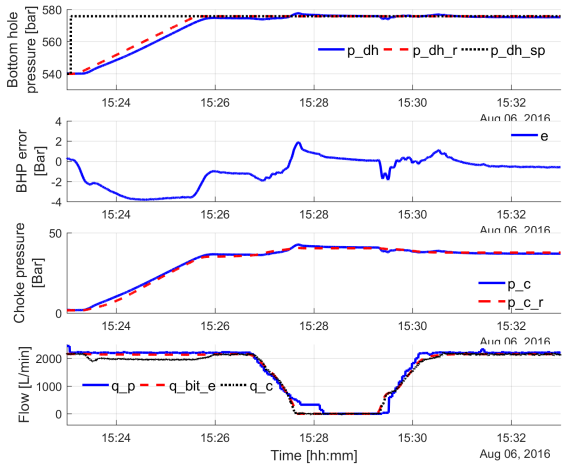

Fig. 11. BHP control in a set-point change and a connection. The first subplot demonstrates the BHP performance, the second subplot presents the BHP control error, the third subplot illustrates the choke pressure response and the fourth subplot shows the pump, choke and estimated bit flows. Data from the Umm al-Quwain well.

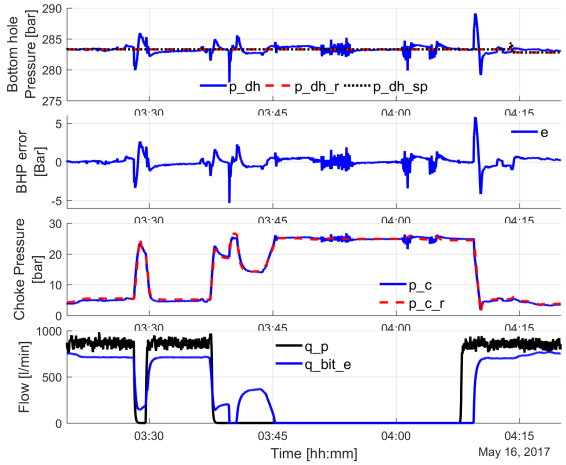

Fig. 12. BHP control in two flow ramp downs at high annular friction. The first subplot demonstrates the BHP performance, the second subplot presents the BHP control error, the third subplot illustrates the choke pressure response and the fourth subplot shows the pump, and estimated bit flows. Data from the Archinskoye well.

when the pump flow is ramped down and the BHP is maintained constant. The error observed through the set-point transient in Fig 11 is larger than in choke pressure control mode, as shown Fig. 7 and Fig. 8. This is caused by the slow PI control in the BHP control loop and would be reduced if tuned more aggressively, however this might cause challenges with regards to time scale separation. This is a limitation of the cascaded control design.

The Umm al-Quwain well had low annulus friction and thus required a limited increase in choke pressure to maintain CBHP in connections. Fig. 12 show flow ramp-down data from a well with significantly higher annulus friction. Here, the choke pressure increased from 5 bar to 25 bar to compensate for the lost annular friction. The main events in Fig. 12 are as follows; the first ramp-down in pump flow is to receive a data package from the PWD tool. The second ramp-down is the beginning of the connection. The increase in bit flow estimate between 03:40 and 03:45 was caused by nitrogen being pumped to displace the mud in the top drive. The oscillations at 03:52 and 04:03 are caused by disconnection and connection of the top drive to the drill string. The connection procedure was finished at about 04:10. The results show that the pressure is within a margin of ± 2.5 bar in the majority of the operation. In fast flow variations larger errors are observed, however the periods are short and the controller quickly compensates. Overall, these results show that the cascaded control structure can handle fast flow changes and still maintain the BHP within the drilling window.

IV. CONCLUSION

In this paper, field results from a cascaded control structure for MPD was presented focusing on the performance in set-point changes and connections. It was demonstrated that the fast inner position control does not affect the performance of the choke pressure control. Results of the choke pressure-, bit flow- and BHP estimators illustrate their validity for control applications. The choke pressure and BHP were shown to maintain pressure in set-point and connection operations, which includes an increase of choke pressure to maintain CBHP at zero flow conditions and fast flow variations in connections.

REFERENCES

[1] B. Dow, "Schlumberger's At Balance brand aims to make MPD more accessible," Apr. 2015.

[2] Weatherford, "MICROFLUX CONTROL SYSTEM," http://www.weatherford.com/en/products-services/drilling-formation-evaluation/secure-drilling-services/managed-pressure-drilling/microflux-control-system#, Nov. 2016.

[3] Ø. N. Stamnes, J. Zhou, G.-O. Kaasa, and O. M. Aamo, "Adaptive observer design for the bottomhole pressure of a managed pressure drilling system." IEEE, 2008, pp. 2961–2966.

[4] Ø. N. Stamnes, O. M. Aamo, and G.-O. Kaasa, "Redesign of adaptive observers for improved parameter identification in nonlinear systems," *Automatica*, vol. 47, no. 2, pp. 403–410, 2011.

[5] G.-O. Kaasa, Ø. N. Stamnes, O. M. Aamo, and L. S. Imsland, "Simplified hydraulics model used for intelligent estimation of downhole pressure for a managed-pressure-drilling control system," *SPE Drilling & Completion*, vol. 27, no. 01, pp. 127–138, 2012.

[6] J.-M. Godhavn, "Control Requirements for Automatic Managed Pressure Drilling System," *SPE-119442-PA*, Sep. 2010.

[7] J.-M. Godhavn, A. Pavlov, and G.-O. Kaasa, "New automatic control solutions for the drilling industry," *Transaction on Control and Dynamical Systems*, vol. 2, no. 2, pp. 61–69, 2013.

[8] D. G. Reitsma and Y. Couturier, "New Choke Controller for Managed Pressure Drilling," *IFAC Proceedings Volumes*, vol. 45, no. 8, pp. 223–230, 2012.

[9] B. Rehm, J. Schubert, A. Haghshenas, A. S. Paknejad, and J. Hughes, *Managed Pressure Drilling*. Elsevier, 2013.

[10] K. S. Bjorkevoll, A. E. Vollen, I. Barr Aas, and S. Hovland, "Successful use of real time dynamic flow modelling to control a very challenging managed pressure drilling operation in the North Sea." Bjorkevoll2010: Society of Petroleum Engineers, 2010.

Paper G

Automated Pressure Control for UBD Operations; Case study and Field Validation

Berg, Christian, Jon Åge Stakvik, Stanislav Kulikov, Glenn-Ole Kaasa, Aleksandr Dubovtsev, Sergey Korolev, and Veliyev Gurban. "Automated Pressure Control for UBD Operations; Case Study and Field Validation." SPE Drilling & Completion, Society of Petroleum Engineers, 2019. https://doi.org/10.2118/194555-MS.

Authors' role in the article: Ideas, implementation, system set up and operation in the field and writing.

Doctoral dissertation no. 61
2020

—

Modeling for Automatic Control and Estimation of Influx and Loss During Drilling Operations

Dissertation for the degree of Ph.D

—

Christian Berg

—

ISBN: 978-82-7206-544-6 (print)
ISBN: 978-82-7206-545-3 (online)

usn.no